BSc Thesis Physics

Kapteyn Astronomical Institute

RIJKSUNIVERSITEIT GRONINGEN

The Cosmic Shoreline: Modelling Bare-rock Surfaces and Atmospheres on Rocky M-dwarf Exoplanets

Author:
Karen Stuitje
s4339150

Supervisor:
Dr. Tim Lichtenberg
Co-supervisor:
Dr. Mark Hammond
Second examiner:
Dr. Kristof de Bruyn

Groningen July 7, 2025

Abstract

Context. Rocky exoplanets around M-stars are promising targets for finding extraterrestrial life, but may not retain atmospheres. Degeneracies between bare surface and atmosphere observations complicate mapping the cosmic shoreline: the boundary between planets with and without atmospheres.

Aims. This thesis characterises four M-star exoplanets (GJ 486b, GJ 367b, TRAPPIST-1b, TRAPPIST-1c) using JWST mid-infrared observations to distinguish bare-rock surfaces from atmosphere scenarios.

Methods. I modelled compositions using the 1D radiative-convective model AGNI, incorporating heat transport. I applied a Bayesian model selection framework and simulated future JWST/MIRI broadband observations.

Results. For GJ 486b, water atmospheres (0.01 – 100 bar) outperform surface models, although heat transport weakens the evidence. GJ 367b is most likely bare, but characterising its surface remains challenging. TRAPPIST-1b and 1c may lack thick atmospheres, although nitrogen-methane atmospheres ($\leq$ 10 bar) with substantial heat transport remain viable.

Conclusions. Heat transport significantly affects atmosphere characterisation. Observational degeneracies between atmospheric and surface emissions limit definitive atmosphere detection. Mapping the cosmic shoreline requires combining multiple JWST techniques.

Contents

1 Introduction

Since the first detection of an exoplanet in 1995 [Mayor and Queloz, 1995], nearly 6,000 planets beyond our solar system have been discovered. This number has grown exponentially in the last 15 years, driven by the success of the transit method: observing small dips in the light of stars as planets pass in front of them. The planets discovered in the last two decades are remarkably diverse, ranging from gas giants larger than Jupiter to small, rocky planets similar to Earth. It is these rocky worlds that most capture our imagination: they could be the hosts of extraterrestrial life.

An atmosphere is essential for sustaining life, but retaining one can be challenging. In the past decade, detecting atmospheres on rocky exoplanets has become a central focus in exoplanet science. The recently-launched James Webb Space Telescope (JWST), a space-based telescope observing in the infrared, now provides the best resolution yet for characterizing atmospheres on Earth-like planets. Rocky planets orbiting M-stars are the most promising targets. These small, cool stars make up most of the Milky Way's stellar population, and about 75% of their planets is expected to be rocky [Pan et al., 2021]. Figure 1 shows a selection of M-star systems, with their planets and habitable zones. The low luminosity and size of M-dwarfs make it easier to detect small planets passing in front of them; they are however, also known for their frequent flares and high levels of extreme-ultraviolet (XUV) radiation, which might easily strip their planets bare. This leads to the question: do rocky M-dwarf exoplanets have atmospheres – and can we detect them?

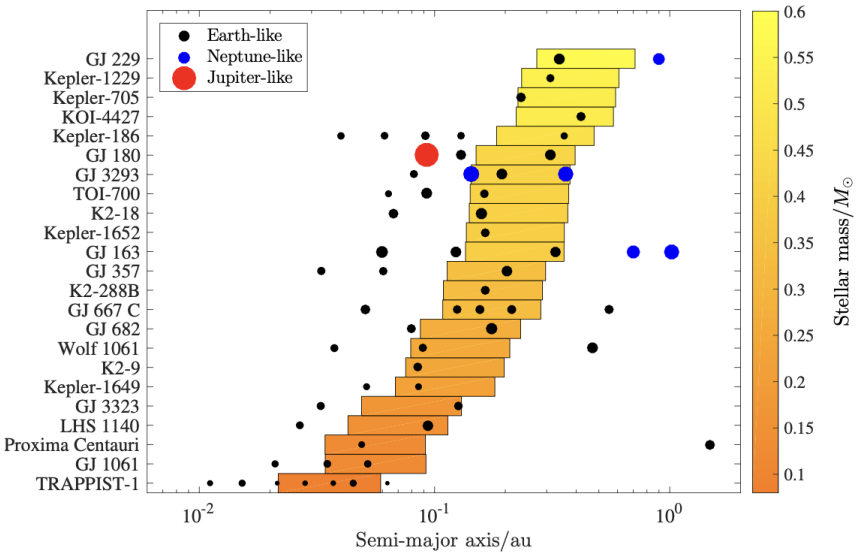

Figure 1: Planetary systems with M-star hosts: stars of masses up to 0.6 solar masses. A significant portion of their planets are Earth-like, shown here in black. Habitable zones – the range of distances from the star that could allow for liquid water – have been shown as coloured regions of the semimajor axis (in AU: Earth-Sun distances). Planets with the highest observational resolution are often too close to their star to be habitable; detecting atmospheres on these planets, however, would be promising for all rocky planets around M-dwarfs. Image by Pan et al. [2021].

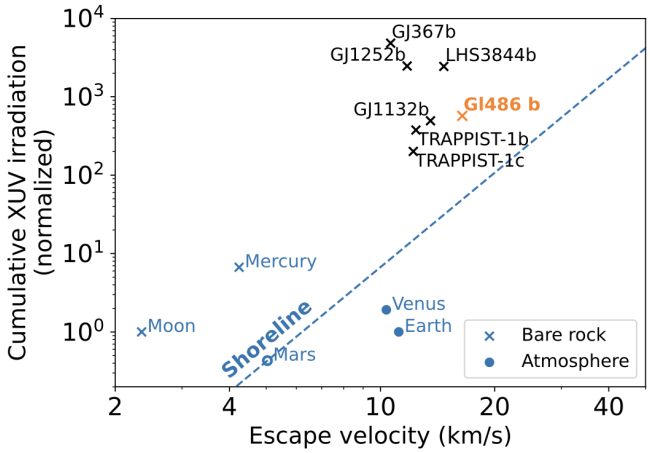

Figure 2: The estimated cosmic shoreline, where crosses indicate planets consistent with no atmosphere [Mansfield et al., 2024]. Solar system bodies have been shown, as well as a number of M-dwarf exoplanets, of which the current atmosphere status is still unknown.

A common framework for understanding atmospheric retention is the 'cosmic shoreline': a proposed boundary that separates planets with atmospheres from those without [Zahnle and Catling, 2017]. This boundary depends on a planet's surface gravity and how much extreme-ultraviolet (XUV) radiation it receives from its star, as shown in Figure 2. Constraining the location of this shoreline, by determining the presence or absence of atmospheres on rocky exoplanets, has become a central goal of JWST observations [Redfield et al., 2024].

Despite JWST's sensitivity, no unambiguous atmospheric detections have yet been made for rocky exoplanets [Hammond et al., 2025]. Transit spectroscopy, the most widely used method for atmospheric characterization, works by studying light that passes through a planet's atmosphere as it crosses in front of its star. This method requires very specific conditions: the host stars must be ultra-cool (below 3000 K) and the planets must be temperate, receiving between 0.25 and 4 times Earth's sunlight [TRAPPIST-1 JWST Community Initiative, 2024]. This greatly limits the number of suitable target systems. An alternative approach is secondary eclipse spectroscopy, which observes a planet passing behind its star. By comparing the star's emission alone with the combined emission of star and planet, we can study the planet's thermal emission. Differences between the observed emission and the expected blackbody emission could indicate the presence of an atmosphere: caused by, for example, atmosphere absorption, high reflection from clouds, or the redistribution of heat to a planet's nightside [Hammond et al., 2025]. An illustration of a planet's transit and secondary eclipse has been shown in Figure 3.

A major challenge, however, lies in separating atmospheric signals from surface effects. A bare rocky surface can produce spectral features similar to those from an atmosphere, due to the way that it reflects and emits light. For example, a high-albedo surface – a surface which reflects a large amount of the light it receives – heats up the planet less, mimicking the effect of an atmosphere that absorbs a large part of a planet's outgoing radiation. As the resolution of data of small, Earth-like planets is limited, their surface and atmospheric signatures might be nearly indistinguishable [Hammond et al., 2025].

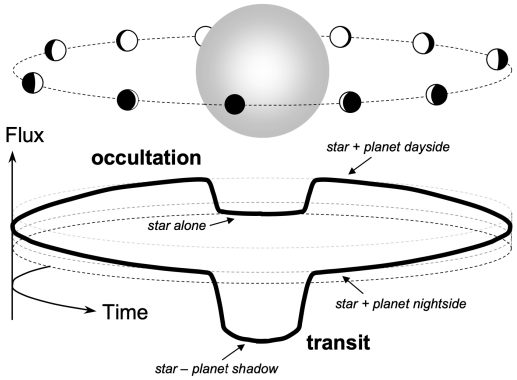

Figure 3: Illustration of a planet's transit and its secondary eclipse, also called 'occultation'. Just before a planet passes behind its star, we observe its dayside; when its passes, we see the star's emission alone. The difference between these two phases allows us to study a planet's own thermal emission. Image by Winn [2010].

Modelling rocky exoplanets both with and without atmospheres helps us understand the difference between spectral features of bare-rock planets, and of those with atmospheres. Models take into account a planet's incoming radiation, reflection properties of its surface, and absorption and re-radiation by atmospheric elements. Combined with JWST's mid-infrared secondary-eclipse measurements, they might constrain the types of surfaces and atmospheres on the rocky exoplanets we observe. Furthermore, comparing models to measurements helps us understand the limitations of JWST in atmosphere detection.

Recently, mid-infrared (5 – 12 μm) observations of the secondary eclipses of several rocky planets orbiting M-dwarf stars have been published. These planets are tidally locked; they always face their host star with the same side. They include GJ 486b [Mansfield et al., 2024] and GJ 367b [Zhang et al., 2024]. GJ 486b is a warm super-Earth, that might have retained its atmosphere; GJ367b, on the other hand, is small and hot, and most likely a bare rock. Additionally, thermal emission has been observed of the two most close-in TRAPPIST-1 planets at 15 μm and 12.8 μm [Zieba et al., 2023, Ducrot et al., 2025].

This thesis aims to simulate a range of surface and atmospheric scenarios for these four exoplanets, applying the 1D radiative-convective model AGNI [Nicholls et al., 2025a] to generate emission spectra of the planets' daysides. These modelled spectra are compared to existing secondary-eclipse observations by the James Webb Space Telescope (JWST) using a Bayesian model selection framework. Additionally, the spectra are used to simulate future photometric observations with JWST, to assess the telescope's ability to differentiate between planets with, and without an atmosphere.

The thesis is structured as follows: Chapter 2 introduces the theoretical background on atmosphere evolution, surface compositions, and observational techniques relevant to rocky M-dwarf exoplanets. Chapter 3 describes the modelling and analysis applied. Chapter 4 presents the results of the simulations for each target planet. Chapter 5 discusses these findings in the broader context of atmospheric retention and exoplanet characterisation. Finally, Chapter 6 summarises the main conclusions and outlines directions for future research.

2 Theoretical context

Essential for habitability on a planet like Earth is the presence of an atmosphere. An atmosphere stabilises surface temperature, provides pressure to sustain liquid water, and contains the elements necessary for life to develop. For a planet to be habitable, however, it must transition from its primary, hydrogen-rich atmosphere it accreted during formation, to a secondary atmosphere composed of heavier elements such as water vapour, carbon dioxide, and nitrogen. Despite the recent launch of the James Webb Space Telescope (JWST), no secondary atmosphere has so far been found on an Earth-sized planet [Van Looveren et al., 2025].

This chapter provides an overview of current theories on atmospheric evolution and retention. Additionally, I will briefly go over the observational methods used to detect atmospheres on rocky exoplanets, and discuss the challenges involved. Finally, I will discuss the current status of the cosmic shoreline; which rocky planets are, and are not likely to have retained their atmosphere.

2.1 Atmosphere evolution and retention

An exoplanet atmosphere's evolution is affected by a combination of internal and external processes, including the accretion and loss of a primary atmosphere, the formation of a secondary atmosphere through outgassing, and its evolution or erosion. This section reviews current theories on how planetary atmospheres form, evolve, and are retained.

2.1.1 Primary and secondary atmospheres

A rocky planet is thought to develop in the protoplanetary disk with a primary atmosphere accreted from the nebula, composed of mostly hydrogen and a small amount of helium. These light gases are often short-lived on terrestrial planets, especially those with relatively low mass and exposed to intense stellar radiation, such as M-dwarf exoplanets. The primary atmosphere is lost likely due to UV and X-ray irradiation, and internal heating [Wordsworth and Kreidberg, 2022]. Nevertheless, recent studies suggest that many terrestrial exoplanets began with substantial, long-lived H_2-rich atmospheres, which might later be replaced by considerable secondary atmospheres [Krissansen-Totton et al., 2024].

For a planet to gain a primary atmosphere, it needs to form before the stellar system's disk is dispersed. This atmosphere will be retained if the planet has a low enough temperature, for the accreted molecules to, on average, stay below the planet's escape velocity. This is often quantified with the gravitational escape parameter λ [Wordsworth and Kreidberg, 2022]:

$$\lambda \equiv \frac{E_P}{E_K} = \frac{GMm}{kTR}, \tag{1}$$

where E_P is the gravitational potential energy, E_K the kinetic potential energy, G is the gravitational constant, M the planet mass, m the molecular mass, k the Boltzmann constant, T the local temperature of the gas and R is the radius of the base of the escaping region. Starting from about an Earth's mass, planets can accrete an atmosphere of 1% of their mass, allowing them to increase in radius and become a sub-Neptune [Wordsworth and Kreidberg, 2022].

Sub-Neptunes are one of the two most common types of exoplanets: planets smaller than Neptune, but with a substantial gaseous envelope. The other main category is the super-Earth – planets larger than Earth that are rocky, although their atmospheres can still be significant. Between these two types lies a gap in planet radii, known as the radius valley [Burn et al., 2024]. This valley refers to the relative lack of exoplanets with sizes between super-Earths and sub-Neptunes, and is thought to result from atmospheric loss. Studies suggest that both types of planets form with similar sizes and accrete thick (over 10,000 bar) primary atmospheres, but a large fraction lose this envelope over time, shrink, and become rocky super-Earths [Kite and Barnett, 2020].

The mechanism driving this atmospheric loss is believed to be XUV-driven hydrodynamic escape, a process mostly relevant in the planet's first 100 to 1000 million years. In this early phase, intense X-ray and ultraviolet (XUV) flux from the young host star heats the upper atmosphere, creating outflows of hydrogen that can strip away a planet's primary atmosphere [Wordsworth and Kreidberg, 2022]. M-stars, cool, dim stars of masses up to 0.6 solar masses, spend an extended period in a pre-main sequence phase, during which their luminosity and XUV output is elevated. Furthermore, planets around M-stars are generally closer to their stars, further increasing the amount of high-energy radiation they receive [Gialluca et al., 2024]. Planets orbiting M-dwarfs in M-dwarf systems are therefore considered particularly prone to losing their (primary) atmospheres [Wordsworth and Kreidberg, 2022].

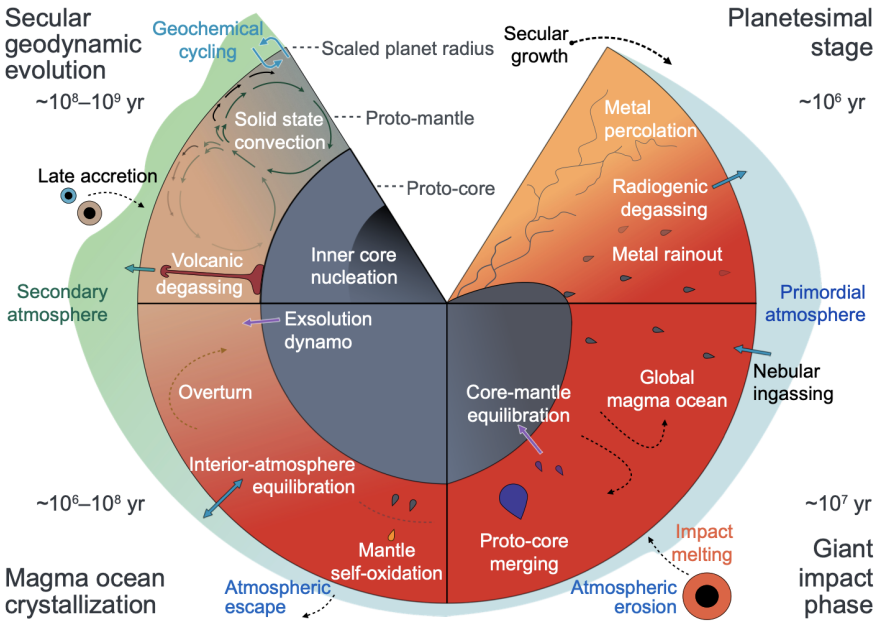

Figure 4: The transition from a primary to a secondary atmosphere on a rocky planet, along with key interior processes, by Lichtenberg et al. [2022]. A primordial H_2-rich atmosphere initially forms through nebular ingassing. This atmosphere is gradually lost due to XUV-driven atmospheric escape and giant impacts; simultaneously, heavy volatiles are outgassed from the mantle during magma ocean crystallization. Volcanic degassing is considered the primary driver for the formation of the secondary atmosphere.

Fortunately for the search for life, a secondary atmosphere with heavier, less easy-to-lose elements can form on a planet after the loss of its primordial envelope. This atmospheric rebuilding happens mainly through volcanic degassing and magma ocean crystallization, releasing heavier elements, often called volatiles, like carbon dioxide and water vapour from the planet's interior [Lichtenberg et al., 2022]. The transition from a primary to a secondary atmosphere has been illustrated in Figure 4. Additional volatiles may be delivered by impacts from icy asteroids [Kral et al., 2024]. Furthermore, Kral et al. [2020] propose that high-metallicity secondary atmospheres could form through late disk accretion: observations suggest that some stellar systems retain significant amounts of gas even in later stages of evolution. Planets in these systems may continue to accrete material, transforming their early atmospheres into dense secondary atmospheres.

It must be noted that Kite and Barnett [2020] find that an initially thick primary atmosphere can hinder the development of a dense, secondary atmosphere, as volatiles are lost in the hydrogen wind. They suggest that substantial secondary atmospheres are more likely on planets that formed hydrogen-poor, and that already started out with a large amount of volatiles. On the other hand, the models of Krissansen-Totton et al. [2024] show that thick primary atmospheres might not preclude the formation of a secondary atmosphere, and could even result in large amounts of surface water.

2.1.2 Erosion of the secondary atmosphere

Even after the formation of a secondary, high–molecular-weight atmosphere, long-term retention is not guaranteed. These atmospheres remain vulnerable to atmospheric escape, such as thermal escape – when high-energy radiation heats the atmosphere so that lighter particles reach escape velocity – along with losses due to the stellar wind, impacts, and collisions. For small exoplanets orbiting M-dwarfs, these processes can be especially influential. M-dwarfs show enhanced starspot activity, might have greater coronal mass ejections, and, as mentioned before, spend a large amount of time as pre-main sequence stars with increased luminosities [Wordsworth and Kreidberg, 2022].

An escape process that is especially dangerous to M-dwarf exoplanet atmospheres is the photolysis of H_2O. A large amount of H_2O in a planet's atmosphere can realise a runaway greenhouse effect, influenced by the star's increased, pre-main sequence luminosity. This H_2O is broken apart by the star's XUV flux, and escapes, drying up the planet completely [Wordsworth and Kreidberg, 2022]. M-star flaring could worsen this effect, increasing the XUV flux with 10%, and removing up to two Earth oceans of water more [do Amaral et al., 2022]. Even after the star's early, violent phase, flares could be a dominant cause of atmospheric removal [France et al., 2020].

On the other hand, once the planet is mostly stripped of hydrogen, its atmosphere is significantly more resistant to hydrodynamic escape; the process where lighter atoms – mostly hydrogen – escape, and drag along heavier atoms. When no heavier molecules escape via drag, much higher temperatures are required for heavy volatiles to escape the planet [Wordsworth and Kreidberg, 2022].

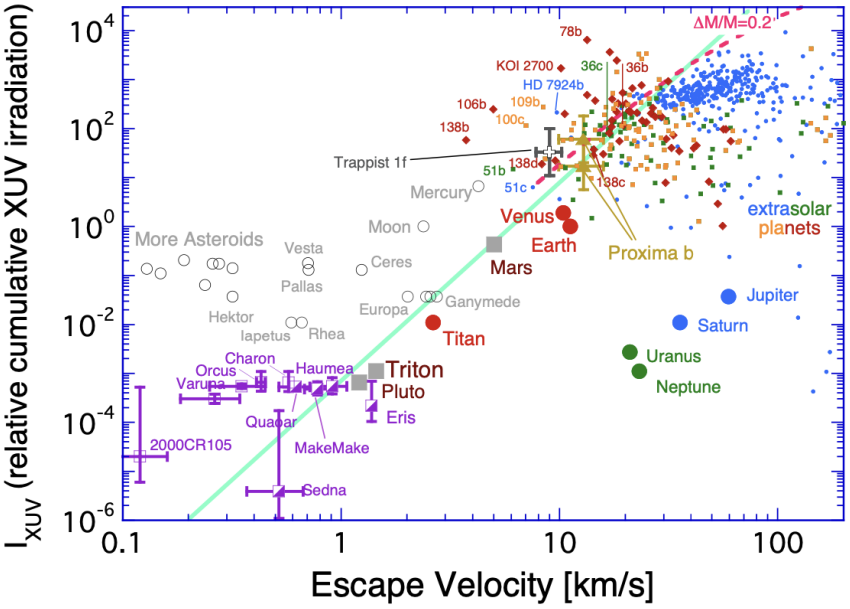

Figure 5: The original, semi-empirical cosmic shoreline, as proposed by Zahnle and Catling [2017], here shown as the incoming XUV flux versus escape velocity. The cosmic shoreline has been shown in green. Solar bodies with atmospheres are shown as filled symbols, where airless bodies are open. Several exoplanets have been shown as well, with planets with radii below 1.6 Earth-radii as red diamonds. Abbreviations like "138b" refer to "Kepler 138b."

2.1.3 The cosmic shoreline

The degree to which M-dwarf exoplanets can retain their atmospheres remains highly uncertain. Both the escape processes discussed above, and additional mechanisms – such as atmospheric loss due to impacts – are still poorly understood. To address these uncertainties, researchers have proposed semi-empirical approaches, one of which is the *cosmic shoreline*, introduced by Zahnle and Catling [2017]. Based on solar system observations, they found that planetary bodies tend to fall into two categories – those with atmospheres and those without – when plotted in terms of insolation (I), or incoming stellar flux, versus escape velocity (v_{esc}). The line that divides them has the proportionality:

$$I \propto v_{\text{esc}}^4. \tag{2}$$

In XUV, the same proportionality holds. The original proposed cosmic shoreline has been shown in Figure 5. This semi-empirical relation is currently being tested in large-scale JWST surveys, with the goal of detecting rocky exoplanet atmospheres [Redfield et al., 2024].

2.1.4 Atmosphere chemistry and composition

This thesis aims to model the atmospheres of rocky exoplanets orbiting M-dwarfs. From theoretical models, we know that the chemical composition of such atmospheres can vary, depending on atmospheric escape, incoming radiation, volatile delivery, greenhouse effects, equilibrium processes, and exchange with the mantle [Herbort et al., 2020, Wordsworth and

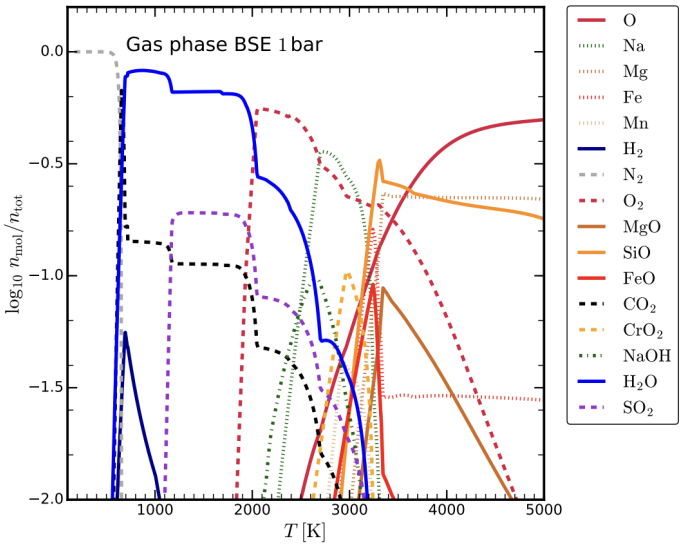

Figure 6: Atmosphere abundances for various atmospheric temperatures, assuming bulk silicate Earth (BSE) element abundances. By Herbort et al. [2020].

Kreidberg, 2022]. An important underlying framework is redox chemistry; that is, the balance between reducing elements, that easily donate electrons, and oxidising species, which are more likely to accept electrons. Common reducing species are hydrogen and iron; and, as the name, oxygen is an example of an oxidising element. The redox chemistry of an atmosphere affects climate stability and planet habitability [Wordsworth and Kreidberg, 2022].

Generally, a reducing atmosphere will be rich in H_2 or CH_4, whereas oxidized atmospheres, like the Earth's, contain large fractions of O_2 or CO_2. As discussed before, M-dwarf exoplanets are likely to lose their hydrogen fast; this leads to net oxidation of the atmosphere, making the redox state a dynamic characteristic of the planet. Without considering interior exchange, rocky exoplanets will become more oxidised over time, and combined with high XUV radiation this could even result in abiotic O_2 from the photolysis of water [Wordsworth and Kreidberg, 2022, Lingam, 2020].

When approximate elemental abundances, temperature, and pressure are known, equilibrium chemistry will predict atmospheric composition, based on the minimisation of the Gibbs free energy [Wordsworth and Kreidberg, 2022]. Herbort et al. [2020] find that atmospheres below 600 K are dominated by N_2 or CH_4, whereas above 600 K H_2O, CO_2, SO_2 are most abundant. Furthermore, modelled atmospheres above magma oceans, relevant for temperatures above $\sim$ 1700 K, are found to contain H_2O, O_2, CO_2, SO_2, and potentially CO and H_2 depending on the composition of the magma. Highly irradiated rocky exoplanets with atmospheric temperatures above 2000 K are expected to mostly contain species such as O_2, O, Mg, SiO, and Fe, depending on the oxidisation state [Seidler et al., 2024]. One set of modelled atmosphere abundances by Herbort et al. [2020], under the assumption of Earth-like element abundances, is shown in Figure 6.

For hot planets, any atmosphere they have can be considered to be, to a reasonable extent, in equilibrium. For cooler planets, however, disequilibrium processes become more relevant. These processes can be the presence of life, which led to the large amount of oxygen in the atmosphere of modern Earth, but also volcanism and impacts, and photochemistry

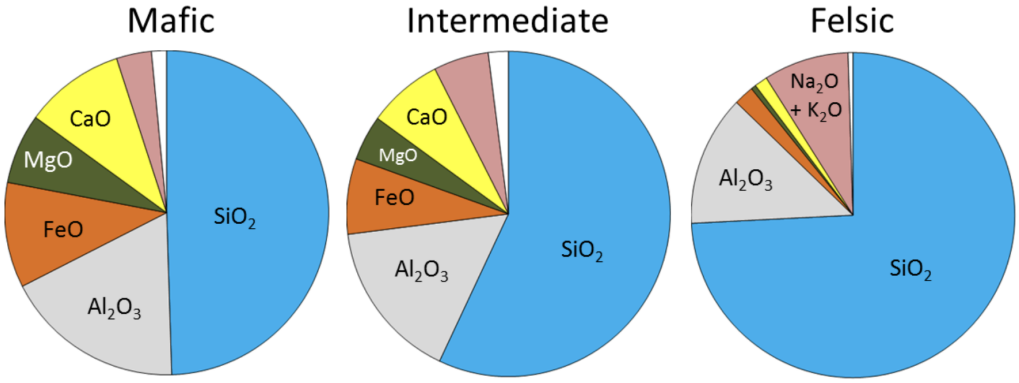

Figure 7: Chemical compositions of mafic, intermediate and felsic rock types. Mafic rocks contain less silicates (SiO_2) and more iron, calcium, aluminium and magnesium. Felsic rocks contain more silicates and alkalis (Na_2O, K_2O). Image from Earle [2015].

driven by UV radiation [Wordsworth and Kreidberg, 2022]. Photochemical effects in the upper atmosphere is largely dependent on the type of host star, because of differences in stellar spectra and stellar activity [Jordan et al., 2021]. Additionally, which exact reactions dominate under the influence of stellar UV radiation is not well-constrained [Wordsworth and Kreidberg, 2022].

2.2 Bare rocks: exoplanet surfaces

As seen earlier in this chapter, it is not unlikely that a significant portion of M-star exoplanets, if not all of them, will have been stripped of an atmosphere. In this case, spectral features in a planet's thermal emission will arise from surface characteristics. Being able to characterise a planet's surface will become more and more relevant in the future, as surface reflection plays a crucial role in a planet's climate [Madden and Kaltenegger, 2020].

The surface of a rocky planet is determined by partial melt eruptions from the mantle. When the planet's mantle undergoes partial melting, the resulting magma is transported to the surface, where it cools and solidifies to form the surface rocks we observe. The mineralogy of these surface rocks depends on the planet's bulk composition, the pressure and temperature at the melting depth in the mantle, and the amount of magmatic differentiation – processes, such as crystallisation, that change the chemical composition of the magma over time [Brugman et al., 2021]. For planets with Earth-like compositions – rich in iron and magnesium – this typically results in a mafic crust. These crusts are generally made of dark, dense rocks with low amounts of silica (SiO_2). Examples are the volcanic rocks gabbro, or basalt. On Earth, basaltic rocks cover around two-thirds of the surface and form the oceanic crust. Similarly, basalts make up most of the surfaces of Mars, the Moon, Mercury, and likely Venus [Putirka, 2024].

Planetary interiors may also undergo extended hydrous melting: partial melting that occurs in the presence of water. This lowers the melting temperature of rocks and can lead to the formation of felsic crusts [Foley, 2024]. These crusts are richer in silica and lighter elements such as aluminium and potassium. On Earth, this type of crust forms the continents, mostly in

the form of granite. Felsic rocks may develop on exoplanets that host abundant liquid water and experience plate tectonics, although the exact processes behind felsic crust formation remain under debate [Bernadet et al., 2025, Aranovich et al., 2025]. The compositional differences between mafic, felsic and intermediate rocks have been shown in Figure 7.

Finally, some planets may develop ultramafic crusts, composed of magnesium-rich minerals like olivine and pyroxene, and very low in silica content [Hu et al., 2012]. Ultramafic rocks make up most of Earth's upper mantle, but are unstable on Earth's surface. They are much more common on the surface of Mars, which might have to do with its atmospheric loss [Murray, 2024]. The spectral properties of ultramafic rocks would be very different from those of Earth-like surfaces, with an especially high albedo. This might offer a way to distinguish them observationally [Mansfield et al., 2019].

Igneous rocks are classified by composition and texture using different schemes depending on their formation. Volcanic rocks, which cool quickly at the surface, are classified using the Total Alkali–Silica (TAS) diagram based on alkali ($Na_2O + K_2O$) and silica (SiO_2) content, with felsic rocks like rhyolite plotted on the right and mafic rocks like basalt on the left (Figure 8a). Plutonic rocks, formed from slowly cooling underground magma, are too coarse-grained for this method and instead use the QAPF diagram based on quartz, alkali feldspar, plagioclase, and feldspathoid content (Figure 8b). Ultramafic rocks are classified separately by their mafic mineral content, primarily olivine, orthopyroxene, clinopyroxene, and hornblende, as shown in Figure 8c [Maitre et al., 2004]. The complete Figure 8 with all three classification diagrams can be found on the next page.

Different surface types reflect sunlight and emit thermal radiation differently, influencing the thermal emission spectrum we observe during a planet's secondary eclipse. With the newly launched JWST, recognising spectral signatures of planetary surfaces has become a realistic effort. Being able to distinguish between surface and atmospheric signatures in a planet's spectrum is essential when determining whether a planet has an atmosphere. Moreover, surface mineralogy can give us hints about a planet's interior processes, plate tectonics, and atmospheric history – and, potentially, the (past) presence of liquid water [Herbort and Sereinig, 2025]. Ultimately, identifying exoplanetary surfaces by combining observations with surface models might be crucial in the search for habitable worlds.

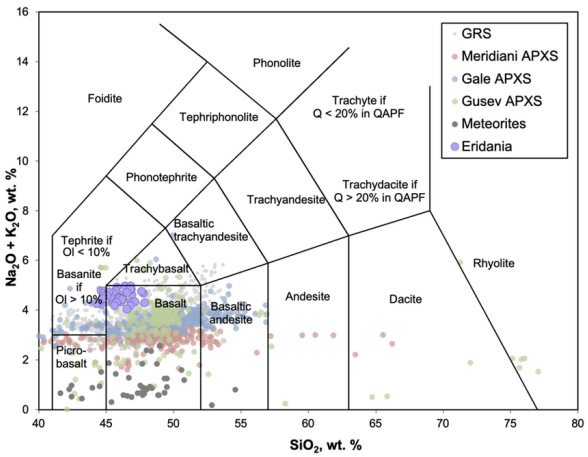

(a) TAS diagram, used to classify volcanic igneous rocks, based on total alkali and silica content. The coloured data points represent Martian rock samples [Hughes et al., 2024].

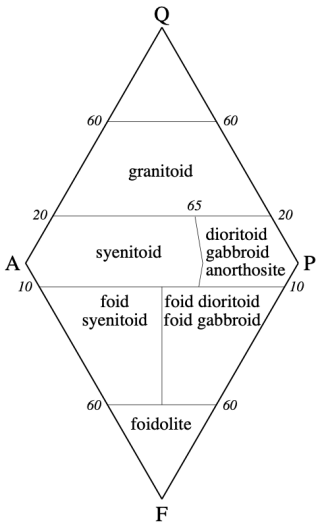

(b) Simplified QAPF diagram, used to classify plutonic igneous rocks by mineral content (quartz, alkali feldspar, plagioclase, and feldspathoids). The numbers represent percentages [Maitre et al., 2004].

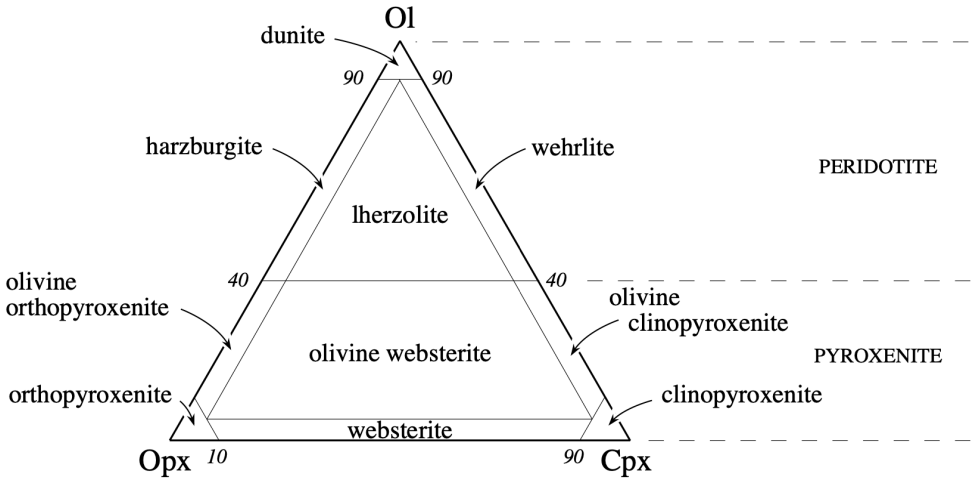

(c) Ternary diagram for ultramafic rocks, based on the proportions of the minerals olivine (Ol), orthopyroxene (Opx), clinopyroxene (Cpx), pyroxene (Px) and hornblende (Hbl) [Maitre et al., 2004].

Figure 8: Examples of classification diagrams for igneous rocks. (a) TAS for volcanic rocks; (b) QAPF for plutonic rocks; (c) Ternary diagram for ultramafic rocks.

2.3 Observing rocky exoplanet atmospheres and surfaces with JWST

In December 2021, the James Webb Space Telescope (JWST) was launched from French Guiana. It is currently the largest telescope in space, with a 6.5-metre-wide mirror that gives it the power to collect very faint light, important for detecting faint atmospheric signals [European Space Agency, 2023]. Webb observes in the infrared, from 0.6 to 28.8 microns, particularly well-suited for exoplanet spectroscopy. Many relevant atmospheric species, including water vapour, carbon dioxide, and methane, have strong absorption features in this wavelength range, making them accessible to detailed study [Lustig-Yaeger et al., 2023].

While for gas giants, atmosphere characterisation has been faring well with the launch of JWST, the detection of atmospheres around rocky exoplanets proves to be more challenging. Rocky planets have small radii and relatively thin atmospheres, producing weak spectral signals easily drowned out by stellar or instrumental noise [Barclay et al., 2025]. Observing rocky planets around the dimmer M-stars might lead to more favourable signal-to-noise ratios, but at the same time, these planets might not be able to retain atmospheres for us to observe [Wordsworth and Kreidberg, 2022]. Nevertheless, methods have been developed to probe the atmospheres – and, if absent, the bare surfaces – of these planets. Techniques applied include transmission spectroscopy, emission spectroscopy and photometry, and, to a lesser extent, phase curve mapping [Mansfield et al., 2019].

2.3.1 Transmission spectroscopy

Transmission spectroscopy is the most commonly used method for observing exoplanet atmospheres. It uses the wavelength-dependent opacity of planetary atmospheres during transits. When a planet passes in front of its host star, the transit depth – how much starlight is blocked by the planet – varies with wavelength due to atmospheric absorption: at wavelengths where atmospheric species absorb strongly, the transit depth increases, as photons are blocked at higher altitudes from the planet's surface. This creates a transmission spectrum showing the planet's apparent radius as a function of wavelength, with absorption features corresponding to atmospheric elements [Rackham et al., 2023].

For rocky exoplanets, however, the small scale height of their atmospheres makes such features very faint. Detecting these signatures requires both extremely stable instruments and favourable target systems – typically M or K stars hosting short-period planets. Even then, disentangling planetary signals from stellar and instrumental contamination is challenging; especially since M stars are known for their stellar variability [Rackham et al., 2023].

Nevertheless, transmission spectroscopy has been applied to rocky (M-star) exoplanets, with moderate success. For the hot super-Earth GJ 486b for instance, of special interest in this thesis, transmission spectroscopy was used to conclude that it likely does not possess a clear H_2 or He atmosphere [Ridden-Harper et al., 2023]. The same goes for Trappist-1h [Garcia et al., 2022], which was observed with the Hubble Space Telescope. Conclusive results, however, are lacking.

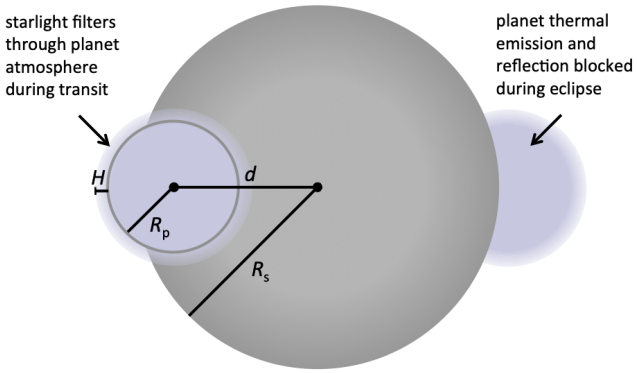

Figure 9: Transmission spectroscopy during a planet's transit (passing in front of the star, starlight filters through atmosphere), and emission spectroscopy or photometry during secondary eclipse (passing behind the star, star blocks planet's thermal emission). R_p and R_s are the planet and stellar radii, H the atmospheric scale height H, and d the separation of centers in the plane of the sky. Taken from Kreidberg [2018].

2.3.2 Emission spectroscopy and photometry

Hot, close-in planets around M-stars are often tidally locked: due to the strong gravitational effect of their star, they continuously face the star with the same side. In this case, emission spectroscopy becomes the most feasible option. It makes use of the planets secondary eclipse, when the planet passes behind its star, to observe its dayside emission and reflection [Wordsworth and Kreidberg, 2022]. Besides finding the absorption features of potential elements in the planet's atmosphere, we can estimate the planet's temperature, to what extent starlight is reflected, and look for surface features. This technique is most promising for hot planets with high equilibrium temperatures, where the contrast between the planet and star is greatest [Xue et al., 2024]. The difference between transmission and emission spectroscopy has been illustrated in Figure 9.

In particular, JWST's mid-infrared sensitivity has enabled opportunities to detect thermal emission from planets. For example, emission spectra from LHS 3844b and GJ 1252b, taken with JWST's NIRSpec instrument, have suggested the absence of substantial atmospheres, consistent with a bare rock surface [Kreidberg et al., 2019, Crossfield et al., 2022].

Additionally, there have been efforts recently to detect a planet's thermal emission using photometry, the F1500W and F1280W photometric filters of JWST's MIRI instrument in particular. The thermal emission of TRAPPIST-1b was observed using the former broadband filter [Greene et al., 2023]. As the signal-to-noise ratio is relatively high in the mid-infrared, observations with the MIRI instrument might be able to detect departures from a blackbody's thermal emission, due to an atmosphere's opacity, albedo, or heat redistribution. Mansfield et al. [2019] suggest that finding a sufficiently high albedo in these broadband filters, higher than expected based on a planet's surface, could point to the presence of an atmosphere. Hammond et al. [2025], on the other hand, show that a significant degeneracy between atmosphere and surface albedo might still exist, especially in individual filters [Hammond et al., 2025].

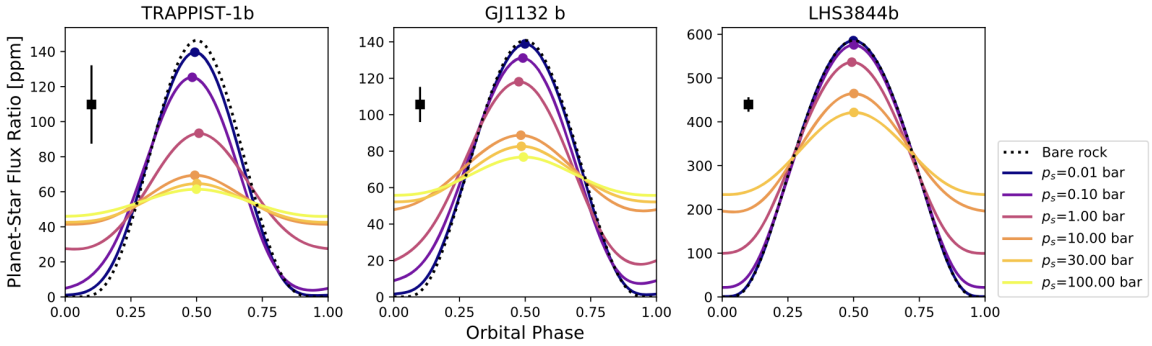

Figure 10: Changes in modelled phase curves for three rocky, tidally locked exoplanets, due to the day-to-nightside heat redistribution of atmospheres of varying pressures. The planet-star contrast is highest at an orbital phase of 0.5, when we observe the planet's dayside; however, the amplitude of this peak diminishes with heat transport [Koll, 2022].

2.3.3 Phase curve mapping

As mentioned in the introduction, when observing a planet's dayside using emission spectroscopy or photometry, it can be difficult to distinguish between surface and atmospheric effects. For instance, a bright, reflective surface (high albedo) may reduce the planet's thermal emission, mimicking the signature of an atmosphere that absorbs heat or redistributes it to the nightside [Hammond et al., 2025]. To break these surface–atmosphere degeneracies, the observation of a planet's phase curve can be very valuable. A phase curve shows the change in light coming from a planet as it orbits its star, looking at both its dayside and its nightside. An airless planet will show a sharp day–night contrast, as heat is not redistributed to the nightside; on the other hand, an atmosphere can redistribute heat and smooth out this contrast, leading to a more gradual phase curve variation [Hammond et al., 2025, Koll, 2022]. This effect has been illustrated in Figure 10.

The shape and amplitude of the phase curve can also provide information about atmospheric albedo and the presence of absorbing gases. For example, Kempton et al. [2023] observed the thermal phase curve of GJ 1214b, a sub-Neptune, to find a thick, high-metallicity atmosphere with potential H_2O features, which could not be seen in transmission spectra due to a thick layer of clouds or haze. Phase curve mapping can, in this way, provide a more complete picture of a planet's thermal structure and potential atmosphere.

2.4 The cosmic shoreline: current status

The cosmic shoreline is a semi-empirical relation that separates bodies with atmospheres from those without, based on the balance between stellar irradiation and gravitational binding energy. Originally proposed by Zahnle and Catling [2017], it suggests that atmospheric retention depends largely on the planet's escape velocity and the amount of bolometric, or XUV, instellation it receives. When plotted on a plane of incident flux versus escape velocity, the boundary dividing planets with and without atmospheres follows an approximate relation of $I \propto v_{\text{esc}}^4$. This simple relation appears to describe Solar System bodies surprisingly well, and is now being tested on exoplanets.

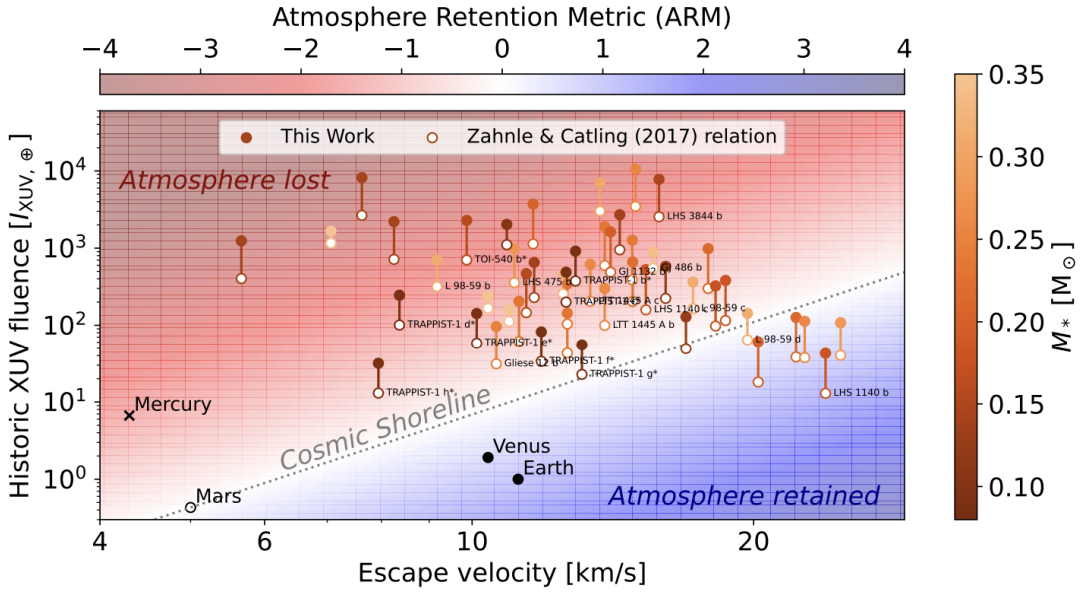

Figure 11: The revisited cosmic shoreline as estimated by Pass et al. [2025] (full circles), compared to the original estimates by Zahnle and Catling [2017] (open circles). The authors estimate higher XUV fluxes for M-stars, making the predicted positions of many exoplanets with respect to the cosmic shoreline move upwards.

In recent years, a growing number of rocky exoplanets near or below the expected shoreline have been observed with JWST and other instruments, allowing for the first empirical constraints on atmospheric presence. Thermal emission observations of TRAPPIST-1b in particular [Ducrot et al., 2025], show that a bare-rock ultramafic surface is a likely scenario. Observations of TRAPPIST-1c [Zieba et al., 2023] also disfavour a thick, CO_2 atmosphere. Similarly, observations of GJ 1252b and LHS 3844b show no atmospheric absorption or thermal phase variation, consistent with atmosphere-free surfaces [Diamond-Lowe et al., 2020, Crossfield et al., 2022]. These results support a receding cosmic shoreline, as estimated by Pass et al. [2025], who predicted the positions of planets with respect to the cosmic shoreline with updated XUV fluxes of M-stars. Compared to earlier predictions by Zahnle and Catling [2017], they suggest that more planets might be airless than expected. This revised shoreline is shown in Figure 11.

Nevertheless, the observational picture remains complex and sometimes contradictory. TRAPPIST-1b has been suggested to possess a thick, hazy CO_2 atmosphere with a temperature inversion, contradicting the notion that it is likely airless [Ducrot et al., 2025]. Similarly, results from Lincowski et al. [2023] are less pessimistic about the atmosphere of TRAPPIST-1c than Zieba et al. [2023]: they show that massive, 1–10 bar O_2 with abundant CO_2 are within 2σ secondary eclipse value. Furthermore, planets like TRAPPIST-1e and GJ 486b [Krissansen-Totton and Fortney, 2022, Moran et al., 2023], which receive less flux or have higher surface gravities, fall closer to or above the expected cosmic shoreline. While their atmospheric status remains inconclusive, they are promising candidates for further investigation.

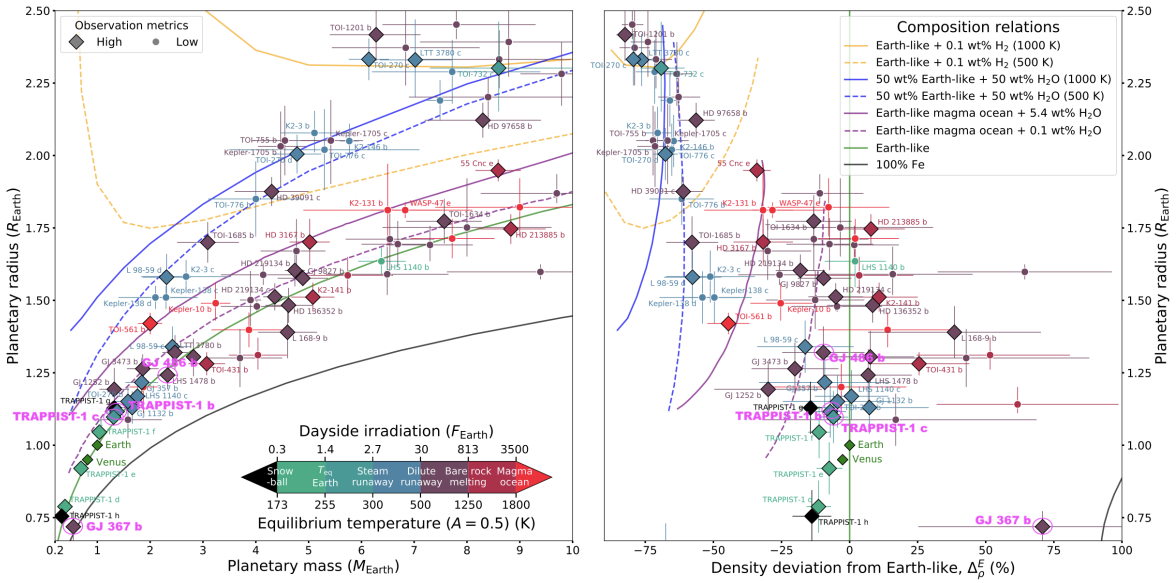

Figure 12: Mass, radius and density of planets GJ 486b, GJ 367b, TRAPPIST-1b and TRAPPIST-1c (highlighted in pink), in the context of other terrestrial (exo)planets . They are plotted together with idealised planetary composition curves. Diamond symbols with attached names indicate planets with high transmission (TSM) or emission (ESM) metrics – meaning they are favourable targets for observation – which is the case for all four planets in this thesis. Figure by Lichtenberg and Miguel [2024].

The planets studied in this thesis are GJ 486b, GJ 367b, and TRAPPIST 1b and 1c. Their mass, radius and density have been shown in the context of other planets in Figure 12. All four planets are small, likely tidally locked, and orbit M-dwarfs – environments where atmospheric loss due to XUV irradiation is expected to be strong. However, they significantly vary in likelihood of an atmosphere, due to their different sizes and temperatures. The planets will be discussed in more detail below.

2.4.1 GJ 486b

GJ 486b is a warm ($T_{eq} \sim 700$ K), rocky exoplanet orbiting a nearby M-dwarf at a distance of approximately 8 parsecs. With a radius of 1.3 $R_\oplus$ and a mass of 2.8 $M_\oplus$, it has a relatively high surface gravity, increasing the likelihood that it may have retained a secondary atmosphere. Its bolometric instellation is moderate, placing it close to the expected boundary of the cosmic shoreline [Trifonov et al., 2021].
Transmission spectroscopy studies with JWST have attempted to detect an atmosphere on GJ 486b, with mixed results. Some spectral features suggest possible H_2O absorption [Moran et al., 2023], although stellar contamination remains a major source of uncertainty. On the other hand, Ridden-Harper et al. [2023] use transmission spectroscopy to find that GJ 486b does not likely possess a pure H_2O atmosphere, nor a He or H_2 atmosphere. Mansfield et al. [2024] use JWST's low-resolution spectroscopy (LRS) of the planet's dayside to conclude that it is very unlikely for the planet to bear a thick atmosphere.

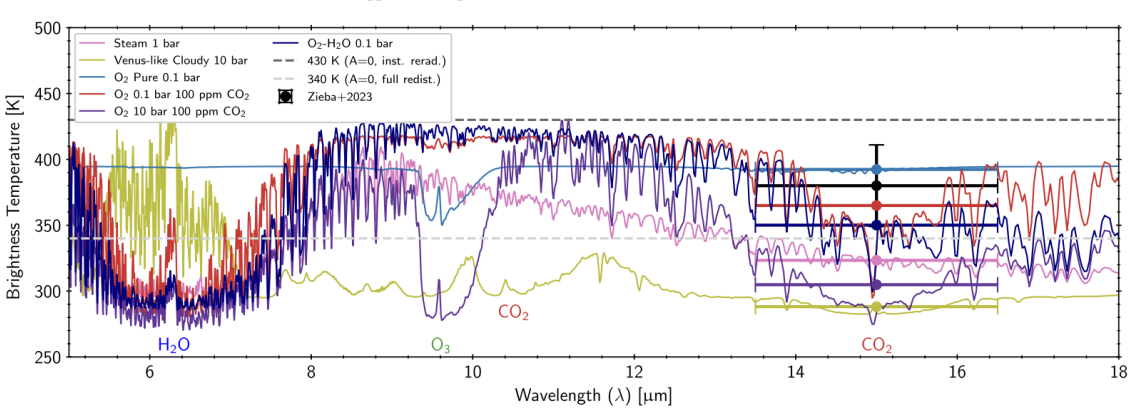

Figure 13: 15 μm observation of TRAPPIST-1c as observed by Zieba et al. [2023], with new atmospheric models by Lincowski et al. [2023]. The authors do not rule out a thick, O_2-CO_2 atmosphere.

2.4.2 GJ 367b

GJ 367b is a small (0.72 $R_\oplus$), dense planet with an extremely short orbital period of just 0.32 days, resulting in a high equilibrium temperature ($T_{\text{eq}} \sim 1400$ K). Its mass and radius imply an iron-rich composition, and possibly a Mercury-like internal structure. Based on its dayside temperature, it could be partially molten [Zhang et al., 2024]. The planet orbits a mid-M dwarf and lies well below the expected cosmic shoreline in both bolometric and XUV instellation space [Lam et al., 2021].

Due to its small size, low gravity, and extreme proximity to its host star, GJ 367b is highly unlikely to have retained a substantial atmosphere [Poppenhaeger et al., 2024]. Zhang et al. [2024] performed low-resolution emission spectroscopy (LRS) with JWST, and concluded that GJ 367b is very likely a bare rock.

In the context of this thesis, GJ 367b represents an end-member: a rocky planet that has almost certainly lost its atmosphere. It is very likely that no atmosphere will be consistent with its data; but it might be an interesting target for the attempt of surface characterization, and it serves as a strong test case for the low end of the cosmic shoreline.

2.4.3 TRAPPIST-1b and 1c

TRAPPIST-1b and TRAPPIST-1c are the two innermost planets in the TRAPPIST-1 system, a system with an ultracool M8-type dwarf located about 12 parsecs from Earth. Both planets are Earth-sized, with radii of 1.12 $R_\oplus$ and 1.10 $R_\oplus$ respectively, and receive significantly more stellar irradiation than Earth [Grimm et al., 2018, Agol et al., 2021]. Given their close proximity to their host star and the star's extended pre-main sequence phase of high luminosity, both planets have likely undergone strong atmospheric escape.

As discussed above, JWST observations have provided direct constraints on the presence of atmospheres for these planets. For TRAPPIST-1b, Ducrot et al. [2025] conducted secondary eclipse photometry using JWST/MIRI. Their results strongly suggest a high-albedo, bare-rock surface, possibly composed of ultramafic minerals; rocks with very low silicate content, as discussed in Section 2.2. A thick, hazy CO_2-dominated atmosphere is also not ruled out by the authors. Furthermore, using the same instrument, Zieba et al. [2023] observed TRAPPIST-

1c's 15 μm secondary eclipse and found that the dayside brightness temperature was consistent with a bare rock surface lacking a significant atmosphere. However, subsequent atmospheric modelling by Lincowski et al. [2023] shows that O_2–CO_2 atmospheres up to 10 bars remain consistent with the data within 2σ confidence, as can be seen in Figure 13. These results show the inherent uncertainties in interpreting single-band eclipse data and the importance of multi-wavelength follow-up.

As the innermost planets of the TRAPPIST-1 system, TRAPPIST-1b and 1c are of particular relevance when it comes to testing atmospheric retention around M-dwarfs. Their location close to the cosmic shoreline makes them good candidates for constraining the boundary between rocky planets with and without atmospheres Zahnle and Catling [2017]. Additionally, since these planets receive the highest irradiation in the system, their atmospheric state may be relevant to the habitability of the outer, more temperate TRAPPIST-1 planets [TRAPPIST-1 JWST Community Initiative, 2024].

3 Methods

This thesis aims to simulate the atmospheres and surfaces of four specific M-star exoplanets: the super-Earth GJ 486b, the hot sub-Earth GJ 367b, and the warm Earth-like planets TRAPPIST-1b and 1c. These models are compared to their mid-infrared JWST data, to assess the likelihood for them to have retained an atmosphere, and if possible, to make constraints on their surfaces. Additionally, I evaluate JWST's sensitivity in distinguishing between bare-rock and atmosphere-bearing scenarios using secondary-eclipse photometry.

For both atmosphere and surface modelling, I use the 1D radiative-convective model named AGNI, developed by Nicholls et al. [2025b]. In the following section, the AGNI model will be described, including its structure, physical assumptions, and the input parameters used for simulating each exoplanet.

3.1 Atmosphere and surface modelling with AGNI

All atmospheric and surface modelling is performed using AGNI, a 1D radiative-convective model developed by Nicholls et al. [2025b]. AGNI solves for the vertical temperature structure of planetary atmospheres by enforcing radiative and convective energy balance. The model is implemented in Julia with radiative transfer handled through the SOCRATES code in Fortran. AGNI can produce emission spectra consistent with its equilibrium solutions, making it well-suited for direct comparison with JWST secondary-eclipse observations.

3.1.1 Model geometry

AGNI treats planetary atmospheres as 1D vertical columns discretized into pressure levels, assuming plane-parallel geometry and hydrostatic equilibrium. The height at each pressure level is calculated by integrating upward from the surface using a fourth-order Runge-Kutta method, that incorporates self-gravity effects.

3.1.2 Radiative transfer

Radiative transfer describes how stellar energy is absorbed, scattered, and re-emitted as it propagates through the atmosphere. This depends on the composition and pressure of the atmosphere, but also on the type of stellar radiation, potential clouds, and the surface of the planet. AGNI implements radiative transfer via the SOCRATES code, originally developed by Edwards and Slingo [1996]. It uses a two-stream solution, where only an upward and a downward radiation stream are considered. Important processes include:

Molecular absorption Opacities are computed using the correlated-k method, where in this thesis, equivalent extinction is used to account for overlapping absorption in mixtures of gases. Opacities are drawn from spectral absorption cross-section data from the DACE opacity database [Grimm et al., 2021]. Water continuum absorption cross-sections are derived using the MT_CKD model, and other continua are taken from HITRAN tables [Mlawer et al., 2023]. Species such as CO_2, H_2O, SO_2, CH_4, N_2, N_2O, HCN, NH_3, O_3, and H_2S are supported.

Rayleigh scattering AGNI includes wavelength-dependent Rayleigh scattering by atmospheric molecules.

Surface interaction For atmospheric simulations, the surface is treated as a grey (blackbody) emitter. For bare-rock modelling, laboratory-measured, wavelength-dependent reflectance spectra from the NASA RELAB database [Milliken et al., 2021] are used for surface reflection, converted to single-scattering albedo values (see Section 3.3.2).

3.1.3 Convection

Convection is a multidimensional process that cannot be simulated in 1D models like AGNI, and is therefore parameterised. AGNI uses mixing length theory (MLT), estimating convective heat flux based on the local temperature gradient and a characteristic mixing length. The mixing length represents the length that gas parcel are diffused over, transporting energy. Energy transport is calculated directly from the instability criterion, requiring the lapse rate dT/dP to exceed the Schwarzschild threshold for convection to occur. The convective flux is computed in the following way [Nicholls et al., 2025a]:

$$F^{\text{conv}} = \frac{1}{2}\rho c_p w T \frac{\lambda}{H}(\nabla - \nabla_{\text{ad}}), \tag{3}$$

with T the local temperature, c_p the mass-specific heat capacity of the gas, w is the characteristic upward velocity defined by:

$$w = \lambda\sqrt{(g/H)(\nabla - \nabla_{\text{ad}})}, \tag{4}$$

where H is the pressure scale height, and ∇ is the local lapse rate, depending on the local temperature T and the local pressure P:

$$\nabla = \frac{d\ln T}{d\ln P}, \tag{5}$$

and finally the dry adiabatic lapse rate ∇_{ad}, with μ the local mean molecular weight of the gas:

$$\nabla_{\text{ad}} = \frac{R}{\mu c_p}. \tag{6}$$

Convective regions are determined locally, so that disconnected regions of convection can exist.

3.1.4 Equilibrium chemistry and transparent atmospheres

AGNI supports both well-mixed and equilibrium chemical compositions. In this thesis, the default, well-mixed atmosphere composition is used. For bare-rock surface modelling, however, the atmosphere is set to 'transparent'. This diminishes its pressure, and disables all absorption processes in SOCRATES. The input wavelength-dependent reflectivity data for a given surface then governs the planet's emission.

f	ε	
$\frac{2}{3}$	0.0	No redistribution
$\frac{9}{16}$	0.25	Weak redistribution
$\frac{11}{24}$	0.5	Semi-redistribution
$\frac{17}{48}$	0.75	Moderate redistribution
$\frac{1}{4}$	1.0	Full (global) redistribution

Table 1: Overview of the heat redistribution factors f used in this thesis, and the corresponding heat redistribution efficiency ε. A redistribution efficiency of 0.50 corresponds to a 50% efficiency of transporting heat to the nightside.

3.1.5 Stellar radiation and heat redistribution

The way the radiation from the star is handled plays a critical role in determining the thermal state of the atmosphere and surface. The stellar flux in AGNI is controlled by the input stellar spectrum scaled to the top of the atmosphere, as well as parameters such as the bolometric instellation flux, an additional albedo factor, a planetary rotation factor and a zenith angle.

Input stellar spectrum To simulate stellar irradiation, AGNI requires an input stellar spectrum scaled to the top of the atmosphere. I apply high-resolution spectra from the PHOENIX stellar library [Husser, T.O. et al., 2013], covering wavelengths from 50 nm to 5 μm. Each model is selected based on the stellar effective temperature, which is listed in Table 2 for the four exoplanets. These spectra define the spectral energy distribution at the top of the atmosphere and directly inform the radiative transfer calculations.

Bolometric instellation (raw) The uncorrected total stellar energy received per unit area (the bolometric instellation flux in W/m^2) at the top of a planet's atmosphere is calculated using:

$$F_{\text{inst,raw}} = \frac{L_\star}{4\pi a^2}, \tag{7}$$

where $L_\star$ is the stellar luminosity and a is the orbital distance of the planet. These values are drawn from literature (Table 2).

Heat redistribution factor Planets with sufficiently thick atmospheres (pressure ≥ 1 bar) can redistribute heat across their surfaces through atmospheric circulation [Koll, 2022]. For tidally locked planets, this process transports energy from the permanently illuminated dayside to the dark nightside. Observationally, this heat redistribution causes the dayside to emit less thermal radiation than would be expected from a simple blackbody calculation [Hammond et al., 2025].

Because AGNI is a 1D model, it cannot explicitly simulate three-dimensional processes like atmospheric circulation. Instead, I apply heat redistribution artificially by scaling the dayside energy budget using a heat redistribution factor f. It ranges from full, isotropic redistribution

($f = 1/4$) to no redistribution ($f = 2/3$), and depends on the heat redistribution efficiency ε according to the parametrisation by [Cowan and Agol, 2011]:

$$f = \frac{2}{3} - \frac{5}{12}\varepsilon, \tag{8}$$

A heat redistribution efficiency of $\varepsilon = 0.25$, for instance, corresponds to 25% redistribution efficiency from the day- to the nightside of the planet. Values for f and ε applied in this thesis are listed in Table 1, allowing for comparison between different redistribution regimes. Unless stated otherwise, a default value of $f = 2/3$ (no redistribution) is assumed.

Scaled instellation When modeling tidally locked planets, the bolometric instellation (incoming stellar radiation) requires two adjustments:

1. **Geometric correction** Since observations typically measure the entire dayside hemisphere while AGNI models only a single point (such as the substellar point), a geometric correction is needed. Rather than directly scaling the instellation, we introduce an effective zenith angle that corresponds to the zero-redistribution, dayside-averaged flux ($f = \frac{2}{3}$):

$$\theta_{\text{zenith}} = \arccos(f) = \arccos\left(\frac{2}{3}\right) \approx 48.19^\circ. \tag{9}$$

   In AGNI, the cosine of this angle automatically scales the incoming stellar flux, while simultaneously regulating the distance light travels through the atmosphere. It represents the average incidence angle across the dayside hemisphere, though it cannot capture the full range of local angles, that would require a three-dimensional model.

2. **Heat redistribution scaling** To account for different redistribution regimes, the instellation is further scaled by the heat redistribution factor described above. To avoid double-counting the geometric factor (once through the zenith angle and once through f), the final scaling becomes:

$$F_{\text{inst,scaled}} = F_{\text{inst,raw}} \cdot \frac{3}{2} \cdot f, \tag{10}$$

   This ensures the flux properly represents the chosen heat redistribution regime.

Surface temperature estimation An initial guess for the surface temperature is required to initiate AGNI's solver. We estimate this using the dayside brightness temperature T_{db}, assuming zero Bond albedo ($A_B = 0$) and incorporating the redistribution factor f:

$$T_{\text{db}} = T_\star \sqrt{\frac{R_\star}{a}} \cdot f^{1/4}. \tag{11}$$

This estimate provides a physically motivated initial condition for both atmosphere and surface simulations. The redistribution factor f used in each model run is explicitly stated.

3.1.6 Solving algorithm

AGNI solves for the temperature structure of the atmosphere using optimisation, finding the state which conserves energy throughout the atmosphere column. The residual minimisation process uses Newton-Raphson iterations, optionally modified by Gauss-Newton or Levenberg–Marquardt methods, and includes safeguards to ensure convergence in non-linear regimes. In this thesis, I use solution option (3), which solves for a state such that the flux carried at each level is equal to:

$$F_{\text{int}} = \sigma T_{\text{int}}^4. \tag{12}$$

Both the surface temperature and the temperature of the rest of the atmosphere are, in this case, free to change; radiative equilibrium is what is solved for. This also naturally captures the greenhouse effect.

3.1.7 Stellar and planetary parameters

The stellar and planetary parameters used in AGNI for each of the modelled planets are listed in Table 2.

	GJ 486b	**GJ 367b**	**TRAPPIST-1b**	**TRAPPIST-1c**
		Stellar parameters		
Spectral type	M3.5V	M1.0V	M8V	M8V
$T_\star$ [K]	3317^{+36}_{-37}	3522 ± 70	2566 ± 26	2566 ± 26
$R_\star$ [$R_\odot$]	$0.3243^{+0.0044}_{-0.0034}$	0.458 ± 0.013	0.1192 ± 0.0013	0.1192 ± 0.0013
$\log_{10}(L_\star/L_\odot)$	$-1.939^{+0.017}_{-0.018}$	–1.54 ± 0.04	$-3.26^{+0.01}_{-0.02}$	$-3.26^{+0.01}_{-0.02}$
Distance [pc]	8.074 ± 0.004	9.413 ± 0.003	12.430 ± 0.019	12.430 ± 0.019
[Fe/H]	$-0.15^{+0.13}_{-0.12}$	–0.01 ± 0.12	0.05 ± 0.09	0.05 ± 0.09
$\log g$ [cgs]	$4.911^{+0.007}_{-0.011}$	4.776 ± 0.026	$5.240^{+0.006}_{-0.007}$	$5.240^{+0.006}_{-0.007}$
		Planetary parameters		
R_p [$R_\oplus$]	$1.289^{+0.019}_{-0.014}$	0.699 ± 0.024	$1.116^{+0.014}_{-0.012}$	$1.097^{+0.014}_{-0.012}$
M_p [$M_\oplus$]	$2.770^{+0.076}_{-0.073}$	0.633 ± 0.050	1.374 ± 0.069	1.308 ± 0.056
a [AU]	0.01714 ± 0.00013	0.00709 ± 0.00027	0.01154 ± 0.00010	0.01580 ± 0.00013
P [days]	$1.4671213^{+0.0000003}_{-0.0000004}$	0.3219225 ± 0.0000002	1.510826 ± 0.000006	2.421937 ± 0.000018
T_{eq} [K]	$696.3^{+7.2}_{-7.3}$	1365 ± 32	397.6 ± 3.8	340 ± 3.3

Table 2: Stellar and planetary parameters, with uncertainties, for the four exoplanets modelled with AGNI. Parameters are sourced from Mansfield et al. [2024] for GJ 486b, Goffo et al. [2023] for GJ 367b, and Agol et al. [2021] and Ducrot et al. [2020] for TRAPPIST-1b and TRAPPIST-1c.

3.1.8 AGNI configuration

A complete summary of the configuration parameters for AGNI is shown in Table 3.

Parameter	Atmosphere	Surface	Comments
`tmp_surf`	T_{db}	T_{db}	Initial surface temperature in K
`instellation`	$F_{\text{inst,scaled}}$	$F_{\text{inst,scaled}}$	Bolometric stellar flux at TOA (W/m²)
`albedo_b`	0.0	0.0	Bond albedo
`s0_fact`	1.0	1.0	Rotation scaling factor (no rotation)
`zenith_angle`	48.19	48.19	Characteristic zenith angle in degrees
`surface_material`	greybody	[surface file]	Type of surface
`albedo_s`	0.0	0.0	Spectrally-grey surface albedo
`flux_int`	0.0	0.0	Internal heat flux
`turb_coeff`	0.001	0.001	Turbulent mixing coefficient
`wind_speed`	2.0	2.0	Zonal wind speed in m/s
`chemistry`	0	0	No coupling with FastChem, well-mixed
`transparent`	false	true	Transparent atmosphere
`continua`	true	true	Include continuum absorption
`rayleigh`	true	true	Include Rayleigh scattering
`cloud`	false	false	Clouds disabled
`aerosol`	false	false	Aerosols disabled
`overlap_method`	ee	ee	Equivalent extinction (overlapping gases)
`real_gas`	true	true	Use real EOS when possible
`thermo_funct`	true	true	Temperature-dependent thermodynamics
`sensible_heat`	true	true	Surface sensible heat flux enabled
`latent_heat`	false	false	Latent heat transport disabled
`convection`	true	true	MLT convection enabled
`rainout`	false	false	No rainout or condensation
`solution_type`	3	3	Radiative equilibrium, free surface temp.
`solver`	gauss	gauss	Gauss-Newton solver
`initial_state`	[“iso”, “1200”]	[“iso”, “1200”]	Isothermal initial guess at 1200 K

Table 3: Summary of relevant AGNI configuration parameters for the simulation of planetary atmospheres and bare-rock surfaces. Pressures and compositions are not included, as they are modified for each atmosphere.

3.2 Eclipse depth calculation

AGNI outputs the planet's flux at the top of the atmosphere, separated into longwave and shortwave components. To compare these outputs with JWST secondary-eclipse data, they must be converted to a star-planet contrast (secondary eclipse depth) in parts per million (ppm). The secondary eclipse depth δ_λ at a given wavelength is computed as:

$$\delta_\lambda = \frac{F_p(\lambda)}{F_\star(\lambda)} \left(\frac{R_p}{R_\star}\right)^2 \times 10^6 \quad \text{[ppm]}, \tag{13}$$

where $F_p(\lambda)$ is the spectral flux density of the planet at the top of the atmosphere, $F_\star(\lambda)$ is the spectral flux density of the host star, R_p is the planetary radius and $R_\star$ is the stellar radius.

For the stellar spectrum $F_\star(\lambda)$ of the stars GJ 486, GJ 367, and TRAPPIST-1, I use SPHINX M-dwarf synthetic spectra. These spectra have a lower resolution than the PHOENIX simulations used in AGNI, but have a wavelength range beyond 5 μm. They are specifically tailored to M-dwarfs, making them more accurate than PHOENIX spectra at longer wavelengths [Iyer et al., 2023, Ih et al., 2023]. As SPHINX spectra have a temperature step size of 100 K, both spectra are interpolated to the correct effective temperature of the star (3317 K, 3522 K and 2566 K for GJ 486b, GJ 367B, and TRAPPIST-1 respectively).

The modelled atmospheric and/or surface spectra are compared to the planet's blackbody emission at the dayside brightness temperature T_{db} (Equation 11), in which case:

$$F_p(\lambda) = \pi B(\lambda, T_{\text{db}}), \tag{14}$$

with:

$$B(\lambda, T) = \frac{2hc^2}{\lambda^5} \cdot \frac{1}{\exp\left(\frac{hc}{\lambda k_B T}\right) - 1}, \tag{15}$$

where h is Planck's constant, c is the speed of light, k_B is Boltzmann's constant, and λ is the wavelength in meters.

3.3 Surfaces and atmospheres used

This section outlines the surface types and atmospheric compositions used in the planetary models. Surface and atmospheric properties are selected to reflect plausible rocky exoplanet scenarios, within the constraints of available data and model capabilities.

3.3.1 Atmospheres

The set of atmospheric compositions modelled in this thesis (Figure 14) is chosen to represent a physically motivated range of volatile-rich rocky exoplanet atmospheres, while constrained by the opacities currently available in AGNI and by computational limitations. These compositions include pure atmospheres of CO_2, SO_2, CH_4, and H_2O, as well as N_2-dominated mixtures with traces of CO_2, SO_2, CH_4, H_2O, and, in the case of GJ 468b, also H_2S, CO, HCN, and NH_3.

As discussed earlier, the redox state of a planet's interior is the main control on atmospheric composition. Under oxidizing conditions, degassing leads to volatiles like CO_2 and H_2O, which

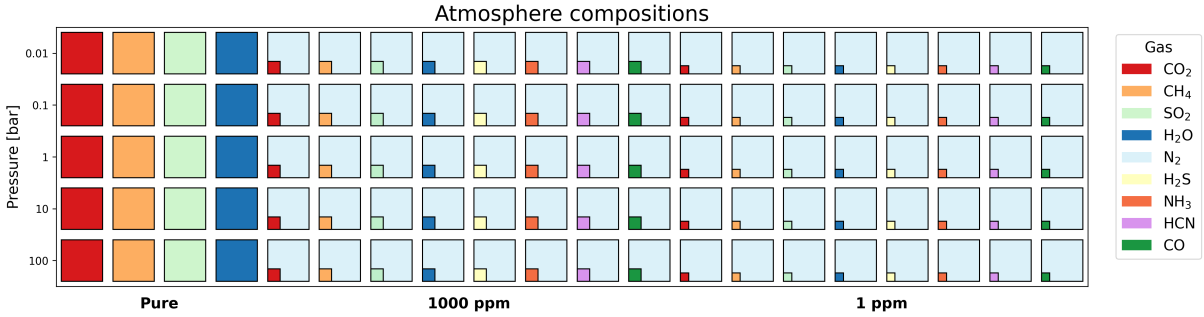

Figure 14: Atmosphere compositions used in this thesis for the planet GJ 486b. GJ 367b and TRAPPIST-1b /1c are modelled with a slightly smaller range of compositions, with H_2S, NH_3, CO and HCN left out. Ratios are not to scale.

dominate terrestrial volcanic outgassing on Earth and Venus. Reduced mantles (near the IW buffer or lower) suppress CO_2 and favour more reduced species such as CH_4, CO, and H_2 [Ortenzi et al., 2020]. Sulfur compounds, such as the oxidized SO_2 and the reduced H_2S, are commonly outgassed from volcanic surfaces, and abundant on Venus [Hu et al., 2013]. Janssen et al. [2023] show that sulfur-bearing atmospheres are expected to be typical for hot, rocky exoplanets.

N_2 is the most common gas in the Earth's atmosphere, and is even more abundant in Titan's atmosphere [Wordsworth and Kreidberg, 2022]. It is a rather transparent molecule to find in an atmosphere Rothman et al. [2013]; the presence of nitrogen should, therefore, allow a planet to have a thick ($>$ 10 bar) atmosphere with relatively little absorption features, making it very relevant in the context of this thesis. The addition of traces of other elements allows for some opacity, and can be interesting for other reasons: HCN, for example, is a prebiotic molecule, produced efficiently in CH_4–N_2 or CO–N_2 atmospheres via UV irradiation or lightning [Wordsworth and Kreidberg, 2022]. Additionally, NH_3 has been suggested as a biosignature, although its effectiveness is still under discussion [Huang et al., 2022].

Figure 15 shows the expected atmospheric regimes for rocky exoplanets based on equilibrium temperature and radius. For the warm to hot planets in this study, CO_2, H_2O, O_2 and SO_2 are the most likely dominant constituents according to this framework. However, I take a broader approach by also including N_2-dominated and CH_4-rich atmospheres in my main focus, to explore a wider range of plausible scenarios, especially given the uncertainties in planetary evolution theories.

Unfortunately, AGNI currently lacks opacity data for O_2 and some other species relevant to rocky exoplanets, such as SiO, Na, and Fe that dominate ultra-hot atmospheres. While our target planets are too cool for significant amounts of the last three elements, the absence of O_2 opacities is an important limitation of this study.

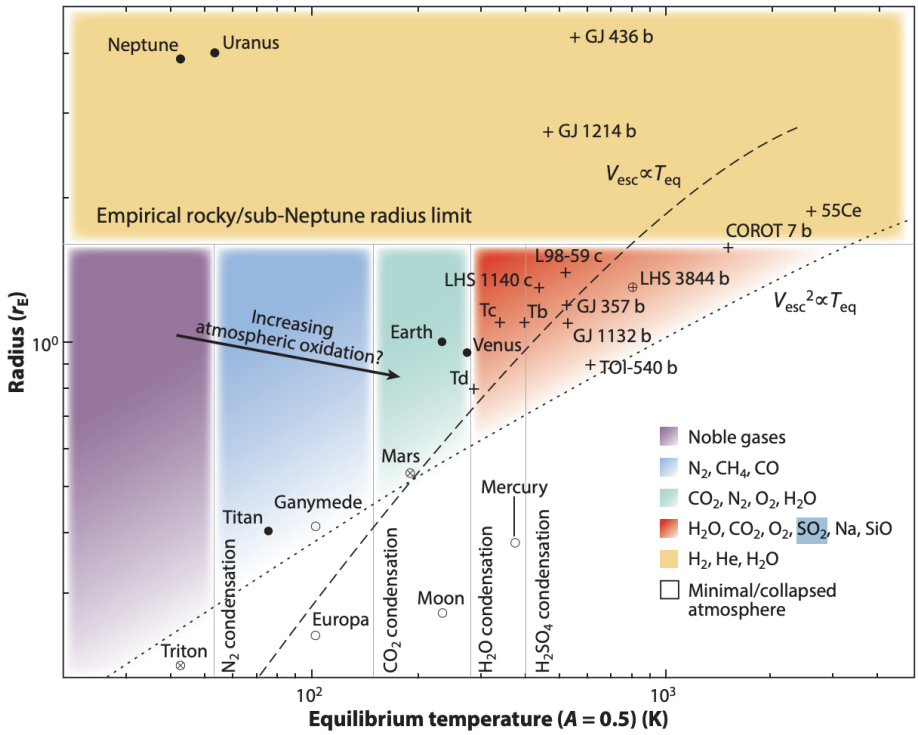

Figure 15: Proposed atmospheric regime diagram for rocky planets as a function of equilibrium temperature and radius. Filled circles show Solar System bodies with stable atmospheres, crossed circles indicate collapsed atmospheres, and open circles represent airless bodies. Plus signs mark show rocky exoplanets, with Tb, Tc and Td as abbreviations for TRAPPIST-1b, c and d. Dashed lines represent theoretical boundaries for atmospheric loss (cosmic shorelines). Taken from Wordsworth and Kreidberg [2022].

3.3.2 Surfaces

I select surface compositions to represent a wide range of rocky exoplanet scenarios, using laboratory-measured reflectance spectra from the NASA RELAB database [Milliken et al., 2021]. The raw reflection factors provided by RELAB are converted to single-scattering albedo using the method provided by Hammond et al. [2025]. Following their study, I focus on rock types with well-characterized spectral properties and plausible origins for airless rocky exoplanets.

My surface selection includes volcanic and plutonic igneous rocks ranging from mafic to felsic compositions, ultramafic mantle-derived materials, extraterrestrial samples, and rocks modified by metamorphism and weathering. These surfaces span Bond albedos from ~ 0.3 to 0.9, allowing me to test how surface reflectivity and atmospheric opacity create degeneracies in secondary-eclipse spectra. Each surface is characterised by its RELAB identifier, grain size, geological origin, and effective Bond albedo under TRAPPIST-1-like illumination (Table 4).

This surface sample, while broad, is not exhaustive. Other potentially important surface types, such as high-temperature lavas, heavily altered rocks, or space-weathered materials, could produce distinct spectral signatures not captured in this work.

Surface	RELAB Data	Grain Size	Petrogenesis	A_B
Volcanic igneous rocks				
Tephrite	AN-G1M-006-B, c1an06b, bir1an006b	36–80 μm	Volcanic igneous rock	0.53
Phonolite	AN-G1M-012-B, c1an12b, bir1an012b	36–80 μm	Volcanic igneous rock	0.53
Trachyte	AN-G1M-018-B, c1an18b, bir1an018b	36–80 μm	Volcanic igneous rock	0.47
Andesite	AD-REA-003-W, cwad03, n1ad03w	Slab	Volcanic igneous rock	0.40
Rhyolite	AN-G1M-010-A, c1an10a, bir1an010a	<63 μm	Volcanic igneous rock	0.71
Basalt (large grain)	AN-G1M-008-C, c2an08c, bir1an008c	80–160 μm	Volcanic igneous rock	0.45
Basalt (small grain)	AN-G1M-008-B, c1an08b, bir1an008b	36–80 μm	Volcanic igneous rock	0.77
Lunar mare basalt	LS-CMP-001, n1ls01, s1ls01	<500 μm	Volcanic igneous rock	0.34
Tholeiitic basalt	RB-CMP-037, c1rb37, bir1rb037	Slab	Volcanic igneous rock	0.34
Basalt glass	BE-JFM-060, c1be60, birlbe060	<25 μm	Volcanic igneous rock	0.62
Pyroclastic rocks				
Basalt tuff	BU-WHF-030, c1bu30, bir1bu030	<400 μm	Pyroclastic ejecta	0.57
Plutonic igneous rocks				
Gabbro	HK-H1T-001, c1hk01, birlhk001	<2000 μm	Plutonic igneous rock	0.60
Diorite	AN-G1M-017-A, c1an17a, bir1an017a	<35 μm	Plutonic igneous rock	0.68
Granite	AN-G1M-011-A, c1an11a, bir1an011a	<63 μm	Plutonic igneous rock	0.67
Norite	AN-G1M-019-B, c1an19b, bir1an019b	36–80 μm	Plutonic igneous rock	0.45
Ultramafic rocks				
Harzburgite	FB-JFM-040-P, cpbf40, nafb40p	25–500 μm	Mantle residue	0.69
Lherzolite	FB-JFM-008-P, cpfb08, nafb8p	25–500 μm	Fertile mantle	0.58
Extraterrestrial rocks and other minerals				
Martian basaltic shergottite	DD-MDD-028, c1dd28, bir2dd028	<50 μm	Igneous rock	0.50
Martian breccia	MT-JFM-263, camt263, biramt263	Slab	Impact breccia	0.38
Lunar anorthosite	LR-CMP-224, c1lr224, bir1lr224	<125 μm	Primitive flotation crust	0.82
Albite dust	albite_ALI	<1.6 μm	Varies	0.90
Magnesium sulfate	CC-JFM-019, c1lc19, s1cc19	<25 μm	Varies	0.81
Pyrite	pyrite_SA-25G	<0.03 μm	Varies	0.34
Hematite	hematite_SA-500G	<0.03 μm	Varies	0.55

Table 4: Surface types used for surface modelling, together with RELAB Data identifiers, grain size, origin, and Bond albedos taken from Hammond et al. [2025]. The Bond albedos were calculated based on the incoming stellar spectrum of TRAPPIST-1, and might significantly differ for other planets. Therefore, the relative Bond albedo with respect to other surfaces is most relevant. All surfaces have been categorised based on rock type, which was explained in more detail in 2.2. Pyroclastic rocks, which were not mentioned before, are rocks that originate from violent volcanic eruptions.

3.4 Bayesian model comparison to JWST data

The AGNI models are compared to recently published JWST data for the four planets. For GJ 486b, this is secondary eclipse data between 5 and 12 μm, gathered using the Low Resolution Spectroscopy (LRS) observing mode of JWST's Mid-infrared Instrument (MIRI) and published by Mansfield et al. [2024]. For GJ 367b, this is MIRI/LRS data at the same wavelengths, published by Zhang et al. [2024]. For TRAPPIST-1b, these are MIRI photometric observations in the F1500W and F1280W broadband filters, presented by Ducrot et al. [2025]; and finally, for TRAPPIST-1c, this is an observation in the F1500W band by Zieba et al. [2023].

To quantitatively compare AGNI model outputs to observed secondary-eclipse data, I adopt a Bayesian model selection framework in line with the method used by Zhang et al. [2024]. Specifically, the Bayesian evidence of each model is calculated, defined as the integral of the likelihood over the prior parameter space, using the `dynesty` nested sampling algorithm [Speagle, 2020].

Each model generated by AGNI is compared to the observed contrast spectrum using a single free parameter: a scaling factor that multiplies the model contrast before comparison. This factor accounts for measurement uncertainties in the stellar flux, the planet–star radius ratio, the semimajor axis, and instrument calibration. Following Zhang et al. [2024], the scaling factor, α, is given a Gaussian prior centered at 1.0 with a standard deviation derived from the quadrature sum of relevant system parameters: planet cross-sectional area, orbital distance, and a flux calibration error of 3%. That is:

$$\alpha \sim \mathcal{N}(1.0,\, \sigma^2), \tag{16}$$

with $\sigma = 0.077$ for GJ 367b, $\sigma = 0.042$ for GJ 486b, and $\sigma = 0.040$ for both TRAPPIST-1b and TRAPPIST-1c.

The log-likelihood is computed by comparing the scaled model contrast to the data, interpolated to the observed wavelength grid:

$$\ln \mathcal{L} = -\frac{1}{2} \sum_i \left(\frac{\delta_{\text{obs},i} - \alpha \cdot \delta_{\text{mod},i}}{\sigma_i} \right)^2, \tag{17}$$

where $\delta_{\text{obs},i}$ are the observed contrasts, $\delta_{\text{mod},i}$ are the modelled values, and σ_i are the observational uncertainties.

The output of `dynesty` is the log evidence $\log Z$ for each model. These are compared relative to a reference model using the Bayes factor:

$$\Delta \ln Z = \ln Z_{\text{model}} - \ln Z_{\text{ref}}, \tag{18}$$

$$\text{Bayes factor} = \exp(\Delta \ln Z). \tag{19}$$

The reference model used in each case is the best-fitting surface for that planet. Models with $\Delta \ln Z < -3$ (equivalent to a Bayes factor < 0.05) are considered strongly disfavoured by the data.

3.5 Simulating photometric observations with JWST

As an initial step in the roadmap for atmospheric characterization of rocky exoplanets with JWST, emission observations using the MIRI instrument are strongly recommended [TRAPPIST-1 JWST Community Initiative, 2024, Hammond et al., 2025]. In particular, MIRI imaging through the 12.8 μm and 15 μm filters, F1280W and F1500W, is frequently used to probe absorption features of CO_2 in exoplanetary atmospheres [Ducrot et al., 2025]. Observations in the 15 μm band specifically are encouraged to look for CO_2 absorption features. On top of that, signal-to-noise ratios for MIRI observations are highest around this wavelength [Redfield et al., 2024].

In this thesis, I generate simulated secondary eclipse signals for GJ 367b and GJ 486b, the two planets which have not yet been observed with MIRI photometry, in the F1280W and F1500W broadband filters of the MIRI instrument, shown in Figure 17. In this way, I aim to assess JWST's sensitivity in distinguishing between bare-rock surfaces and atmosphere-bearing scenarios. Each planet is modelled using the full set of atmospheric compositions and surface types described in Section 3.3.

The planet's emergent flux, modelled with AGNI, is interpolated to a common wavelength grid between 10 and 20 μm. This flux is scaled by the apparent solid angle of the planet, given by $\pi(R_p/d)^2$, where R_p is the planetary radius and d is the distance from the planetary system. This has been illustrated in Figure Similarly, a reference blackbody spectrum is computed at the planet's dayside brightness temperature and normalized using the same solid angle.

The relative photometric emission is then evaluated for each MIRI filter (F1280W and F1500W) by integrating both the model flux and the blackbody flux over the instrument throughput curve:

$$F_{\text{filter}} = \int F_\lambda(\lambda) \cdot T(\lambda)\, d\lambda, \tag{20}$$

where $F_\lambda(\lambda)$ is the spectral flux density and $T(\lambda)$ is the filter throughput, which we obtain using the throughput calculator of the JWST exposure time calculator `pandeia` [Pickering et al., 2016]. The relative emission is defined as the ratio of the model-integrated flux to the corresponding blackbody-integrated flux.

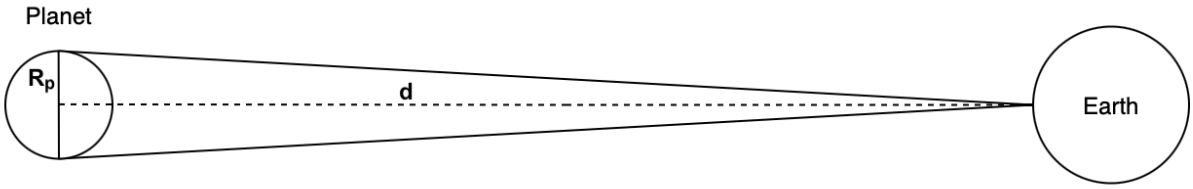

Figure 16: Simple illustration of the solid angle scaling of the planet, with R_p the planet radius, and d the system distance between the planet and the Earth. The cone shows how JWST observes the planet's flux. The solid angle of the planet is given by $\Omega = \pi(R_p/d)^2$.

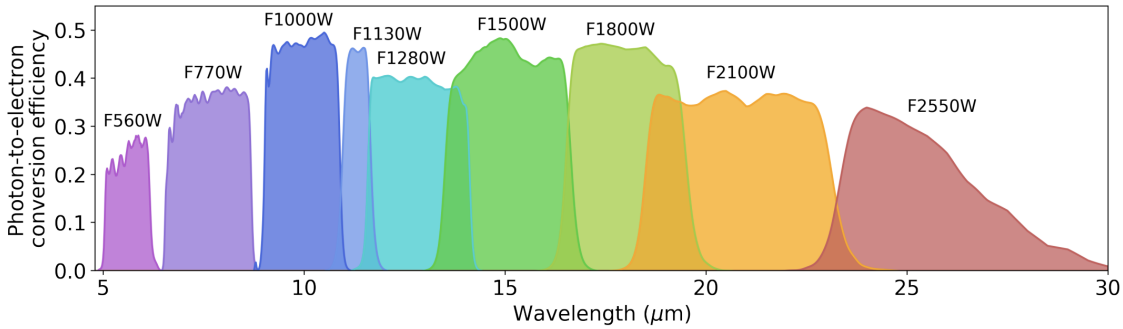

Figure 17: MIRI imaging filter bandpasses, including the F1280W and F1500W bands around 12.8 and 15.0 μm [Dicken et al., 2024]

To estimate detectability, the signal-to-noise ratio (SNR) for each filter is calculated by estimating the photon count rates from the planet, host star, and telescope background. The photon rate is given by:

$$N_\gamma = \frac{F_\lambda \cdot \Delta\lambda \cdot \lambda}{hc} \cdot T(\lambda) \cdot A, \tag{21}$$

where h is Planck's constant, c is the speed of light, $T(\lambda)$ is the filter throughput, A is the JWST collecting area, and $\Delta\lambda$ is the bandwidth of integration.

The total noise includes contributions from photon noise of the star and planet, thermal background from JWST optics, and detector read noise. The resulting signal-to-noise ratio is expressed as:

$$\text{SNR} = \frac{N_p}{\sqrt{\left(1 + \frac{1}{n_{\text{out}}}\right) N_s + \frac{1}{n_{\text{out}}} N_p + \left(1 + \frac{1}{n_{\text{out}}}\right) N_b}}, \tag{22}$$

where N_p, N_s, and N_b are the photon counts from the planet, star, and background, respectively, and n_{out} is the number of out-of-eclipse measurements.

We simulate the photometric emission for four eclipses, which is the amount of eclipses observed for the 15 μm emission of TRAPPIST-1c [Zieba et al., 2023]. Each scenario is compared to the blackbody reference. To reach a realistic uncertainty estimate, a scaling factor is applied based on JWST's TRAPPIST-1c measurement in the F1500W filter by Zieba et al. [2023].

4 Results

This chapter presents spectral modelling results for the M-dwarf rocky exoplanets GJ 486b, GJ 367b, and TRAPPIST-1b and 1c. For each planet, I evaluate a comprehensive range of surface and atmospheric scenarios by comparing modelled emission spectra to JWST mid-infrared observations. Using the Bayesian model selection framework outlined in Section 3.4, I identify scenarios consistent with the observational data and quantitatively rule out highly improbable atmospheric compositions.

Furthermore, I incorporate different heat redistribution regimes across a selection of atmospheric compositions, as detailed in Section 3.1.5. While I use a simplified scaling approach to approximate heat transport, it captures the first-order impact of atmospheric circulation, allowing for a more realistic approach than simple dayside modelling.

Finally, for GJ 486b and GJ 367b, which lack existing MIRI imaging observations, I simulate emission spectra in the JWST MIRI broadband filters at 12.8 and 15 μm. These simulations show to what extent future photometric observations can distinguish between competing atmospheric models, and whether it could potentially exclude a bare-rock hypothesis for these planets.

4.1 GJ 486b

GJ 486b is one of the few rocky planets with available mid-infrared emission measurements from JWST. Its zero-albedo, zero-redistribution dayside brightness temperature of $\sim$ 890 K is relatively high; however, it is considered one of the best candidates for retaining a secondary atmosphere produced by degassing [Meier et al., 2024]. In the next sections, we will compare a range of surface compositions and atmospheric models to GJ 486 b's measured eclipse depths by Mansfield et al. [2024].

4.1.1 Surface models

Figure 18 shows modelled emission spectra for GJ 486b for the four best, and four worst performing surface models. The best performing surface, hematite, was used as a reference model. Models with a Bayes factor above 0.05 (Δln Z > -3) were considered acceptable, and shown in blue; below 0.05, models were rejected, and shown in red. The (frequentist) reduced chi-squared values have been shown here as well.

Figure 19 shows an overview of the Bayes factors, with respect to the best-performing model hematite, of all surface modelled for GJ 486b. In black, the Δln Z = -3 boundary is shown. Surfaces with Bayes factors below this boundary are considered extremely unlikely for this planet.

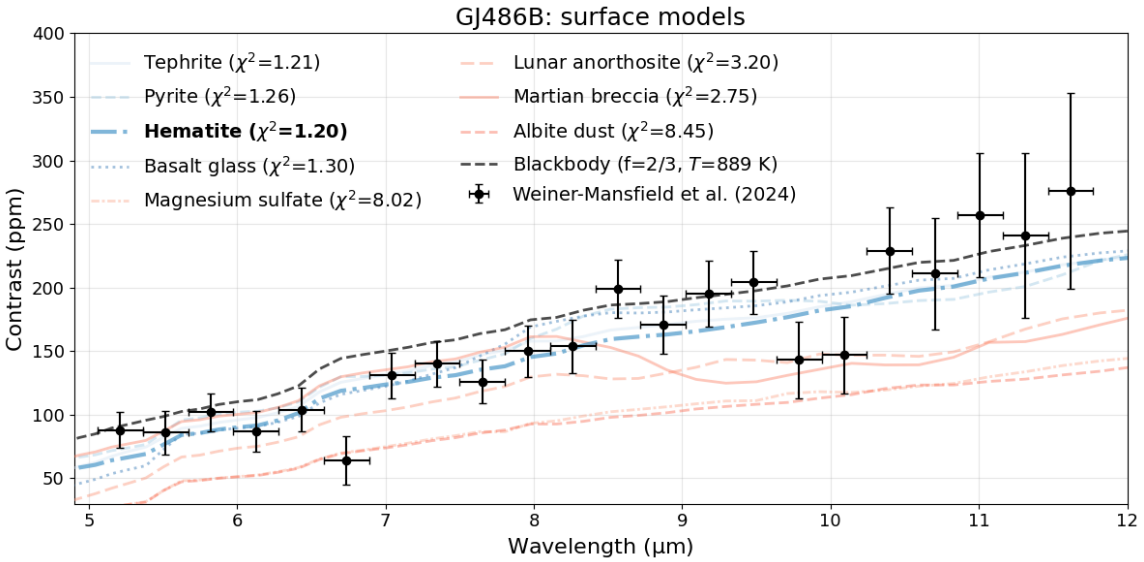

Figure 18: Eclipse depths (here: contrast) in ppm for the four best and four worst performing surface models for GJ 486b, together with their chi-squared value for a quick impression. Models were compared using a Bayesian selection technique. Accepted models (Δ ln Z > -3) are shown in blue, rejected (Δ ln Z < -3) in red. Secondary eclipse depth data by Mansfield et al. [2024].

While a subset of surfaces can be excluded with confidence, we see that many surfaces fit the data moderately well. None of the surfaces reflect all features in the data exactly; instead, relatively featureless surfaces with an appropriate Bond albedo are favoured. Hematite, the best performing model, has a Bond albedo of 0.55 (Hammond et al. [2025], based on Trappist-1's irradiation). Pyrite has a relatively low albedo ($A_B = 0.34$) in comparison with hematite and tephrite ($A_B = 0.53$), but its shape seems to better fit the data at higher wavelengths. High-albedo surfaces, such as albite dust, Martian breccia, or magnesium sulfate, fit very poorly. Table 6 in Appendix A.1.2 summarises the Bayesian comparison of surface models.

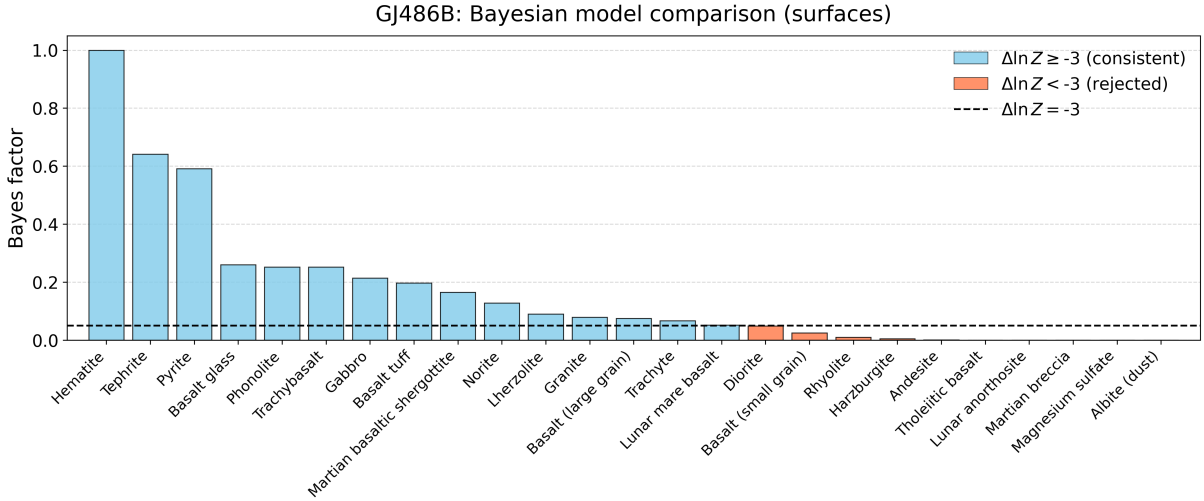

Figure 19: Bayes factors for all surface models applied to the GJ 486b data. Accepted models (Δ ln Z > -3) are shown in blue, rejected (Δ ln Z < -3) in red.

4.1.2 Atmosphere models

As discussed in section 3.3.1, GJ 486b was modelled with the largest range of atmosphere compositions used in this thesis. I evaluated pure CO_2, H_2O, SO_2, and CH_4 atmospheres, as well as N_2 atmospheres with 1 ppm and 1000 ppm traces of CO_2, H_2O, SO_2, CH_4, HCN, CO, NH_3 and H_2S. Figure 20, 21 and Figure 22 show the modelled eclipse depth for each atmosphere composition, together with the eclipse depth data from Mansfield et al. [2024]. Each panel shows the three best, and three worst performing models for each surface pressure (0.01 to 100 bar). Models considered consistent with the data are shown in blue (Δ ln Z > -3), and models inconsistent with the data (Δ ln Z < -3) are shown in red. The Bayesian model comparison was performed with the best-performing surface hematite as a reference model (see Section 4.1.1). The performance of each model can also be found in Table 7 (pure atmospheres), Table 8 (N_2 atmospheres with 1 ppm trace elements) and Table 9 (N_2 atmospheres with 1000 ppm trace elements) of Appendix A.1.2.

H_2O-rich atmospheres consistently provide the best fits across pressure regimes; a pure H_2O atmosphere remains consistent with the data up to a surface pressure of 100 bar. The shape of these steam atmospheres varies little for different pressures. Possibly, the increase in opacity is compensated for by an increase in atmosphere temperature, keeping the emission stable. The highest-pressure steam atmosphere (100 bar), for instance, doubles the bare-rock dayside-brightness temperature to 1816 K.

The water-dominated atmospheres have larger overall slopes than the zero heat-distribution blackbody, making them more consistent with the data in the whole range of wavelengths. Interestingly, however, while low-pressure N_2 with 1000 ppm H_2O atmospheres fit the data very well, at 1, 10 and 100 bar they are all inconsistent with the data. This suggests that if GJ 486b possesses a thick, water-rich atmosphere, the H_2O concentration is very high.

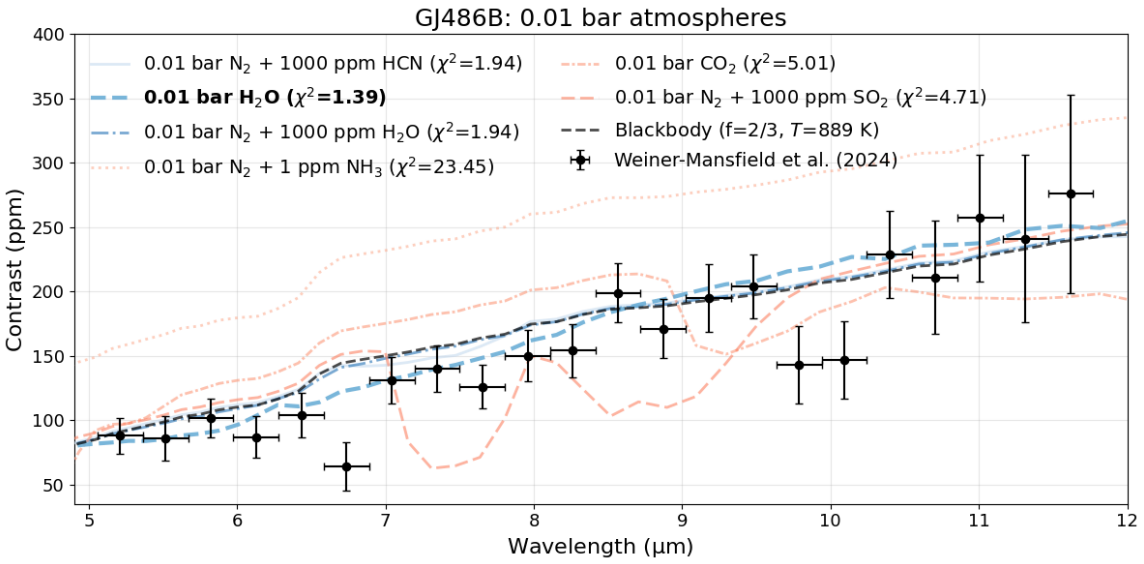

Figure 20: Three best and three worst performing models for GJ 486b, at 0.01 bar, with the data by Mansfield et al. [2024]. Models in red can be rejected (Δ ln Z < -3), models in blue are considered acceptable (Δ ln Z > -3).

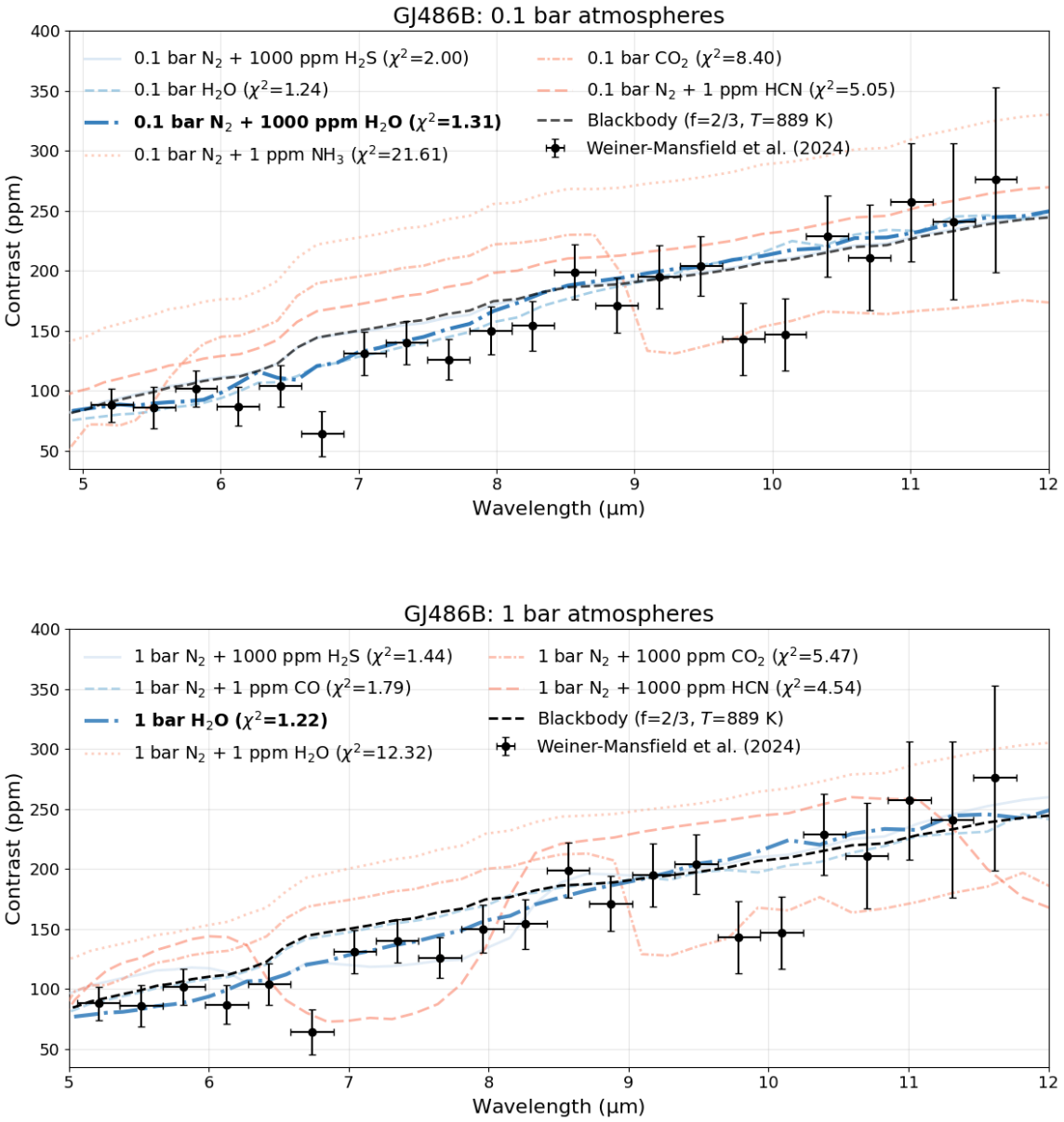

Figure 21: Atmosphere models for GJ 486b for 0.1 and 1 bar surface pressures, with the data by Mansfield et al. [2024]. Each panel shows the three best, and three worst performing models for that pressure. Models in red can be rejected based on the data (Δ ln Z < -3), and models in blue are considered acceptable (Δ ln Z > -3).

Other high-pressure atmosphere do not perform well. For 10 and 100 bar, pure H_2O is the only atmosphere not rejected based on its Bayes factor. Overall, atmospheres with traces of NH_3 fit the data very poorly; and large amounts of CO_2 or SO_2 also make for bad fits. Some interesting, well-performing cases are the 1 bar N_2 + 1 ppm CO atmosphere, fitting the data slightly better than a blackbody; 1 bar N_2 + 1000 ppm H_2S, showing a contrast-dip between 7 and 8.5 micron that is quite consistent with the data; and 0.01 bar N_2 + 1000 ppm HCN, although its goodness-of-fit can also be attributed to its relative transparency, as it largely overlaps with the blackbody model.

Figure 22: Atmosphere models for GJ 486b between 10 and 100 bar surface pressure, with the data by Mansfield et al. [2024]. Each panel shows the three best, and three worst performing models for that pressure. In red, the models are shown that can be rejected based on the data (Δ ln Z < -3), and in blue, the models are considered acceptable (Δ ln Z > -3). In both cases, only the pure H_2O models are not ruled out.

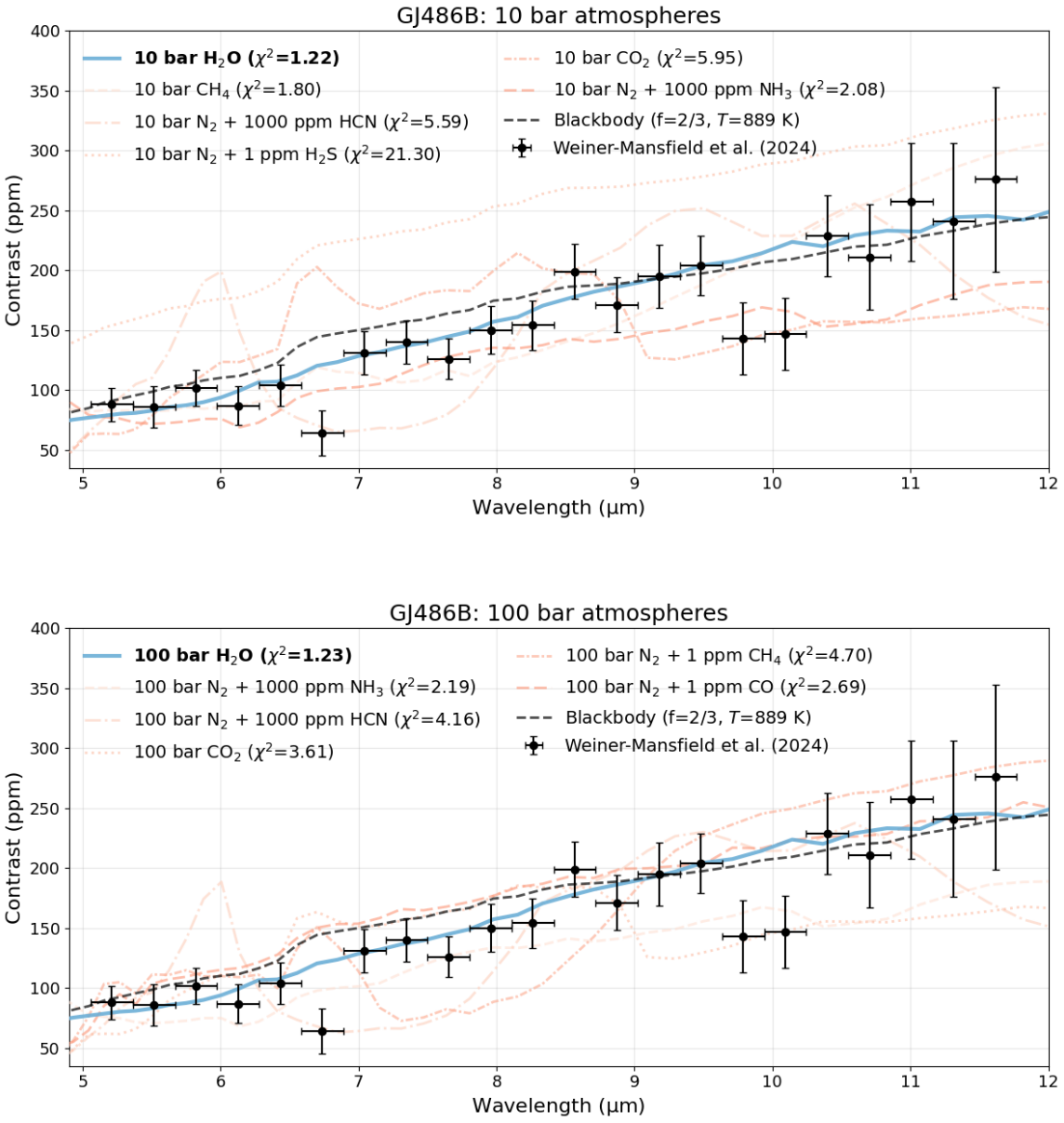

Overall, steam atmospheres provide the best fit to the observational data, significantly outperforming all surface-only models. Pure H_2O atmospheres achieve a maximum Bayes factor of 1.69 at 100 bar surface pressure, while mixed H_2O atmospheres reach a maximum Bayes factor of 2.91. All other atmospheric compositions tested yield poorer fits than the best-performing surface model. A simple blackbody spectrum corresponding to the dayside brightness temperature provides a reasonable baseline fit, although it lacks the spectral features present in the data.

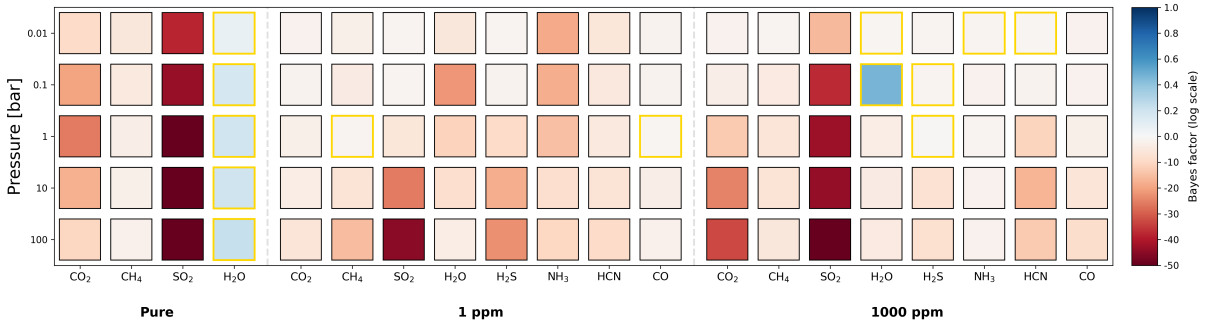

Figure 23: Overview of the Bayesian model comparison for GJ 486b atmospheres. Atmospheres have been ordered according to their gas abundance; pure, and 1 and 1000 ppm mixed with nitrogen. Colours show the Bayes factor with respect to the best surface, hematite. Atmospheres with golden contours are consistent with the data (Δ ln Z > -3).

Notably, none of the physical models explored here successfully reproduce two distinct spectral features observed in the eclipse depth measurements: an absorption feature just below 7 μm and a even broader feature centred around 10 μm. These spectral signatures suggest either additional atmospheric constituents not considered in this analysis, or surface mineralogy effects that require more sophisticated treatment than could be achieved in this thesis.

A complete overview of all atmospheres modelled for GJ 486b is shown in Figure 23. Colours represent Bayes factors with respect to hematite; atmospheres in blue perform better than hematite, and atmospheres in red perform worse. A golden contour shows atmospheres considered consistent with the data. As discussed, SO_2 atmospheres perform worst overall; atmospheres with H_2O, on the other hand, perform best.

4.1.3 Atmospheres: heat redistribution effects

The atmospheric models shown in the previous pages have all been made under the assumption of a dayside-average, zero-heat-redistribution atmosphere. While this is not implausible for atmospheres below 1 bar, heat redistribution effects might become influential in the observations of atmospheres with pressures above 1 bar [Koll, 2022]. I have modelled GJ 486b for five different regimes of heat redistribution (f = $\frac{2}{3}$, $\frac{9}{16}$, $\frac{11}{24}$, $\frac{17}{48}$ and $\frac{1}{4}$), for all pure atmospheres (H_2O, CO_2, CH4, SO2), and for N_2 + 1000 ppm H2O atmospheres. Figure 24 shows the results. Pure SO2-atmospheres have not been included in this figure: all models, regardless of heat redistribution regime, resulted in extremely poor fits.

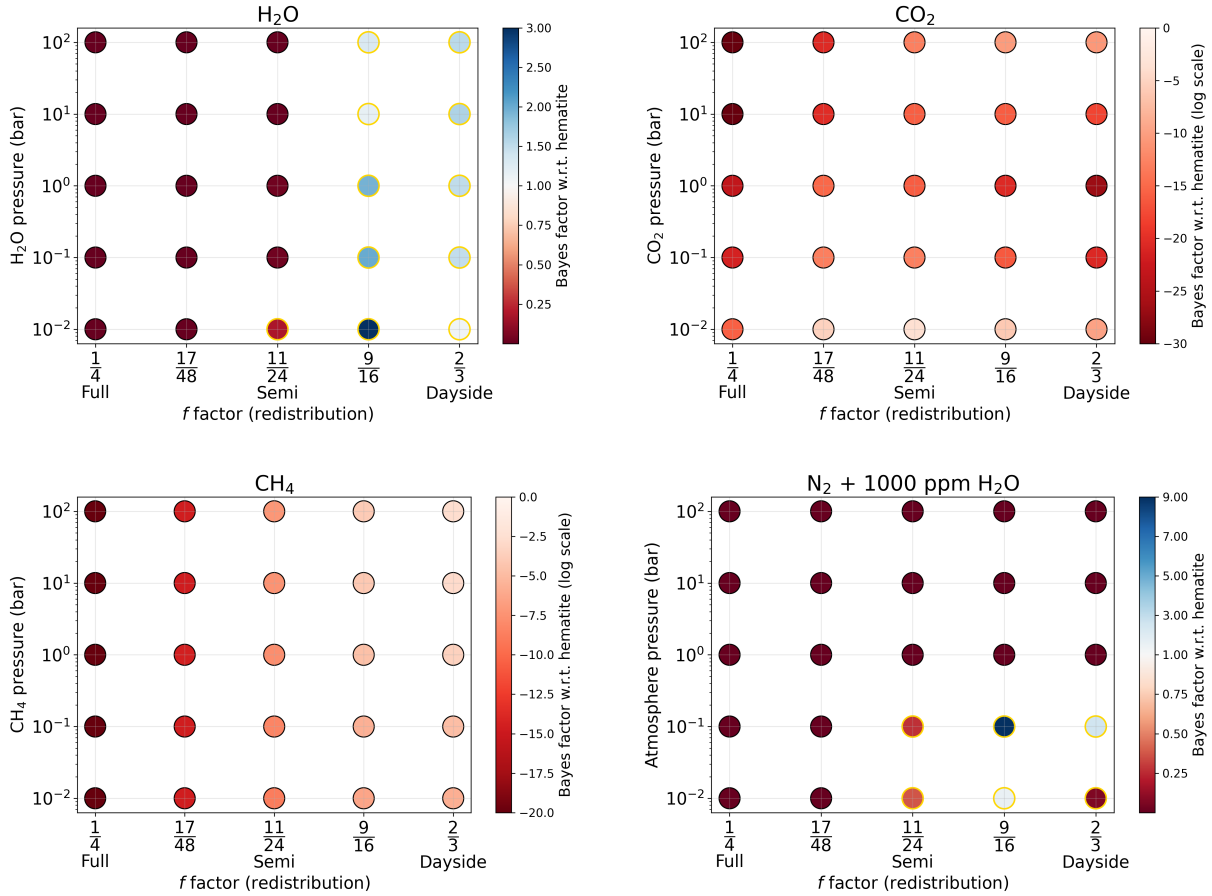

Figure 24: Bayes factors (with respect to hematite) for pure H_2O, CO_2, and CH_4, and N_2 + 1000 ppm H_2O atmospheres at different pressures and heat redistribution (f) factors. The Bayes factors for CO_2 and CH_4 atmospheres have been shown in $\log_{10}$ scale. Atmospheres consistent with the data (Δln Z > -3, Bayes factors above 0.05) are highlighted with a golden ring.

Incorporating heat redistribution effects reveals a tension in the atmospheric modelling results. H_2O-dominated atmospheres perform best under minimal heat transport conditions (f-factor = 2/3 for no redistribution, or 9/16 for 25% efficiency), but their performance degrades substantially as heat redistribution increases. At full heat redistribution, H_2O atmospheres at any surface pressure yield negligible Bayes factors, effectively ruling them out as viable scenarios.

This creates a physical inconsistency: the best-fitting atmospheric models require low heat redistribution efficiencies, yet these same models predict surface pressures and compositions that should drive efficient atmospheric circulation. For instance, a 0.1 bar N_2 + 1000 ppm H_2O atmosphere achieves a strong Bayes factor of $\sim$9 with f = 9/16, while a pure 0.01 bar H_2O atmosphere reaches $\sim$3 in the same redistribution regime. However, both scenarios are physically implausible: atmospheres dense enough to produce significant spectral signatures should also facilitate substantial heat transport to the nightside.

Nevertheless, in the moderate heat redistribution regime ($f = \frac{9}{16}$, corresponding to 25% efficiency), all pure H_2O atmospheric models still outperform the best-fitting surface model.

To assess whether this redistribution efficiency is physically reasonable, I apply the scaling relation from Koll [2022], which relates the f-factor of tidally-locked exoplanets to atmospheric surface pressure, long-wave optical depth $\tau_{\rm LW}$, and equilibrium temperature:

$$f = \frac{2}{3} - \frac{5}{12} \times \frac{\tau_{\rm LW}^{1/3} \left(\frac{p_s}{1\ \rm bar}\right)^{2/3} \left(\frac{T_{\rm eq}}{600\ \rm K}\right)^{-4/3}}{k + \tau_{\rm LW}^{1/3} \left(\frac{p_s}{1\ \rm bar}\right)^{2/3} \left(\frac{T_{\rm eq}}{600\ \rm K}\right)^{-4/3}}, \tag{23}$$

where k encapsulates planetary parameters beyond atmospheric properties and can be approximated as unity for high-molecular-weight atmospheres. For a representative 1-bar H_2O atmosphere around GJ 486b, assuming $\tau_{\rm LW} \approx 1$ and $T_{\rm eq} \approx 700$ K, this scaling predicts $f \approx 0.44$ (closer to $\frac{11}{24}$ than $\frac{9}{16}$). While this estimate involves significant uncertainties, it suggests that substantial H_2O atmospheres should exhibit more efficient heat redistribution than the optimal value found in our spectral fitting. This mismatch underlines the tension between atmospheric models that fit the thermal emission data and those that are physically self-consistent under realistic redistribution assumptions.

4.1.4 An ozone feature at 10 μm?

None of the atmospheres or surfaces shown above explain two features in GJ 486b's eclipse spectrum: one at ~ 6.7 μm, and one at ~ 10 μm. The former is difficult to account for; the latter, however, is wider, and could match ozone's well-known absorption feature at ~ 10 μm. As ozone opacities are available in AGNI, I tried a small set of water-ozone atmospheres (with and without nitrogen) on the data. The full range of pressures (0.01 to 100 bar) was applied. As is clear from Figure 25, these models fit exceptionally well. While a 0.1 bar atmosphere performs best, a 100 bar H_2O + 1000 ppm O_3 atmosphere performs similarly. Table 5 shows the Bayes factors for each atmosphere shown in the figure, with respect to the best fitting surface, hematite. Three of the atmosphere applied have Bayes factors above 20 (Δ ln Z $>$ 3); this means that, would I have used the best performing ozone model as my reference model for Bayesian model comparison, all surface models would have been rejected.

Atmosphere	$\Delta \ln Z$	Bayes factor
0.01 bar N_2 + 30% H_2O + 1000 ppm O_3	2.45	11.59
100 bar N_2 + 30% H_2O + 1000 ppm O_3	2.22	9.23
0.1 bar N_2 + 30% H_2O + 100 ppm O_3	3.37	29.15
1 bar N_2 + 30% H_2O + 100 ppm O_3	3.31	27.43
100 bar H_2O + 1000 ppm O_3	3.24	25.57

Table 5: Bayes factors (with respect to hematite) for water and ozone-rich atmospheres for GJ 486b, with and without nitrogen.

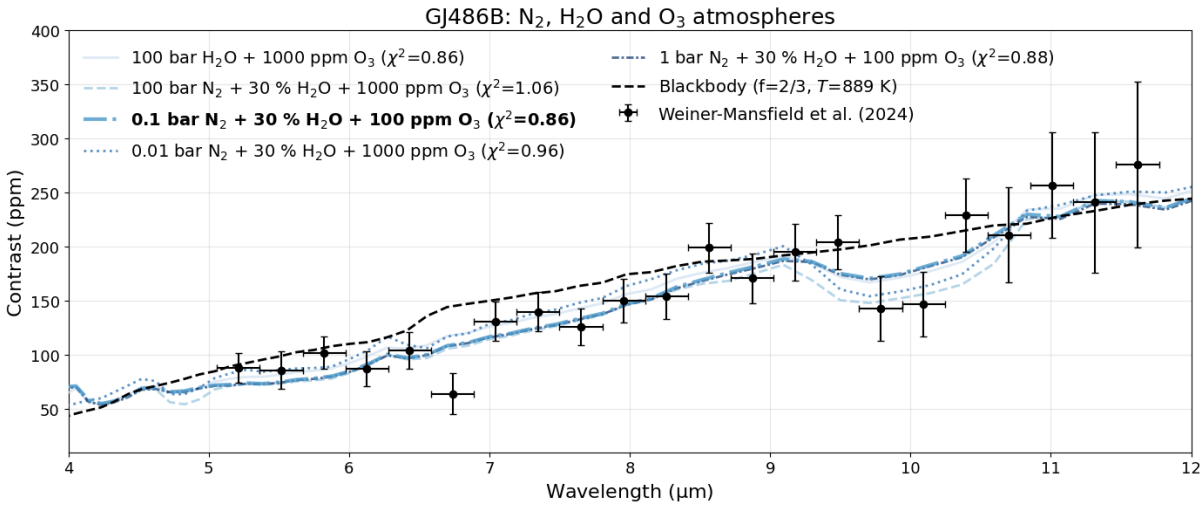

Figure 25: N_2, H_2O and O_3 atmospheres with the data of GJ 486b by Mansfield et al. [2024], together with their chi-squared values.

This raises the question whether abiotic ozone build-up of these amounts is in some way realistic for this planet. Important to note is that potential heat transport has not been accounted for in the models shown above. Nevertheless, it is an interesting result, and will be discussed in more detail in Section 5.4.

4.2 GJ 367b

GJ 367b is a hot, rocky exoplanet with an ultra-short orbital period and an equilibrium temperature of ∼1400 K, making atmospheric retention highly unlikely. In this section, I evaluate a range of atmospheric and surface scenarios to determine which compositions and pressures are consistent with the observed thermal emission by Zhang et al. [2024].

The planet's extreme irradiation and low surface gravity make it an interesting test-case for atmosphere survival under harsh stellar conditions. Additionally, if thick atmospheric models prove capable of fitting the emission data, this might highlight fundamental limitations in using thermal emission spectroscopy alone to distinguish between different atmospheric regimes.

4.2.1 Surface models

Figure 26 shows modelled emission spectra for GJ 367b for the four best, and four worst performing models. The best surface, pyrite, is used as a reference model. Models with a Bayes factor above 0.05 (Δ ln Z > -3) are accepted, and shown in blue; below 0.05, models are rejected, and shown in red. The reduced chi-squared values have been shown as well. Figure 27 displays the relative Bayes factors for all surface compositions tested, while Table 10 in the appendix provides a summary of surface model performances.

We see that, based on the data by Zhang et al. [2024], it is very difficult to distinguish between surface types. Most surfaces produce nearly indistinguishable spectral signatures – only the highest-albedo materials (magnesium sulfate, Martian breccia, albite dust) are definitively ruled out by the data. While pyrite is the preferred model, the distinction is

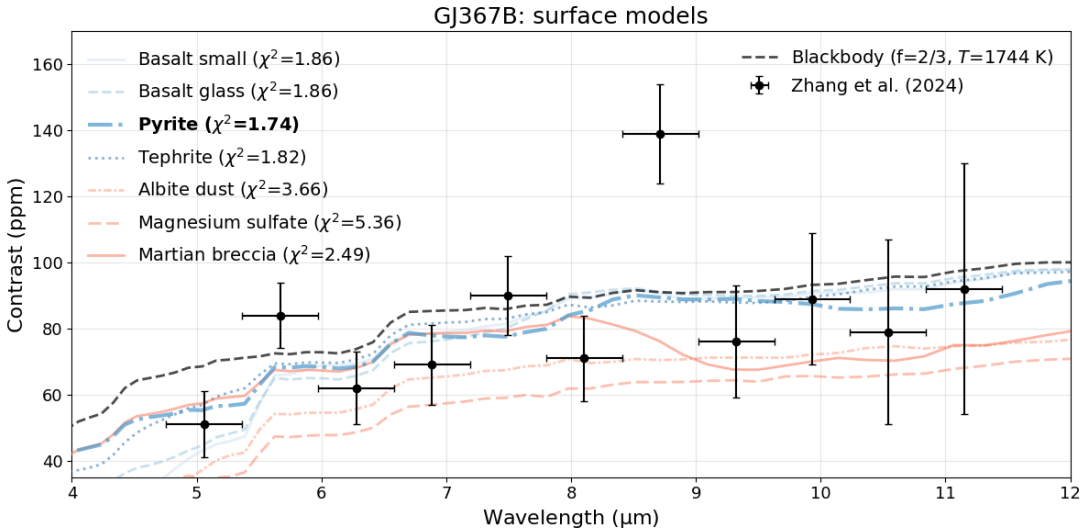

Figure 26: Eclipse depths (here: contrast) in ppm for the four best and four worst performing surface models for GJ 367b, together with their chi-squared values. Models were compared using a Bayesian selection technique. Accepted models (Δ ln Z > -3) are shown in blue, rejected (Δ ln Z < -3) in red. Secondary eclipse depth data by Zhang et al. [2024].

marginal: the five next-best surfaces (tephrite, diorite, basalt glass, small-grain basalt, and norite) have Bayes factors not lower than 0.5, well within the range of model uncertainties.

Figure 28 focuses on four surface models that might be most likely on this planet from a geological perspective [Spaargaren, personal communication], together with the best performing surface model, pyrite. Gabbro and norite represent the most likely scenarios for this planet. Lherzolite and harzburgite (both ultramafic surfaces), while consistent with the data, perform more poorly, although the differences are small. Overall, from an observational and theoretical point of view, a mafic surface such as norite or gabbro seems most likely.

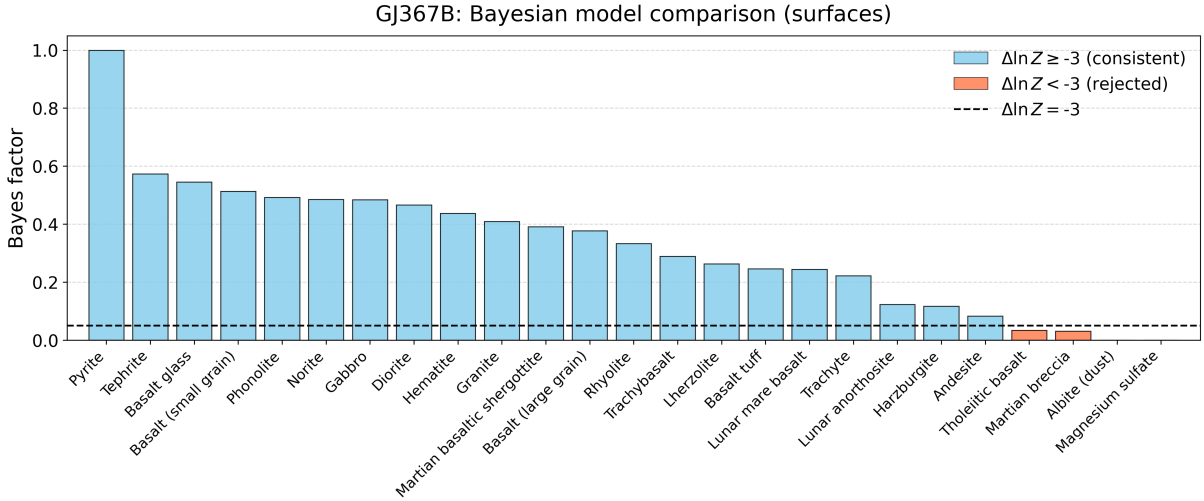

Figure 27: Bayes factors for all surface models applied to the GJ 367b data. Accepted models (Δ ln Z > -3) are shown in blue, rejected (Δ ln Z < -3) in red. Four surfaces that are geologically most likely are made bold.

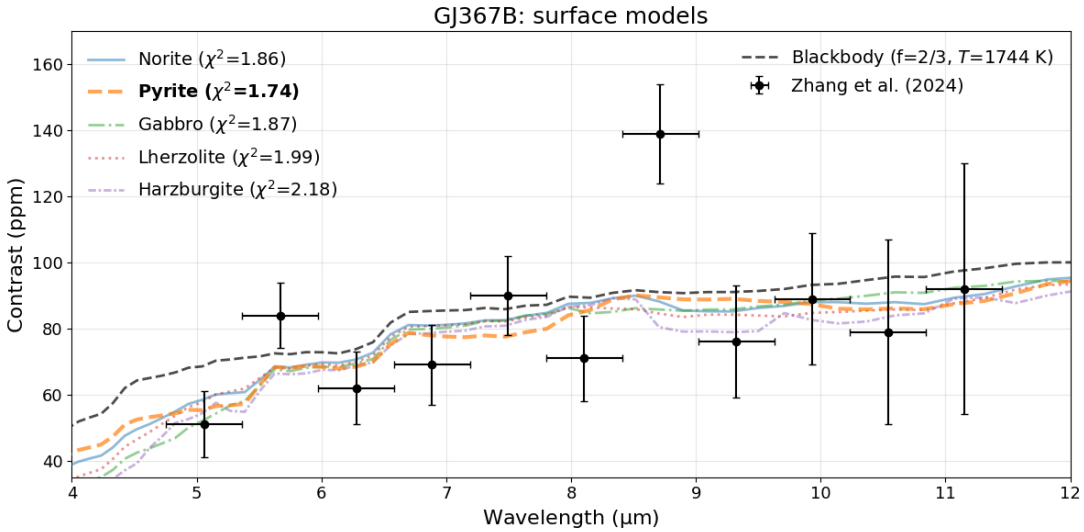

Figure 28: Four consistent surface types that are more likely on GJ 367b from a geological perspective [Spaargaren, personal communication]. Norite and gabbro, the better-performing models, are both mafic surface types. The ultramafic lherzolite and harzburgite are also consistent with the data, but perform less well. Colours are merely used for distinction.

4.2.2 Atmosphere models

Figures 29, 30 and 31 show the atmospheric models for GJ 367b across pressure levels. For this planet, only the elements H_2O, CO_2, CH_4 and SO_2 were modelled; both pure, and as trace elements mixed with N_2. The different panels show the three best, and three worst performing model for each surface pressure (0.01 - 100 bar). Models consistent with the data are shown in blue (Δ ln Z > -3), and models inconsistent with the data (Δ ln Z < -3) are shown in red. The Bayesian comparison was performed with the surface pyrite as a reference model (see Section 4.2). The performance of each model can also be found in Table 11 (pure atmospheres), Table 12 (N_2 atmospheres with 1 ppm trace elements) and Table 13 (N_2 atmospheres with 1000 ppm trace elements) of Appendix A.2.2.

Interestingly, despite our expectations regarding GJ 367b's atmospheres, quite a few atmospheres remain viable based on the data, even up to 100 bar. For pure atmospheres, only H_2O atmospheres are not rejected based on the data. N_2-based atmospheres with traces of CO_2, however, are also viable; and, both 100 bar N_2 + 1 ppm SO_2, and 1 bar N_2 + 1 ppm CH_4 are consistent with the data. The strong performance of the SO_2 model appears linked to the spectral feature around 9 μm visible in Figure 31. Generally, the viable high-pressure atmospheres are characterised by very low trace gas abundances (1 ppm), suggesting that only minimal volatile content is consistent with the observations.

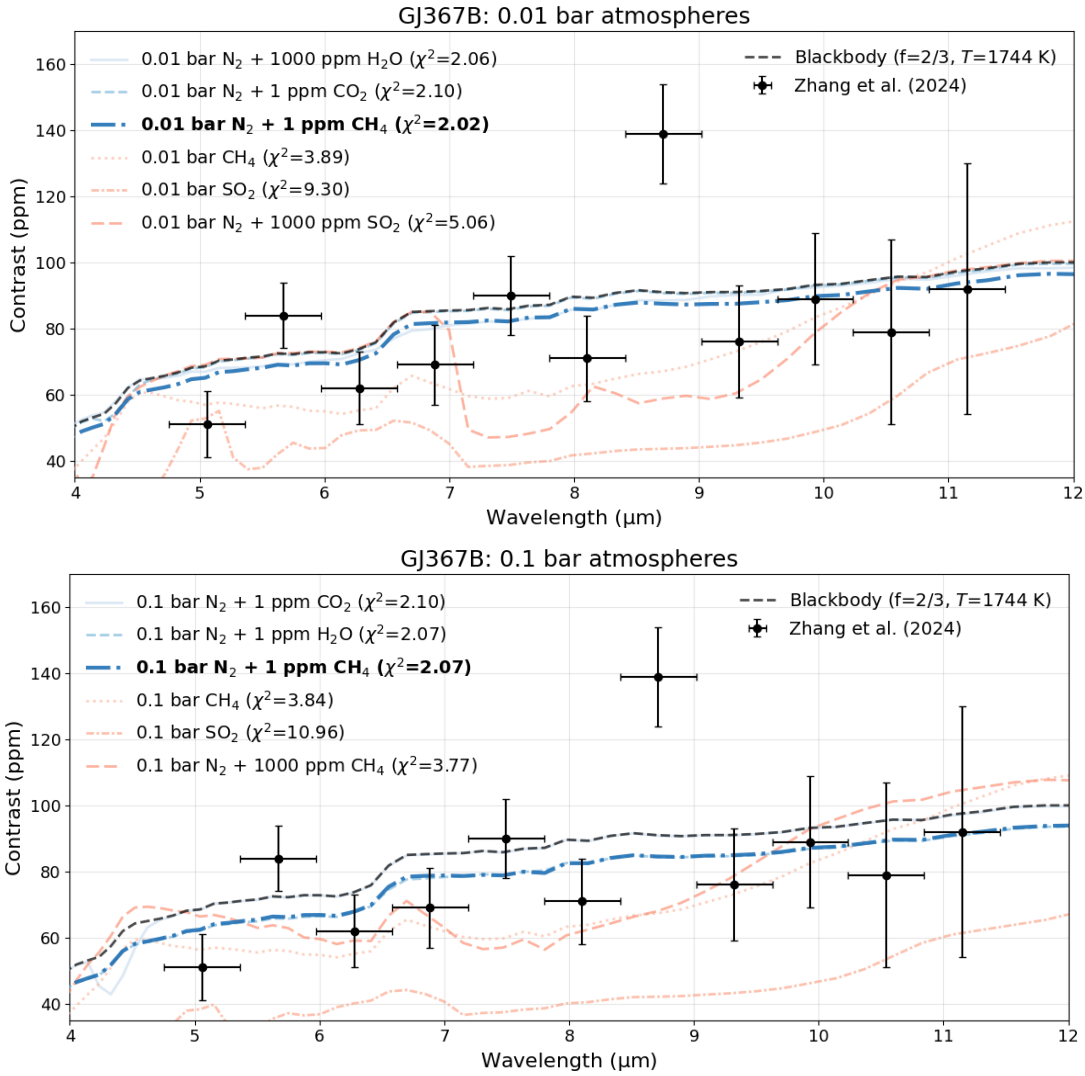

Figure 29: Atmospheric emission models for GJ 367b at 0.01 and 0.1 bar surface pressures. Each panel shows the three best- and three worst-performing atmospheric compositions for the given pressure, compared against the data by Zhang et al. [2024]. Models with Δ ln Z < -3 are shown in red and considered rejected, while those above the threshold (Δ ln Z > -3) are shown in blue and considered consistent with the data.

Despite this range of statistically acceptable models, none successfully reproduce all observed spectral features in GJ 367b's emission spectrum. The scattered nature and low resolution of the data points may limit our ability to effectively choose between models. Importantly, all atmospheric scenarios perform worse than the majority of surface models. Every surface composition above basalt tuff (Bayes factor 0.24) in Table 10 of the appendix provides a better fit to the data than any atmospheric model tested.

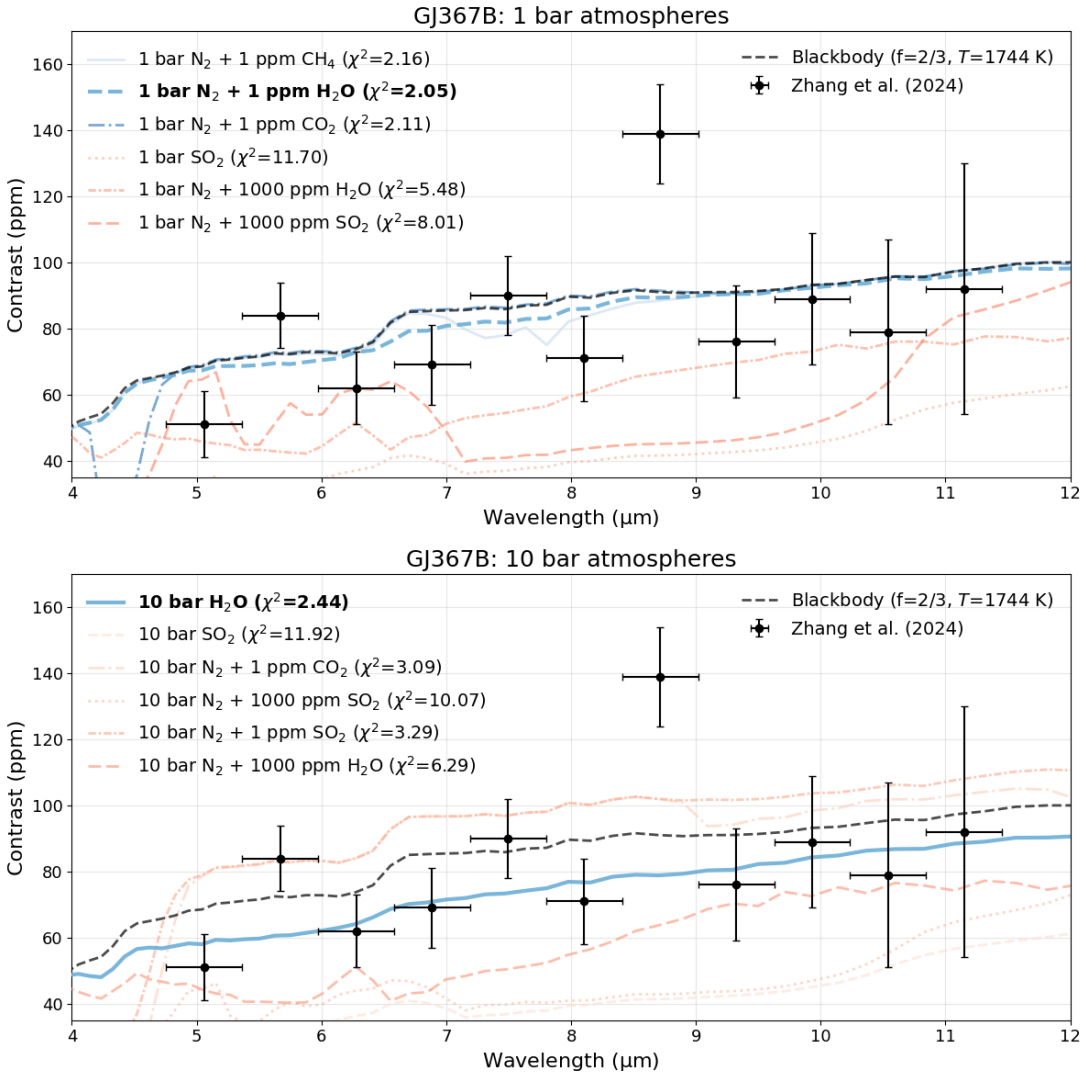

Figure 30: Atmospheric emission models for GJ 367b at 1 and 10 bar surface pressures. Each panel shows the three best- and three worst-performing atmospheric compositions for the given pressure, compared against the data by Zhang et al. [2024]. Models with Δ ln Z < -3 are shown in red and considered rejected, while those above the threshold (Δ ln Z > -3) are shown in blue and considered consistent with the data.

Figure 32 shows a complete overview of all modelled atmospheres for GJ 367b, and their Bayes factors. Models consistent with the data have been shown with golden contours. Overall, high-abundance SO_2 atmospheres perform the worst, and N_2-atmospheres with 1 ppm trace gases fit best. No atmosphere performs better than the reference surface model, pyrite.

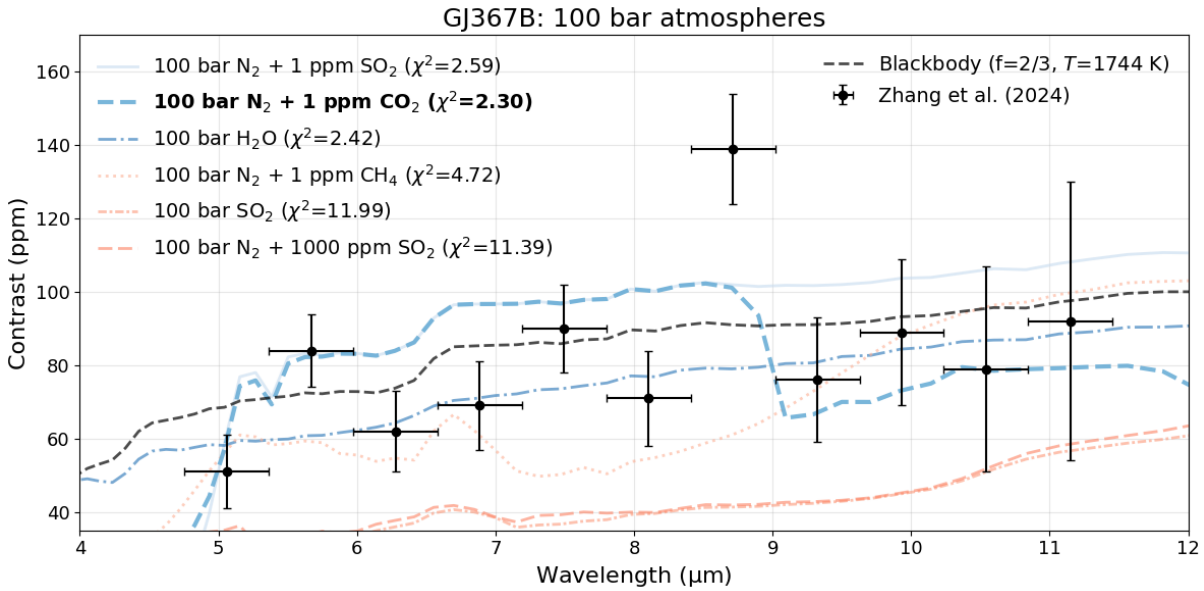

Figure 31: Atmospheric emission models for GJ 367b at 100 bar surface pressures. Each panel shows the three best- and three worst-performing atmospheric compositions for the given pressure, compared against the data by Zhang et al. [2024]. Models with Δ ln Z < -3 are shown in red and considered rejected, while those above the threshold (Δ ln Z > -3) are shown in blue and considered consistent with the data.

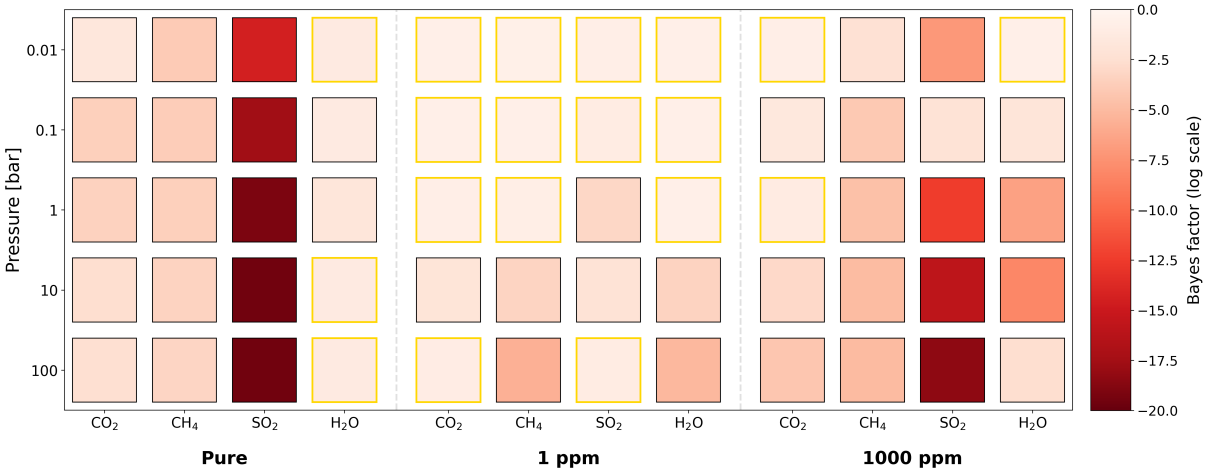

Figure 32: Overview of the Bayesian model comparison for GJ 367b atmospheres. Atmospheres have been ordered according to their gas abundance; pure, and 1 and 1000 ppm mixed with nitrogen. Colours show the Bayes factor with respect to the best surface, pyrite. Atmospheres with golden contours are consistent with the data (Δ ln Z > -3).

4.2.3 Atmospheres: heat redistribution effects

Following the methodology applied to GJ 486b, I examine five heat redistribution regimes ($f = \frac{2}{3}, \frac{9}{16}, \frac{11}{24}, \frac{17}{48}$, and $\frac{1}{4}$) for GJ 367b's atmospheric models. Figure 33 shows my results for pure H_2O, CO_2, and CH_4 atmospheres, alongside N_2 + 1000 ppm CO_2 compositions. The analysis shows a consistent pattern with GJ 486b: increasing surface pressure and heat redistribution both degrade model performance. However, N_2 + 1000 ppm CO_2 atmospheres remain resilient, with a significant fraction staying above the statistical acceptance threshold even under efficient heat transport. Most interestingly, a 1 bar N_2 + 1000 ppm CO_2 atmosphere with 50% heat redistribution efficiency ($f = \frac{11}{24}$) remains consistent with the observations.

This result is significant because, unlike the pure H_2O scenarios for GJ 486b, this CO_2-trace atmosphere achieves a reasonable fit while remaining physically consistent: the heat redistribution efficiency is plausible for a 1 bar atmosphere according to the scaling relation by Koll [2022]. While these models still perform worse than most surface models, nitrogen atmospheres with traces of CO_2 of moderate thickness should not be excluded.

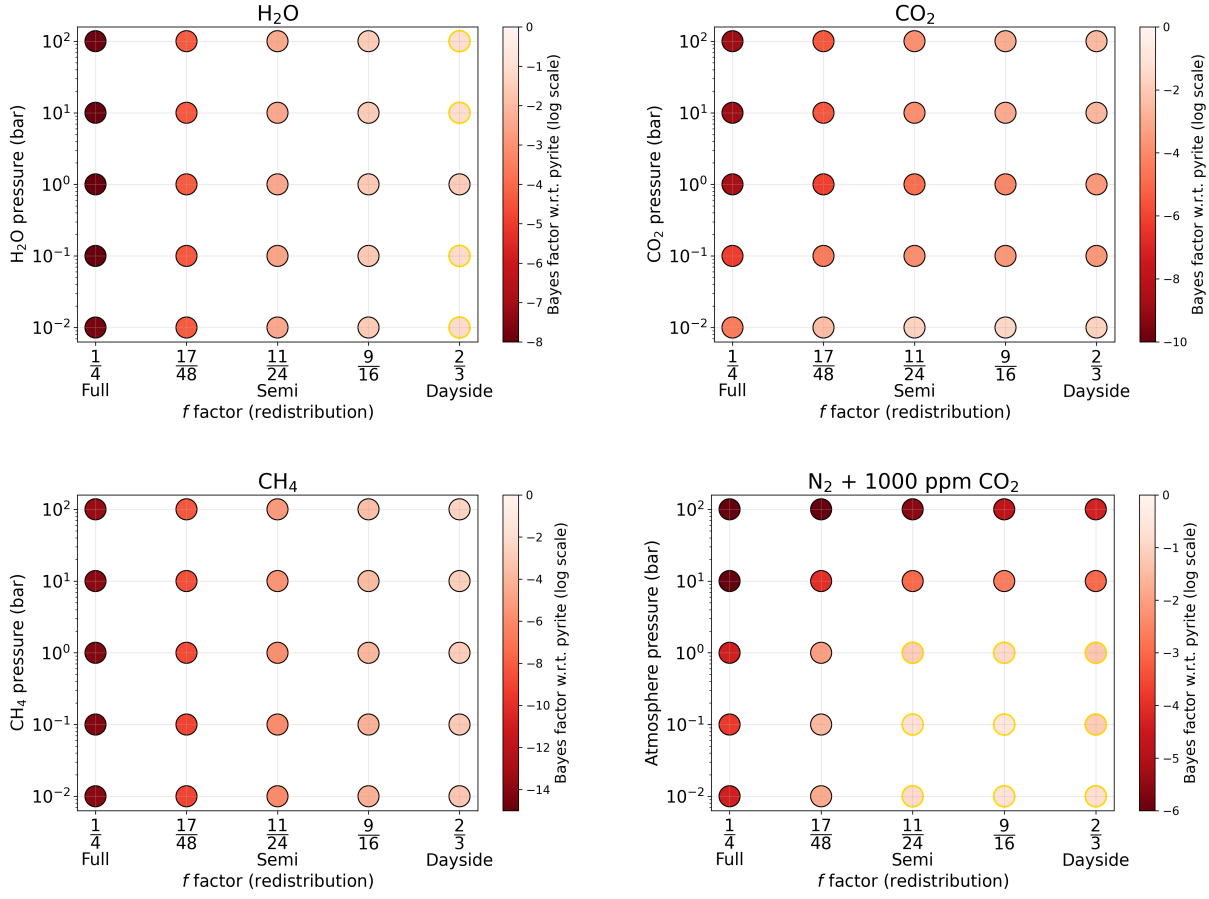

Figure 33: Bayes factors (with respect to pyrite) for pure H_2O, CO_2, and CH_4, and N_2 + 1000 ppm CO_2 atmospheres at different pressures and heat redistribution (f) factors for GJ 367b. All Bayes factors have been shown in $\log_{10}$ scale. Atmospheres consistent with the data (Δln Z > -3, Bayes factors above 0.05) are highlighted with a golden ring.

4.3 TRAPPIST-1b

TRAPPIST-1b is a warm, Earth-sized exoplanet orbiting an ultra-cool M-star of just above 2500 K. With an equilibrium temperature of 400 K, it is significantly cooler than both GJ 367b and GJ 486b. The TRAPPIST-1 system is noteworthy for hosting seven rocky planets, with several located in the temperate zone. Understanding the atmospheric status of TRAPPIST-1b, along with its neighbour TRAPPIST-1c, carries broader implications for the habitability of the other TRAPPIST-1 planets.

Unlike GJ 367b and GJ 486b, which have been studied using low-resolution spectroscopy, TRAPPIST-1b has been observed through MIRI's F1280W and F1500W broadband filters. In the following sections, we will compare a range of surface compositions and atmospheric models to TRAPPIST-1b's measured eclipse depths reported by Ducrot et al. [2025].

4.3.1 Surface models

Figure 34 shows modelled emission spectra for TRAPPIST-1b for the four best, and four worst performing models. The best surface, Martian breccia, is used as a reference model. Models with a Bayes factor below 0.05 are rejected, and shown in red. In the case of TRAPPIST-1b, certain models are shown in yellow: these surfaces are not rejected based on the data, but perform significantly worse than the best surface types, with Bayes factors below 0.3 (-1.2 $>$ Δ ln Z $>$ -3). Models with Bayes factors above 0.3 (Δ ln Z $>$ -1.2) are shown in blue. The reduced chi-squared values are also included. Figure 35 displays the relative Bayes factors for all surface compositions tested, while Table 14 in Appendix A.3.1 provides a summary of surface model performances.

Due to the limited amount of data by Ducrot et al. [2025], the Bayesian selection model has difficulty distinguishing between surface types. Surfaces with low albedos are not preferred, but also not rejected; only the highest-albedo materials (magnesium sulfate, albite dust) are ruled out. Mafic surfaces (basalt, gabbro) and ultramafic surfaces (lherzolite) do well. Martian breccia, the best performing surface, contains fragments of different Martian surface types, making its classification into (ultra)mafic, intermediate of felsic more difficult. Nevertheless, as most of Mars' surface is mafic, it is likely largely composed of mafic materials [Meslin et al., 2013].

It should be remarked that even the best fitting surface does not match both data points nicely, only meeting their error bars. If there is no better fitting atmosphere, this might be a sign of the planet having a different type of surface than considered here; or one of more complexity.

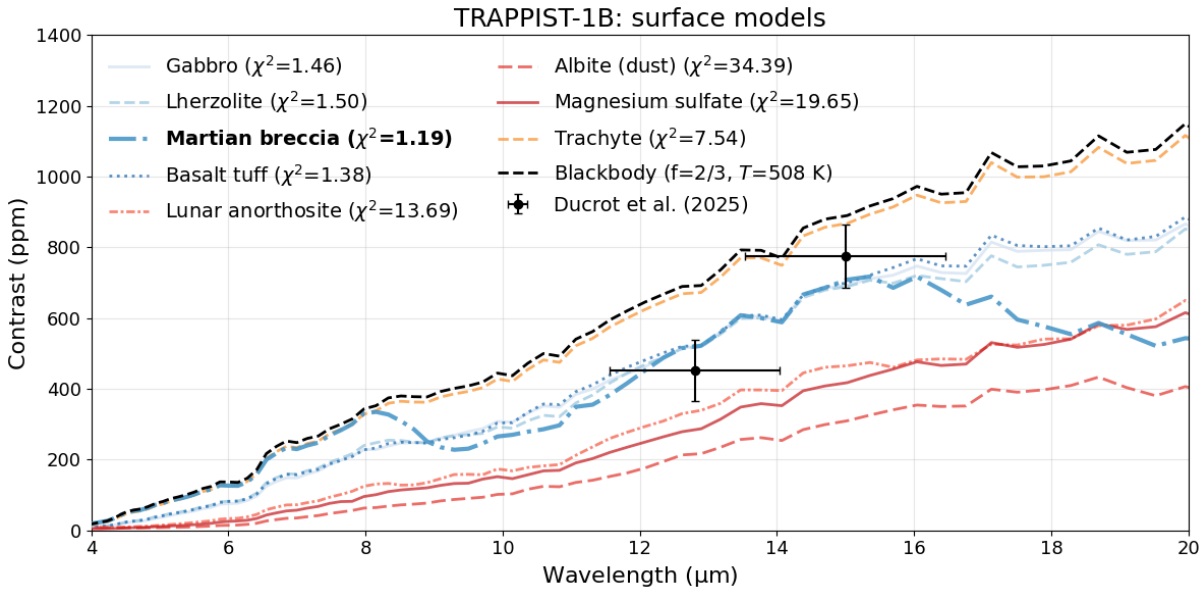

Figure 34: Eclipse depths in ppm for the four best and four worst performing surface models for TRAPPIST-1b, together with their chi-squared values. The best performing model has been made bold. Models were compared using a Bayesian selection technique. The best accepted models (Δ ln Z > -1.2) are shown in blue, accepted models with Bayes factors below 0.3 (-1.2 > Δ ln Z > -3) are shown in yellow, and rejected models (Δ ln Z < -3) in red. The data are secondary eclipse measurements in MIRI's F1500W and F1280W filters, by Ducrot et al. [2025].

Figure 35 shows an overview of the surfaces modelled for TRAPPIST-1b. Many surfaces are practically indistinguishable; only three surfaces can be rejected based on its Bayes factor with respect to Martian breccia.

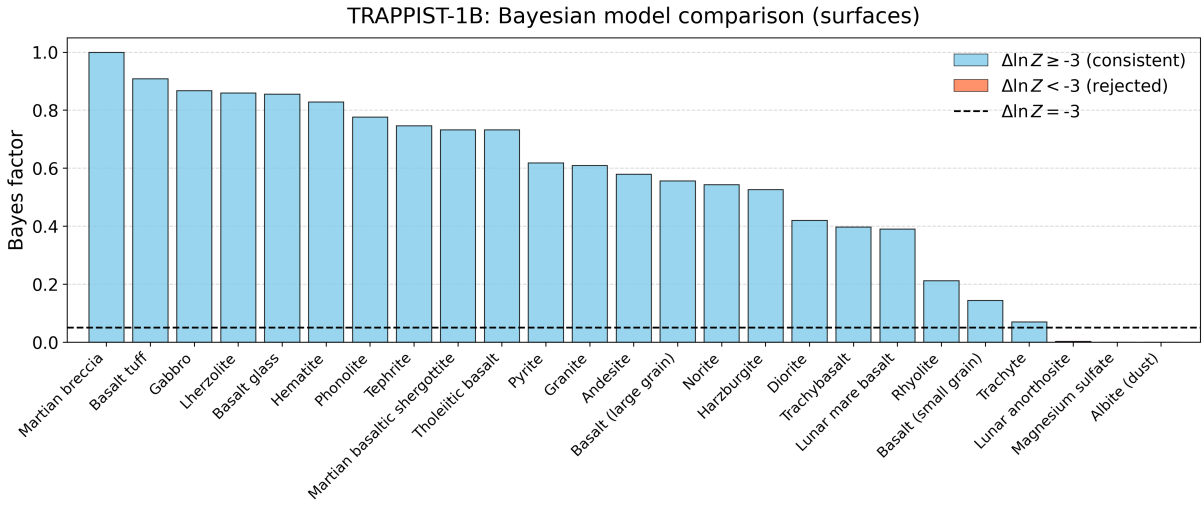

Figure 35: Overview of Bayes factors for all surface models applied to the TRAPPIST-1b data, with respect to Martian breccia. Accepted models (Δ ln Z > -3) are shown in blue, rejected (Δ ln Z < -3) in red.

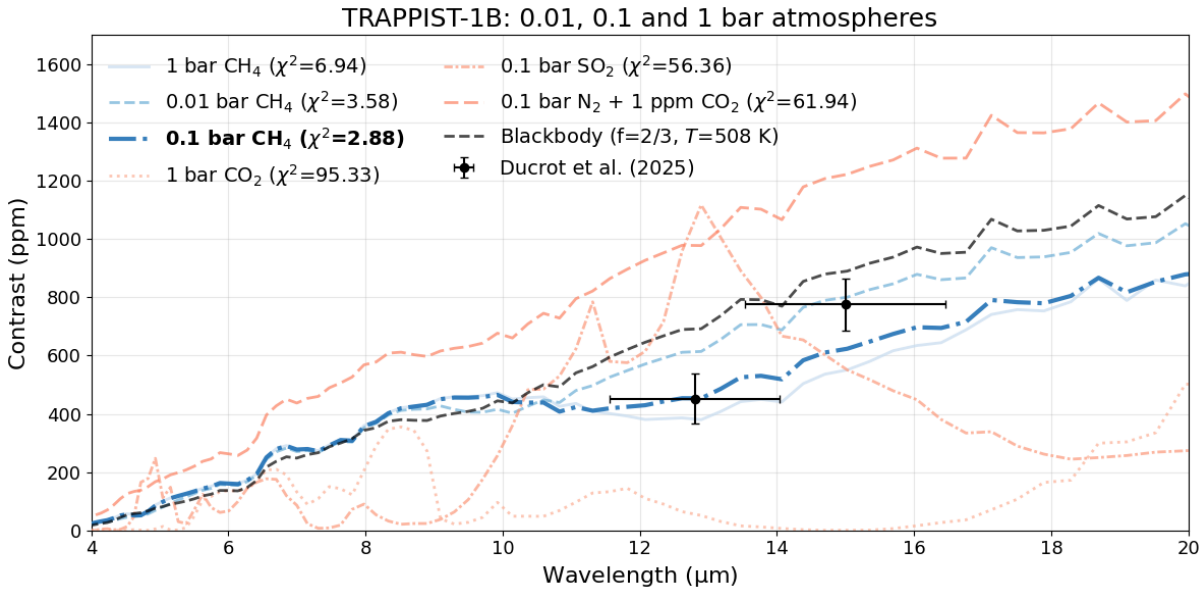

Figure 36: Atmosphere models for TRAPPIST-1b between 0.01 and 1 bar surface pressure, together with the data by Ducrot et al. [2025]. Each panel shows the three best, and three worst performing models for the pressures mentioned. In red, the models are shown that can be rejected based on the data (Δ ln Z < -3.0), and in blue, the models are considered acceptable (Δ ln Z > -3.0). Models with Δ ln Z < -50 were excluded from the plots, to allow for a better visual overview.

4.3.2 Atmosphere models

Figures 36 and 37 show the atmospheric models for TRAPPIST-1b across pressure levels, categorised into thin (0.01 - 1 bar) and thick (10 - 100 bar) atmospheres. The elements H_2O, CO_2, CH_4 and SO_2 were modelled; both pure, and as trace elements mixed with N_2. Models consistent with the data are shown in blue (Δ ln Z > -3), and models inconsistent with the data (Δ ln Z < -3) are shown in red. The Bayesian comparison was performed with the surface Martian breccia as a reference model (see Section 4.3.1). The performance of each model can also be found in Table 15 (pure atmospheres), Table 16 (N_2 atmospheres with 1000 ppm trace elements) and Table 17 (N_2 atmospheres with 1 ppm trace elements) of Appendix A.3.2.

Only a narrow range of compositions provide adequate fits to the observational data. Most atmospheric scenarios, particularly nitrogen-dominated atmospheres containing trace amounts (1 ppm) of secondary species, fit very poorly.

Interestingly, methane-rich atmospheres are viable candidates. Pure CH_4 atmospheres remain consistent with the data for surface pressures up to 1 bar, while nitrogen atmospheres containing 1000 ppm CH_4 provide good fits at a surface pressure of 100 bar. Beyond these scenarios, the only other atmospheres that are not rejected are thick nitrogen atmospheres (10 and 100 bar) containing 1000 ppm H_2O, though both yield Bayes factors below 0.1, indicating marginal support.

Figure 38 shows a complete overview of all modelled atmospheres for TRAPPIST-1b, and their Bayes factors. Bayes factors have been cut off until 10^{-20}, to allow for distinction between better performing models. Models consistent with the data have been shown with golden

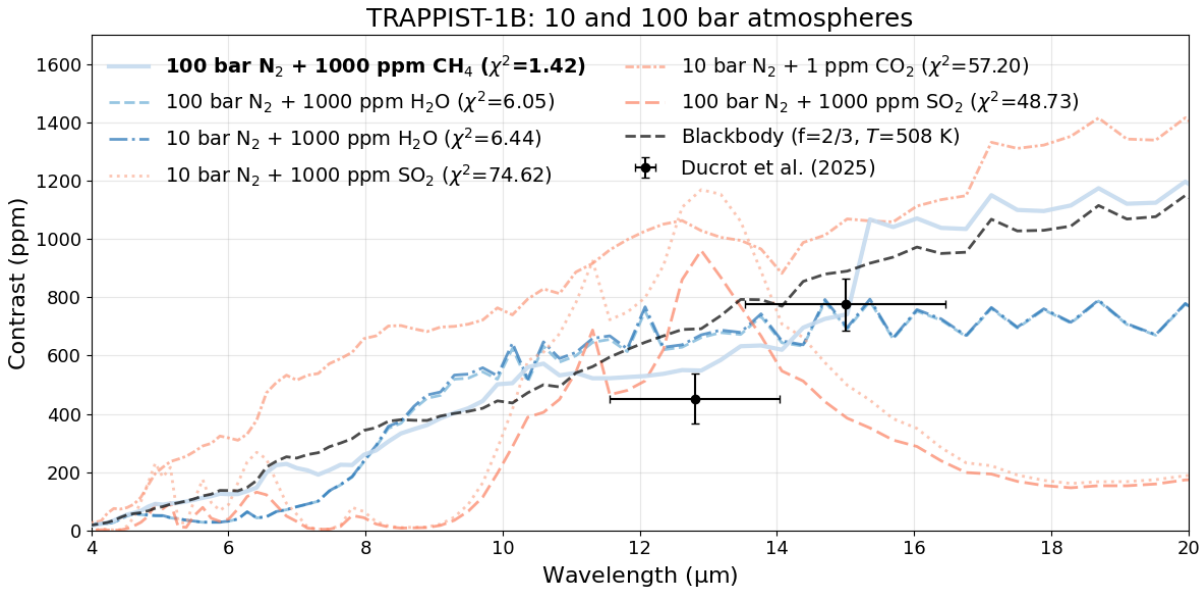

Figure 37: Atmosphere models for TRAPPIST-1b between 10 and 100 bar surface pressure, together with the data by Ducrot et al. [2025]. Each panel shows the three best, and three worst performing models for the pressures mentioned. In red, the models are shown that can be rejected based on the data (Δ ln Z < -3.0), and in blue, the models are considered acceptable (Δ ln Z > -3.0). Models with Δ ln Z < -50 were excluded from the plots, to allow for a better visual overview.

contours. As mentioned, few atmospheres do well. N_2-atmospheres with 1 ppm trace gases fit worst; and a small set of CH_4 atmospheres fit best. No atmosphere performs better than the reference surface model, Martian breccia.

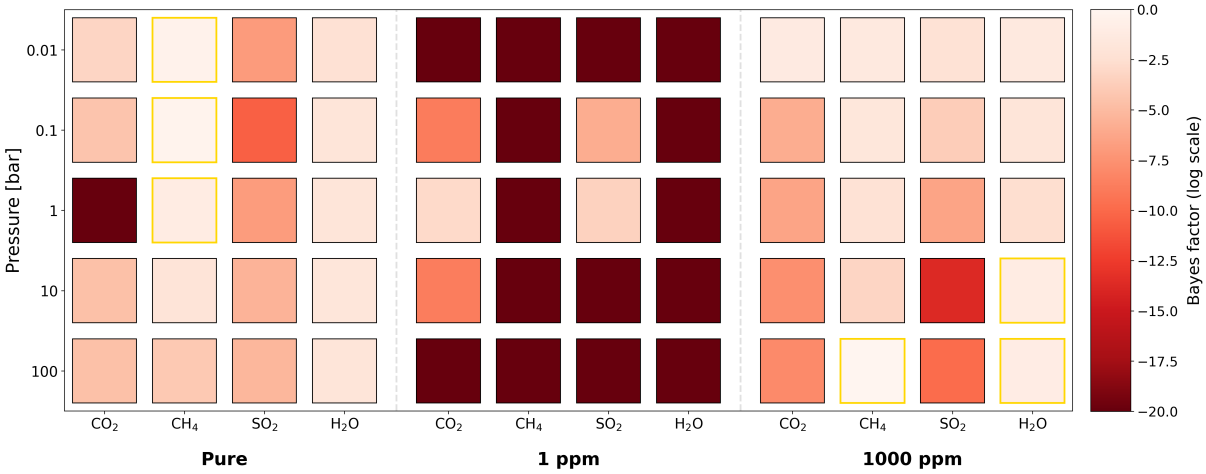

Figure 38: Overview of the Bayesian model comparison for TRAPPIST-1b atmospheres. Atmospheres have been ordered according to their gas abundance; pure, and 1 and 1000 ppm mixed with nitrogen. Colours show the Bayes factor with respect to the best surface, Martian breccia. Atmospheres with golden contours are consistent with the data (Δ ln Z > -3).

4.3.3 Atmospheres: heat redistribution effects

Again for TRAPPIST-1b, I model five heat redistribution regimes ($f = \frac{2}{3}, \frac{9}{16}, \frac{11}{24}, \frac{17}{48}$, and $\frac{1}{4}$) for all atmospheric models. Figure 39 shows the results for pure H_2O, CO_2, and CH_4 atmospheres, together with N_2 + 1000 ppm CH_4 compositions.

CO_2 atmospheres are in no case consistent with the data, and CH_4 atmospheres decrease in goodness of fit with increasing pressure and heat transport. Taking heat transport into account, only the pure and thin CH_4 atmospheres, up to 0.1 bar, stay plausible. Instead, the performance of N_2 + 1000 CH_4 atmospheres seems to improve with heat transport: even a 10 bar atmosphere with 75% redistribution efficiency ($\varepsilon = 0.75, f = 17/48$) is consistent with the data.

There is a similar trend for pure H_2O atmospheres: while none of these fit without heat transport included, pure water atmospheres up to 100 bar with 75% redistribution efficiency cannot be rejected. Nevertheless, thin (up to 1 bar) N_2 + 1000 CH_4 atmospheres with moderate ($\varepsilon = 0.50, f = 11/24$) perform best. A 100 bar N_2 + 1000 CH_4 atmosphere does not stay consistent with the data in high heat transport regimes.

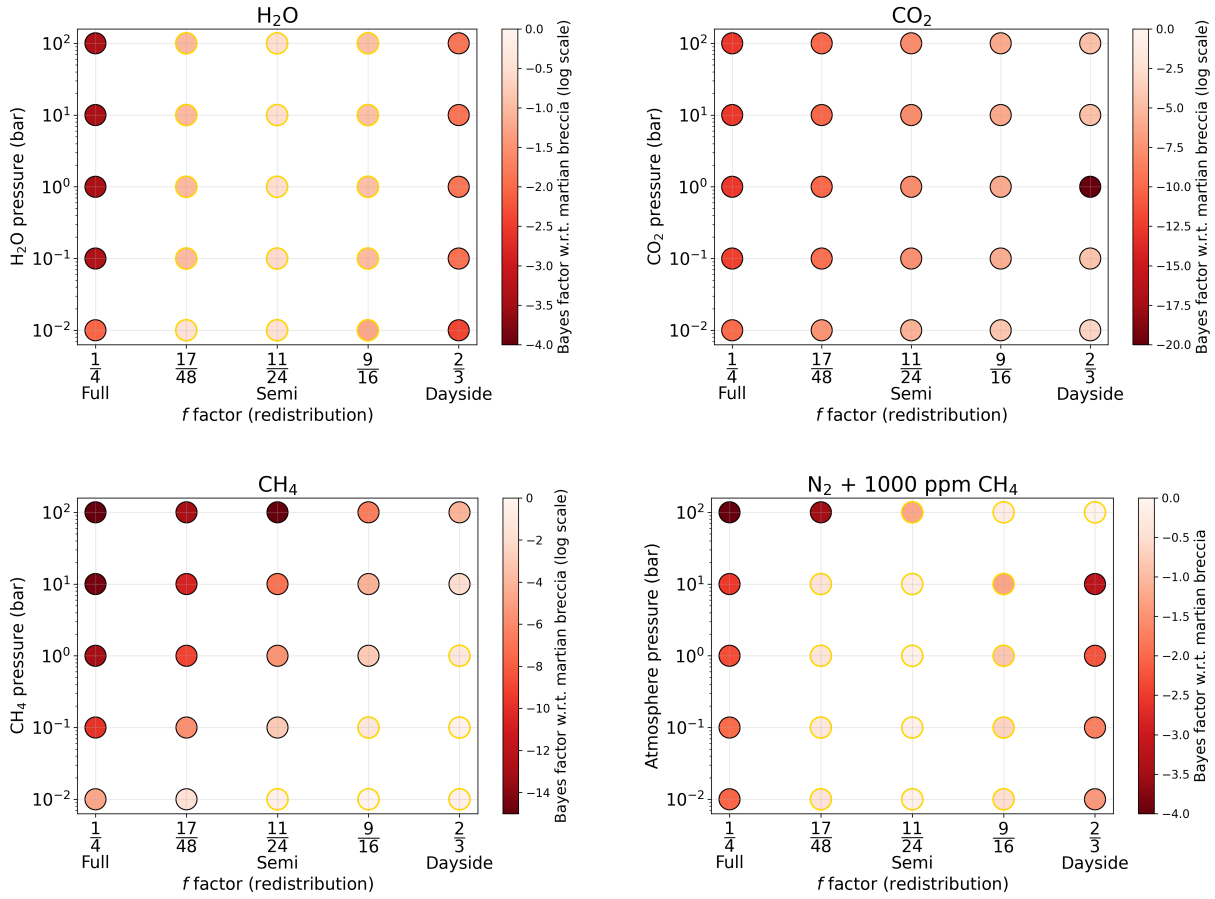

Figure 39: Bayes factors (with respect to pyrite) for pure H_2O, CO_2, and CH_4, and N_2 + 1000 ppm CH_4 atmospheres at different pressures and heat redistribution (f) factors for TRAPPIST-1b. All Bayes factors have been shown in $\log_{10}$ scale.

4.4 TRAPPIST-1c

With an equilibrium temperature just below 350 K, TRAPPIST-1c is the coldest exoplanet modelled in this thesis. It has a similar size TRAPPIST-1b, and is slightly more massive than the Earth. TRAPPIST-1c has, so far, only been observed through MIRI's F1500W broadband filter. In the following sections, we will compare a range of surface compositions and atmospheric models to this eclipse depth, as reported by Zieba et al. [2023].

4.4.1 Surface models

Figure 40 shows modelled emission spectra for TRAPPIST-1c for the three best, and three worst performing models. As the differences in performance between surfaces is small, only six have been shown. The best surface, granite, is used as a reference model. Models with a Bayes factor below 0.05 are rejected, and shown in red. In the case of TRAPPIST-1c, two models are shown in yellow: these surfaces are not rejected based on the data, but perform worse than the best surface types, with Bayes factors below 0.3 (-1.2 > Δ ln Z > -3). Models with Bayes factors above 0.3 (Δ ln Z > -1.2) are shown in blue. As there is only one data point, no chi-squared has been included. Figure 41 displays the relative Bayes factors for all surface compositions tested, while Table 18 in Appendix A.4.1 provides a summary of surface model performances.

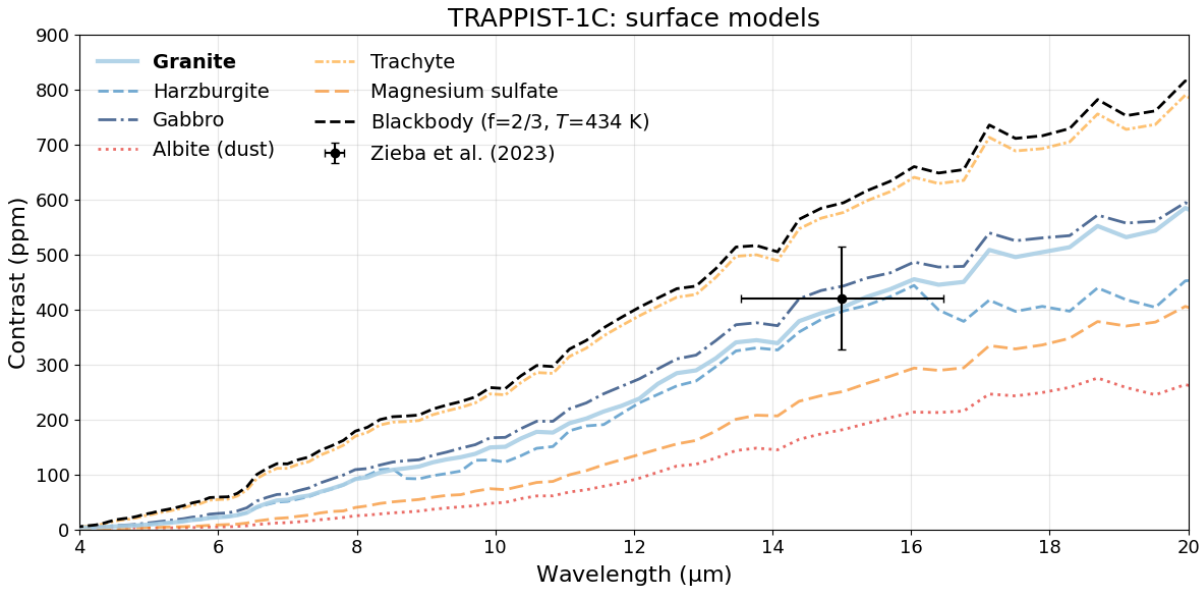

Figure 40: Eclipse depths in ppm for the three best and three worst performing surface models for TRAPPIST-1c, together with their chi-squared values. The best performing model has been made bold. Models were compared using a Bayesian selection technique. The best accepted models (Δ ln Z > -1.2) are shown in blue, accepted models with Bayes factors below 0.3 (-1.2 > Δ ln Z > -3) are shown in yellow, and rejected models (Δ ln Z < -3) in red. The data point is a secondary eclipse measurement in MIRI's F1500W filter by Zieba et al. [2023].

Having only one data point, any surface model yielding nearly the correct eclipse depth at 15 μm fits well. Therefore, Bayesian selection is difficult. Albite dust is the only surface type definitely excluded by the data. Other high-albedo surfaces are also not preferred, as well as low-albedo surfaces, such as trachyte or pyrite. The ultramafic harzburgite and lherzolite fit well, as well as and the mafic gabbro and basalt. The surface that fits best (by a very small margin) is granite, a felsic, plutonic rock very common on Earth. Exact surface characterisation is nearly impossible based on the single data point.

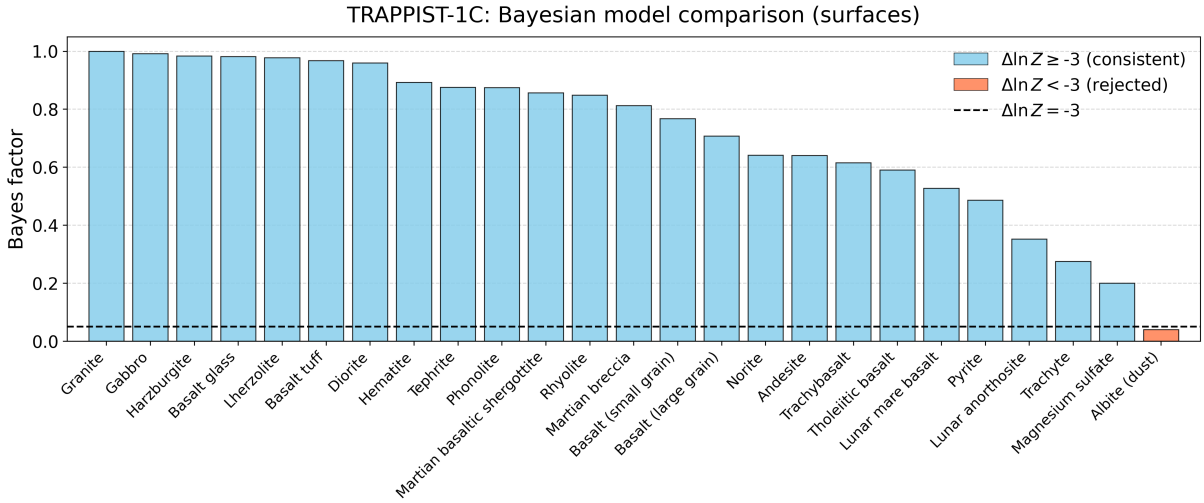

Figure 41: Overview of Bayes factors for all surface models applied to the TRAPPIST-1c data, with respect to granite. Accepted models (Δ ln Z > -3) are shown in blue, rejected (Δ ln Z < -3) in red.

4.4.2 Atmosphere models

Figures 42 and 43 show the atmospheric models for TRAPPIST-1c across pressure levels, categorised into thin (0.01 - 1 bar) and thick (10 - 100 bar) atmospheres. The elements H_2O, CO_2, CH_4 and SO_2 were modelled; both pure, and as trace elements mixed with N_2. Models consistent with the data are shown in blue (Δ ln Z > -3), and models inconsistent with the data (Δ ln Z < -3) are shown in red. The Bayesian comparison was performed with the surface granite as a reference model (see Section 4.4.1). The performance of each model can also be found in Table 19 (pure atmospheres), Table 20 (N_2 atmospheres with 1000 ppm trace elements) and Table 21 (N_2 atmospheres with 1 ppm trace elements) of Appendix A.4.2.

With a single data point, many atmospheric scenarios provide adequate fits to the data. With a single exception, all pure atmospheres are considered consistent, with low-pressure CH_4 and SO_2 performing best. Nevertheless, most nitrogen-dominated atmospheres containing trace amounts (1 ppm) of secondary species fit poorly. 1 bar N_2 + 1 ppm CO_2 is an exception: the CO_2 absorption feature around 15 μm exactly matches the F1500W emission found by Zieba et al. [2023].

High-pressure atmospheres can not be excluded based on the data. Specifically, a 100 bar N_2 + 1000 ppm CH_4 atmosphere matches the data point exactly. 100 bar N_2 + 1000 ppm H_2O also performs well, although the match is less striking. Similarly, over half of the 10 bar

atmospheres cannot be ruled out, with 10 bar N_2 + 1000 ppm H_2O and SO_2 both yielding good fits.

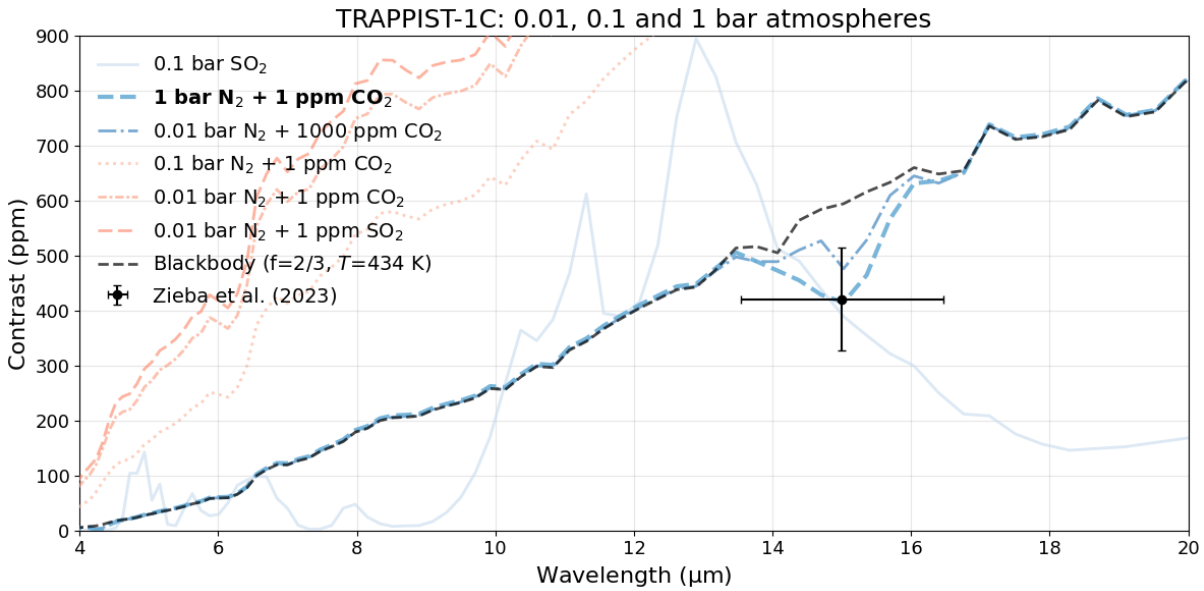

Figure 42: Atmosphere models for TRAPPIST-1c between 0.001 and 1 bar surface pressure. Each panel shows the three best, and three worst performing models for the pressures mentioned. In red, the models are shown that can be rejected based on the data (Δ ln Z < -3.0), and in blue, the models are considered acceptable (Δ ln Z > -3.0). Models with Δ ln Z < -50 were excluded from the plots, to allow for a better visual overview. The data point is a secondary eclipse measurement in MIRI's F1500W filter by Zieba et al. [2023].

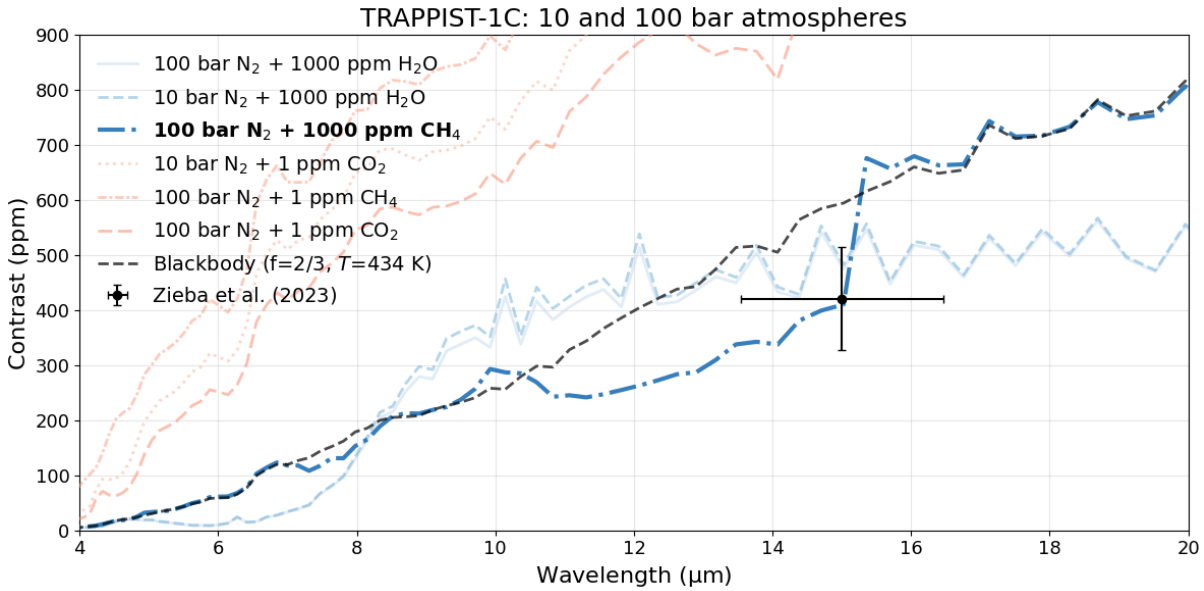

Figure 43: Atmosphere models for TRAPPIST-1c between 10 and 100 bar surface pressure. Again, models with Δ ln Z < -50 were excluded from the plots, to allow for a better visual overview. The data point is a secondary eclipse measurement in MIRI's F1500W filter by Zieba et al. [2023].

Figure 44 shows a complete overview of all modelled atmospheres for TRAPPIST-1c, and their Bayes factors. Bayes factors have been cut off until 10^{-10}, to allow for visual distinction between better performing models. Models consistent with the data have been shown with golden contours. As mentioned, most atmospheres are consistent with the data; more data points are necessary for this planet to constrain its atmosphere status.

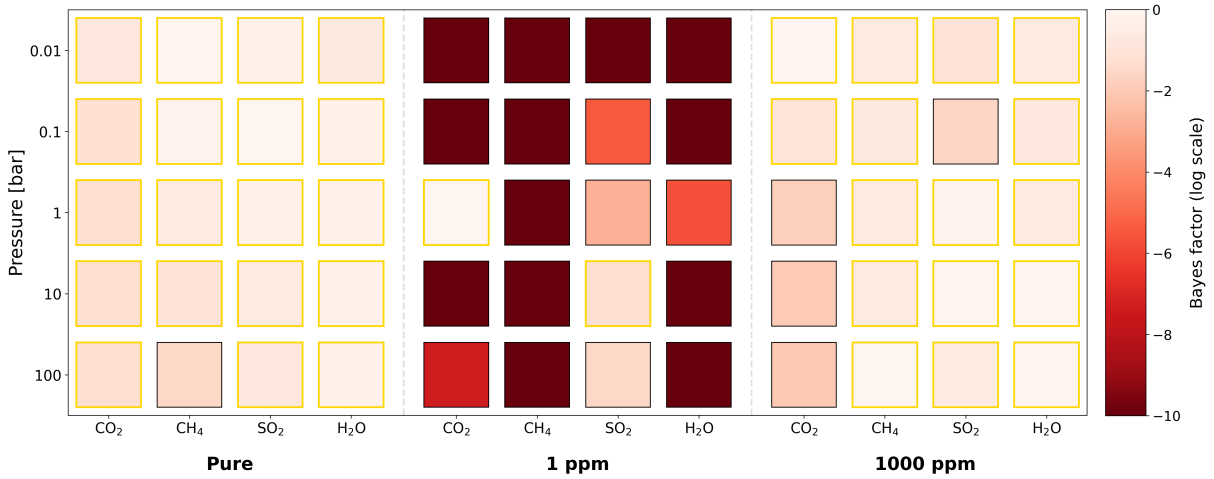

Figure 44: Overview of the Bayesian model comparison for TRAPPIST-1c atmospheres. Atmospheres have been ordered according to their gas abundance; pure, and 1 and 1000 ppm mixed with nitrogen. Colours show the Bayes factor with respect to the best surface, granite. Atmospheres with golden contours are consistent with the data (Δ ln Z > -3). Bayes factors have been cut off below 10^{-10} to allow for a better distinction by eye.

4.4.3 Atmospheres: heat redistribution

For TRAPPIST-1c, the same five heat redistribution regimes were modelled ($f = \frac{2}{3}, \frac{9}{16}, \frac{11}{24}, \frac{17}{48}$, and $\frac{1}{4}$) for all atmospheric models. Figure 45 shows results for pure H_2O, CO_2, and CH_4 atmospheres, plus N_2 + 1000 ppm CH_4 compositions. The pattern mirrors the no-transport case: many atmospheres remain viable with one data point. Heat transport degrades CO_2 and CH_4 performance, while N_2 + 1000 ppm CH_4 and pure H_2O improve, peaking at 50% efficiency ($\varepsilon = 0.50, f = 11/24$). A 10 bar N_2 + 1000 ppm CH_4 atmosphere with 75% heat redistribution fits well.

TRAPPIST-1c is the only planet supporting a 100 bar atmosphere with full heat redistribution: 100 bar pure H_2O has a Bayes factor of ∼0.2 versus granite. However, the evidence favours thinner atmospheres (1-10 bar) with moderate heat transport.

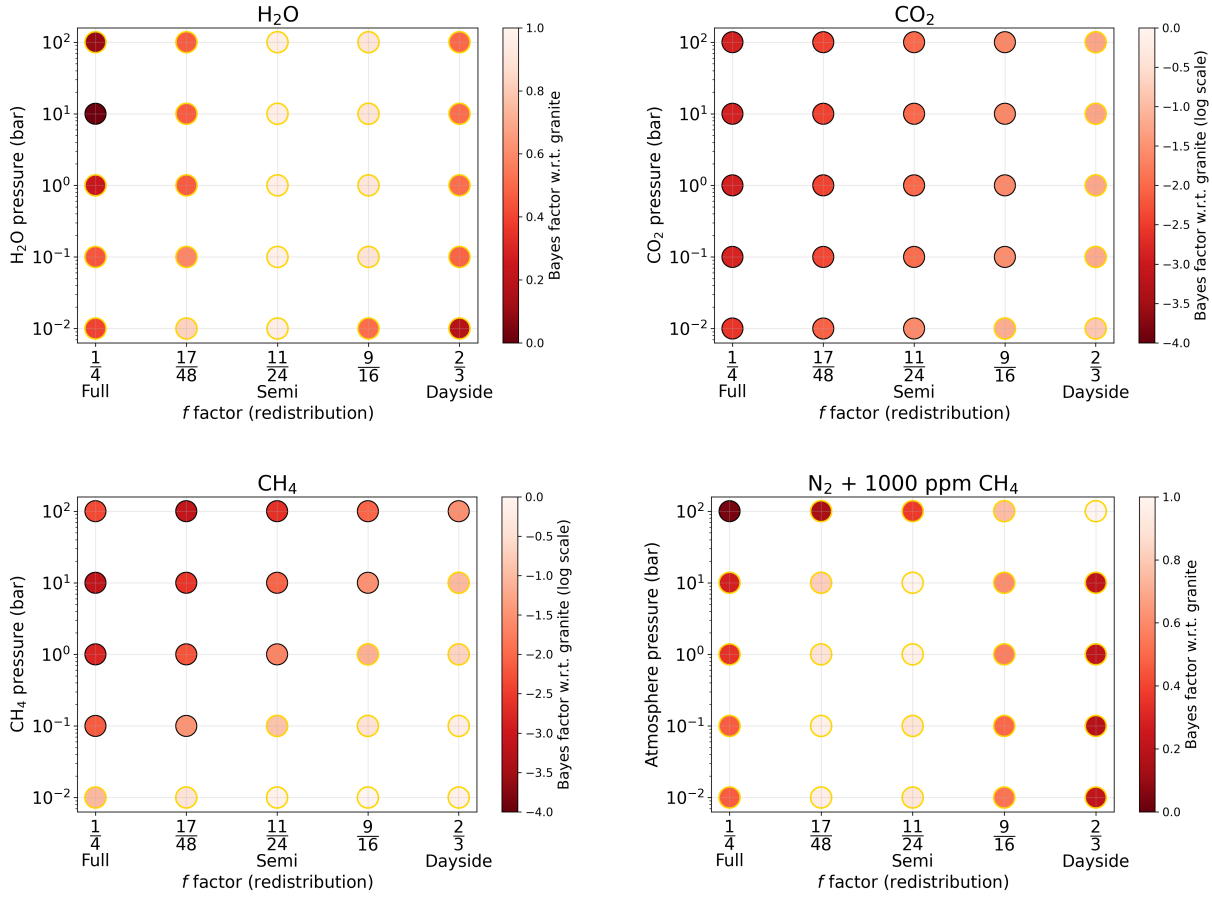

Figure 45: Bayes factors (with respect to granite) for pure H_2O, CO_2, and CH_4, and N_2 + 1000 ppm CH_4 atmospheres at different pressures and heat redistribution (f) factors for TRAPPIST-1c. The Bayes factors of pure CH_4 and CO_2 have been shown in $\log_{10}$ scale; the Bayes factors of pure H_2O and N_2 + 1000 ppm CH_4 are linear.

4.5 Future sensitivity with JWST: GJ 486b and GJ 367b

JWST MIRI photometry has been proposed as an efficient method for detecting atmospheric signatures on rocky exoplanets by measuring deviations from pure blackbody emission. The F1280W and F1500W filters specifically probe potential CO_2 absorption features, which would show as reduced emission relative to the expected blackbody spectrum. However, Hammond et al. [2025] showed a fundamental degeneracy: observed departures from blackbody emission could equally result from atmospheric opacity effects or variations in surface albedo and emissivity.

In this section, I use the spectral models generated by AGNI to simulate JWST MIRI photometric observations of the planets GJ 367b and GJ486b, both of which have not yet been observed with MIRI imaging. By comparing predicted flux ratios between different atmospheric compositions and bare-rock surfaces, the diagnostic power of broadband photometry for distinguishing between atmospheric and surface scenarios can be assessed. This analysis quantifies the extent to which surface-atmosphere degeneracies limit the interpretation of MIRI photometric data for these two planets, with implications for future observational strategies targeting rocky exoplanet atmospheres.

4.5.1 Bare-rock surfaces

Figures 46 and 47 show predicted surface emission signatures for GJ 486b and GJ 367b in the JWST MIRI F1280W and F1500W filters. The simulations assume an observational strategy of four eclipse measurements with a baseline of four eclipse durations observed outside eclipse for background subtraction. Photometric uncertainties are scaled to match the measured 1σ error in the F1500W filter for TRAPPIST-1c [Zieba et al., 2023].

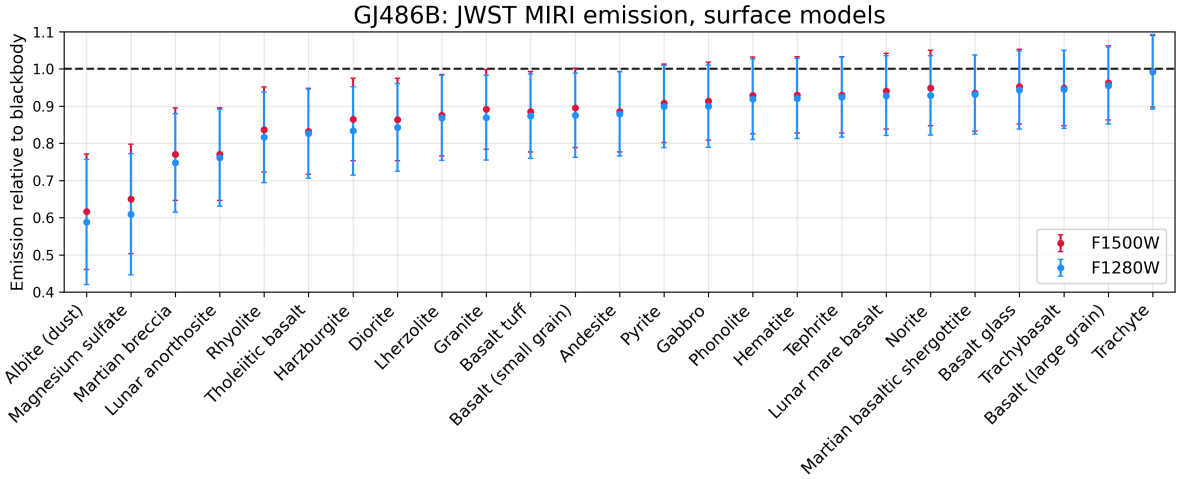

Figure 46: Simulated emissions in the JWST MIRI F1500W and F1280W filters for planet GJ 486b, with respect to the emission of a blackbody (in black). I assumed four observed eclipses, and a baseline of four eclipse durations outside the eclipse. 1σ error bands are included, based on JWST's signal-to-noise ratios, and scaled using the measurement of TRAPPIST-1c in the F1500W filter by Zieba et al. [2023].

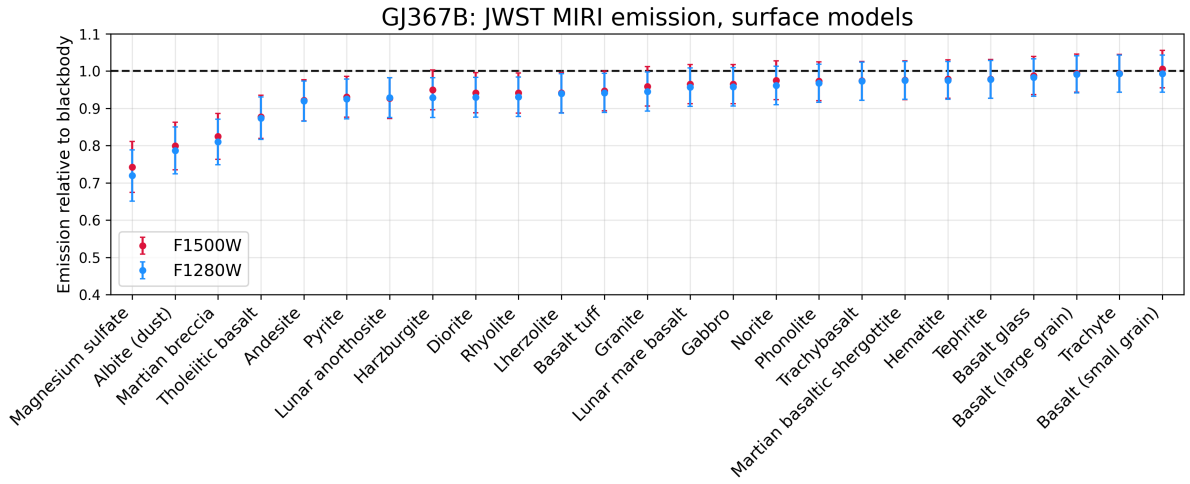

Figure 47: Simulated emissions in the JWST MIRI F1500W and F1280W filters for planet GJ 367b, with respect to the emission of a blackbody (in black). I assumed four observed eclipses, and a baseline of four eclipse durations outside the eclipse. 1σ error bands are included, based on JWST's signal-to-noise ratios, and scaled using the measurement of TRAPPIST-1c in the F1500W filter by Zieba et al. [2023].

4.5.2 GJ 486b atmospheres

I further simulate MIRI photometric signatures for GJ 486b across pure CO_2, H_2O, CH_4, and SO_2 atmospheres, as well as N_2-dominated atmospheres with trace amounts of these species. The grey band represents the complete range of possible surface emissions tested in the spectroscopic analysis, with 1σ error bars. By directly comparing this broad range of surface emission possibilities with predicted atmospheric signatures in the same photometric bands, I can quantitatively assess the degree of degeneracy between surface and atmospheric interpretations for these MIRI imaging filters.

For pure atmospheres, distinguishing between surface albedo effects and atmospheric opacity becomes practically impossible within JWST's photometric precision. While CO_2 and SO_2 possess significant absorption features at or near 15 μm, their emission signatures in both MIRI filters flatten toward similar values at higher pressures, likely due to greenhouse warming effects that increase the overall thermal emission. H_2O atmospheres produce emission signatures nearly indistinguishable from blackbody radiation, while CH_4 shows the only clear atmospheric signature through consistently elevated emission across all pressure regimes.

N_2-dominated atmospheres with 1000 ppm volatile traces show slightly more potential, with pressure-dependent variations becoming more pronounced. Most atmospheres, with CH_4 as the notable exception, show decreasing emission with increasing atmosphere thickness. However, even these variations remain well within the range of surface emission diversity.

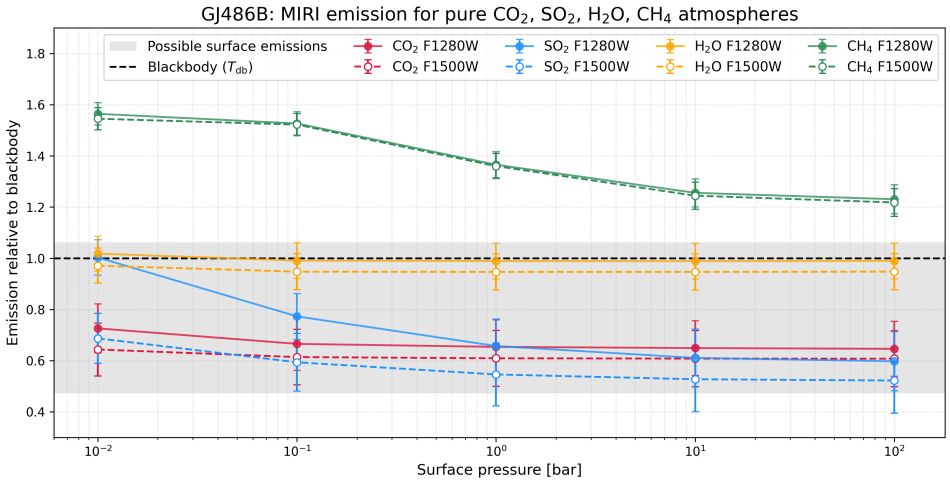

(a) Pure CO_2, SO_2, CH_4 and H_2O atmospheres.

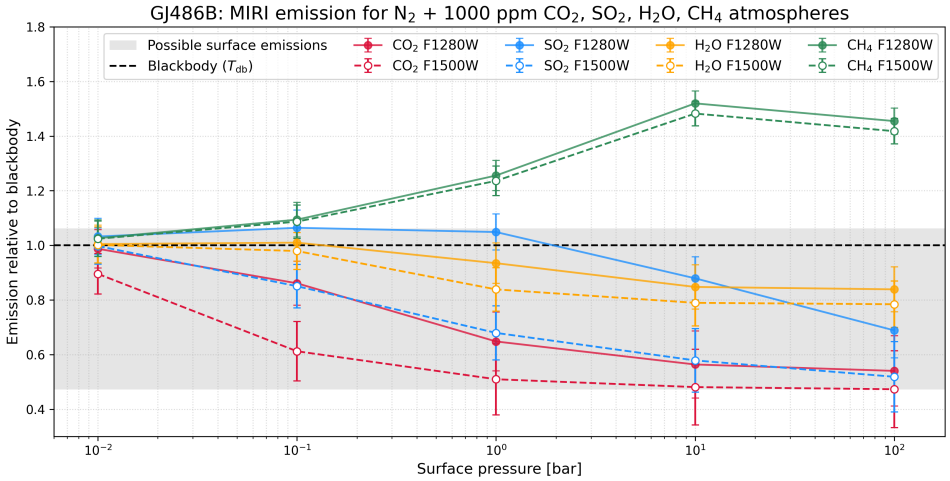

(b) N_2 atmospheres with 1000 ppm CO_2, SO_2, CH_4 traces.

Figure 48: Simulated dayside emission observed through JWST MIRI F1500W and F1280W broadband filters, compared to blackbody emission (black line). The 1σ observational uncertainty bands are derived from four eclipse measurements. The grey band represents the complete range of possible surface emissions modelled in this study. Atmospheric signatures can be distinguished from surface features when the modelled emission (including error bands) falls outside the grey surface emission range.

4.5.3 GJ 486b atmospheres: heat redistribution effects

Following Hammond et al. [2025], I incorporated heat redistribution effects for higher-pressure atmospheres using the methodology of Section 3.1.5. I established a provisional relationship between surface pressure and the heat redistribution efficiency factor (f): no redistribution ($f = \frac{2}{3}$) for 0.01 and 0.1 bar atmospheres, minimal redistribution ($f = 9/16$, corresponding to 25% efficiency) for 1 bar atmospheres, substantial redistribution ($f = 17/48$, corresponding to 75% efficiency) for 10 bar atmospheres, and full redistribution ($f = 1/4$) for 100 bar

atmospheres. These parameter values represent estimates intended to illustrate the potential magnitude of heat redistribution effects rather than precise physical constraints; actual redistribution efficiencies for each pressure would require detailed atmospheric modelling.

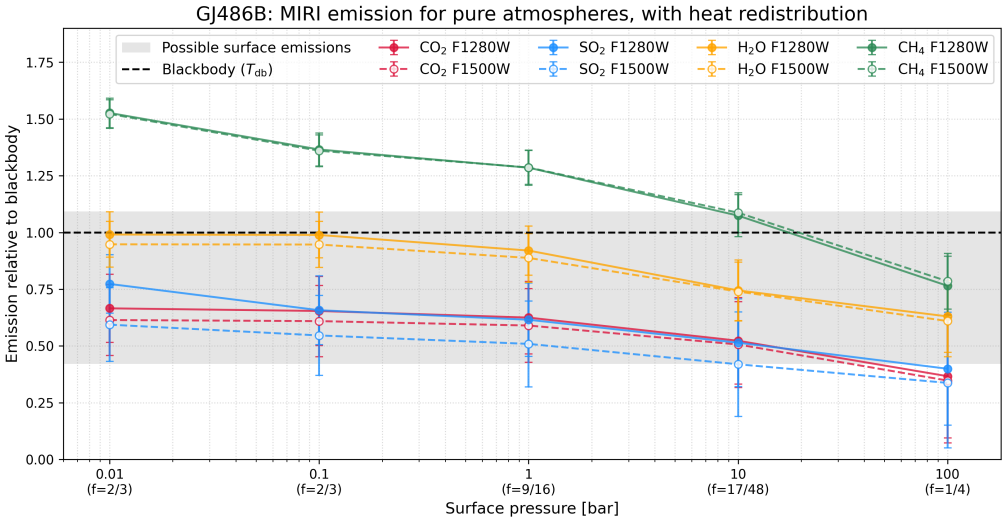

(a) Pure H_2O, CO_2, SO_2, and CH_4 atmospheres, with heat transport mapping.

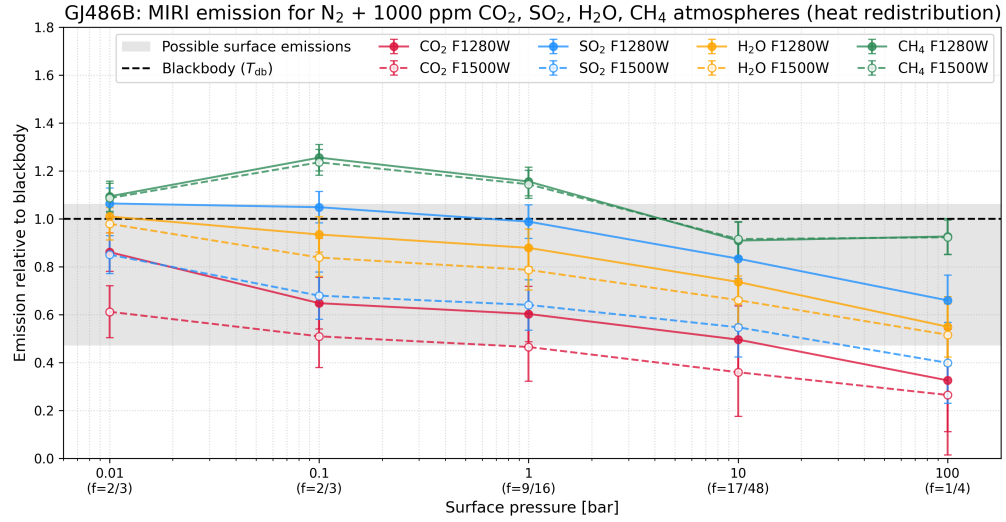

(b) N_2 atmospheres with 1000 ppm traces of H_2O, CO_2, SO_2, and CH_4, with heat transport mapping.

Figure 49: Simulated dayside emission observed through JWST MIRI F1500W and F1280W broadband filters, compared to blackbody emission (black line). Heat redistribution factors were mapped to atmospheric surface pressures as follows: 0.01 and 0.1 bar correspond to f = 2/3 (no heat redistribution); 1 bar to f = 9/16 (25% redistribution efficiency); 10 bar to f = 17/48 (75% redistribution efficiency); and 100 bar to f = 1/4 (100% redistribution efficiency). The grey band represents the complete range of possible surface emissions (in F1280W) modelled in this study. Atmospheric signatures can be distinguished from surface features when the modelled emission (including error bands) falls outside the grey surface emission range.

Thermal emissions in the two MIRI filters were computed for both pure atmospheric compositions and N_2-dominated atmospheres containing 1000 ppm of volatile trace species. The results are presented in Figure 49. I apply the same pressure-dependent redistribution parameterisation to both atmospheric scenarios.

Under the assumption of full heat redistribution, MIRI emissions from 100 bar CO_2 and SO_2 atmospheres begin to fall below the range of possible surface emissions. However, the reduced signal-to-noise ratio associated with smaller eclipse depths results in large uncertainties that complicate clear atmospheric detection. Atmospheres containing H_2O and CH_4 do not produce sufficiently low emission values. Even with heat redistribution, distinguishing high-opacity atmospheres around 15 μm from the highest-albedo bare surfaces remains difficult. Only a N_2 + 1000 ppm CO_2 atmosphere at 100 bar with full heat redistribution shows minimal overlap with possible surface emissions. Reliable atmospheric detection using this observational approach may require either a greater number of eclipse observations than modelled here (more than four eclipses), or could be made possible by increased albedo due to the formation of clouds in thick atmospheres, which was not accounted for in my analysis.

4.5.4 GJ 367b atmospheres

In a similar way as for GJ 486b, I simulated thermal emissions in the two JWST MIRI broadband filters, F1500W and F1280W, for planet GJ 367b. Figure 50 shows the results for pure CO_2, SO_2, H_2O, and CH_4 atmospheres, as well as N_2 atmospheres with 1000 ppm and 1 ppm traces of these gases. For completeness, the 1 ppm trace atmospheres have been included as well for this planet, as the results show a significantly more optimistic picture for atmospheric detectability than was the case for GJ 486b.

GJ 367b offers substantially better prospects for distinguishing atmospheric signatures from surface emissions using MIRI broadband photometry. Pure CO_2 and SO_2 atmospheres, even at lower pressures (0.1 - 1 bar) produce emission reductions that approach or fall below the range of possible surface emissions, particularly in the F1500W filter where CO_2 absorption features are prominent. Most notably, N_2 atmospheres with CO_2 traces show the strongest atmospheric signatures: at 1 bar, N_2 + 1000 ppm CO_2 produces emissions that clearly fall outside the grey band of surface possibilities in both filters. For 1 bar, N_2 + 1000 ppm SO_2, atmosphere emissions start to fall below surface emissions starting from 10 bar. In the F1500W band, even the more dilute N_2 + 1 ppm CO_2 atmosphere at 10 and 100 bar shows emissions below the surface range.

A severe degeneracy between H_2O atmospheres and possible bare-rock surface emissions remains. An emission feature above the expected blackbody curve, on the other hand, could indicate the presence of large amounts of CH_4; and a similar emission feature is produced by thick (10 - 100 bar), N_2-dominated atmospheres with 1 ppm traces of SO_2.

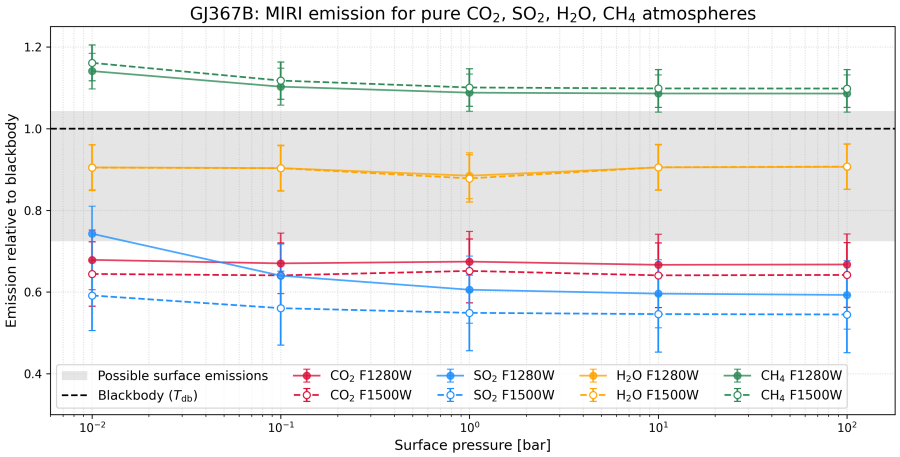

(a) Pure CO_2, SO_2, CH_4 and H_2O atmospheres.

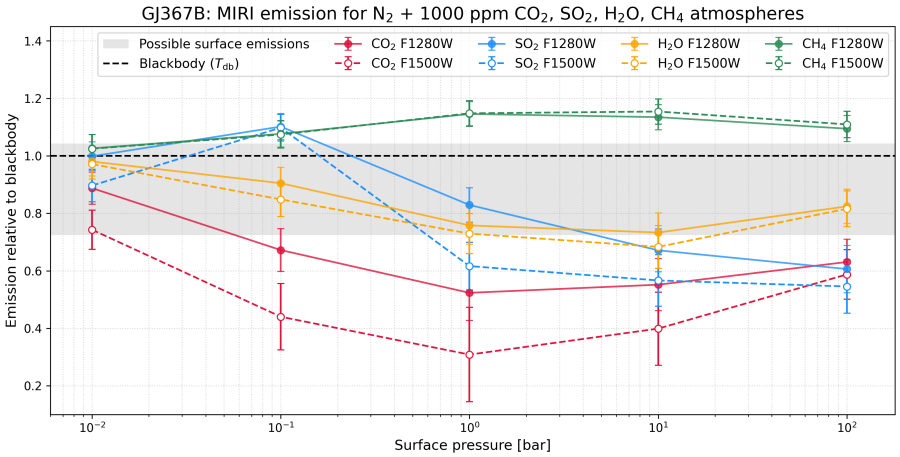

(b) N_2 atmospheres with 1000 ppm CO_2, SO_2, CH_4 traces.

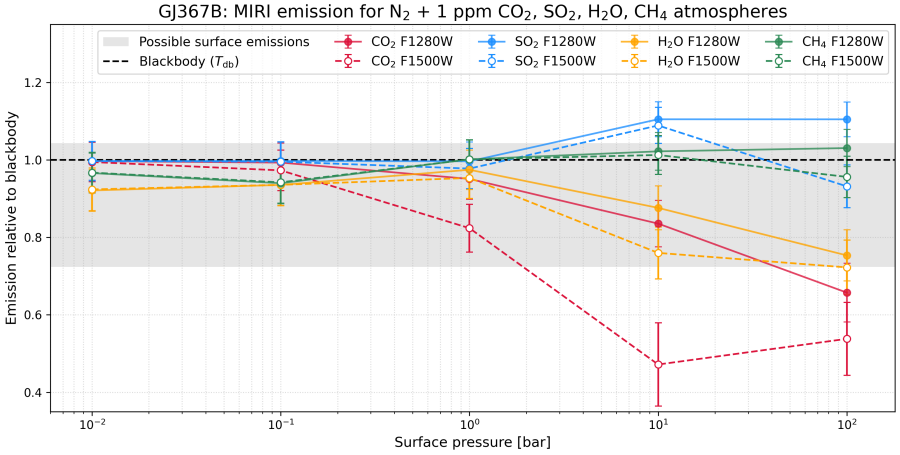

(c) N_2 atmospheres with 1ppm CO_2, SO_2, CH_4 traces.

Figure 50: Simulated dayside emission observed through JWST MIRI F1500W and F1280W broadband filters, compared to blackbody emission (black line). The grey band represents the complete range of possible surface emissions modelled in this study.

4.5.5 GJ 367b atmospheres: heat redistribution effects

I include the pressure-redistribution mapping as was done for planet GJ 486b. The results, as shown in Figure 51 confirm the results without heat transport, and show even lower emissions at high surface pressure. Between 1 an 100 bar surface pressure, the tentative mapping suggests that both SO_2 and CO_2 atmospheres can be clearly distinguished from possible surface emissions in both filters. For N_2-atmospheres with 1000 ppm CO_2, this is the case for all modelled pressures. Notably, even N_2 + 1000 ppm H_2O-atmospheres approach fall below the lowest surface emissions at pressures between 10 and 100 bar. The emission feature of CH_4, on the other hand, disappears at high surface pressures.

The incorporation of heat redistribution significantly enhances the atmospheric detectability for GJ 367b compared to the zero-redistribution case. As heat transport becomes more efficient, the reduced dayside temperatures lead to lower thermal emission that becomes increasingly distinguishable from surface-only scenarios. This effect is particularly pronounced for CO_2-bearing atmospheres, where the combination of atmospheric opacity and heat redistribution creates emission departures from a blackbody that fall well outside the range of possible surface emissions. The enhanced contrast suggests that MIRI broadband photometry could reliably detect thick atmospheres on GJ 367b. Nevertheless, the heat redistribution efficiencies assumed in this analysis might not all be physically realistic for each atmospheric composition and pressure, which adds some uncertainty.

While the likelihood for a thick CO_2 or SO_2 bearing atmosphere is very small on GJ 367b, both 100 bar N_2 with 1 ppm of SO_2 and CO_2 atmospheres were consistent with the data, as shown in Section 4.2.2. The same goes for a pure 100 bar H_2O atmosphere. According to my analysis, the latter might be distinguishable from (most) bare-rock surfaces in F1500W and F1280W filters, assuming full heat redistribution. The same goes for a 100 bar N_2 with 1 ppm of CO_2 atmosphere, even without considering heat transport. MIRI photometry observations might, therefore, rule out these atmospheres with confidence.

Figure 51: Simulated dayside emission for GJ 367b observed through JWST MIRI F1500W and F1280W broadband filters, compared to blackbody emission (black line). Heat redistribution factors were mapped to atmospheric surface pressures as follows: 0.01 and 0.1 bar correspond to f = 2/3 (no heat redistribution); 1 bar to f = 9/16 (25% redistribution efficiency); 10 bar to f = 17/48 (75% redistribution efficiency); and 100 bar to f = 1/4 (100% redistribution efficiency). The grey band represents the complete range of possible surface emissions (in F1280W) modelled in this study. Atmospheric signatures can be distinguished from surface features when the modelled emission (including error bands) falls outside the grey surface emission range.

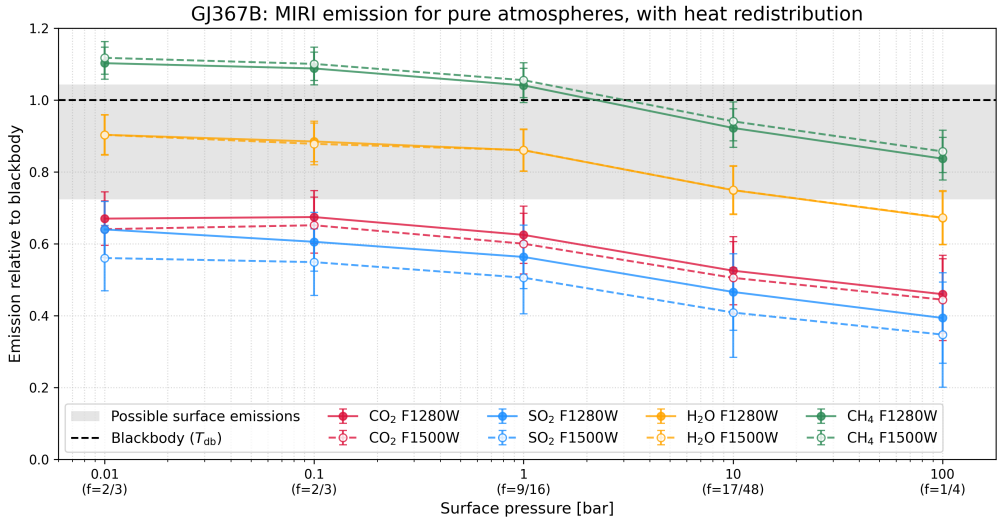

(a) Pure H_2O, CO_2, SO_2, and CH_4 atmospheres, with heat transport mapping.

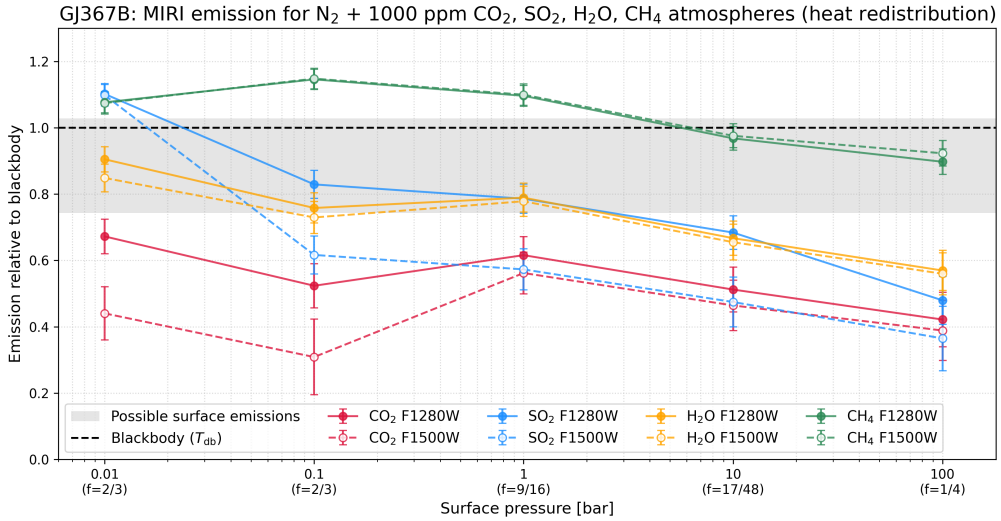

(b) N_2 atmospheres with 1000 ppm traces of H_2O, CO_2, SO_2, and CH_4, with heat transport mapping.

5 Discussion

This thesis had two primary objectives. First, I modelled the dayside emission of M-dwarf exoplanets GJ 486b, GJ 367b, TRAPPIST-1b, and TRAPPIST-1c using the 1D radiative-convective model AGNI across various atmospheric and surface scenarios. I then compared these simulations to mid-infrared MIRI secondary eclipse data from the James Webb Space Telescope (JWST) using a Bayesian model-selection framework to assess the likelihood of atmospheric retention and potentially characterize planetary surfaces.

This work addressed the cosmic shoreline: the proposed, semi-empirical boundary between airless bodies and rocky exoplanets that have retained atmospheres. The main challenge in this context is the observational degeneracy between surface reflection properties and atmospheric opacity in JWST data of rocky exoplanets. Our second objective was therefore to simulate JWST photometric observations in two broadband filters commonly used to assess rocky planets' atmospheric status (F1500W and F1280W) for planets GJ 367b and GJ 486b, both of which have, as of yet, not been observed with MIRI imaging. I aimed to assess the potential of these broadband observations to definitely exclude a bare-rock scenario, or instead, to rule out the presence of specific atmosphere scenarios.

An important addition to both analyses was the inclusion of heat redistribution effects. While true atmospheric circulation could not be modelled, a scaling of the planet's dayside energy budget was implemented to simulate different heat redistribution regimes. For tidally locked planets with atmospheres above 1 bar, heat transport should be taken into account. Different heat distribution scenarios were tested when fitting atmosphere models to JWST data. Additionally, heat transport was included in the simulation of JWST photometry emissions for GJ 367b and GJ 486b.

5.1 Atmosphere and surface models

The first objective of this thesis was to model bare-rock surfaces, as well as atmospheric scenarios on the rocky exoplanets GJ 486b, GJ 367b, TRAPPIST-1b and TRAPPIST-1c, and compare them to mid-infrared observations gathered by JWST in the last two years. This section provides a summary of my findings, discusses their alignment with any theoretical expectations and compares them to recent publications.

5.1.1 GJ 486b: atmosphere results

Based on available data from Mansfield et al. [2024], I found that most thick atmospheric models could be ruled out for GJ 486b. Atmospheres containing CO_2 or SO_2 yielded particularly poor fits. Notable exceptions were H_2O-rich atmospheres with pressures between 0.01 and 100 bar, which consistently outperformed the best surface models. Pure steam atmospheres achieved Bayes factors of ~ 2, while a 0.1 bar nitrogen atmosphere with 1000 ppm water vapour reached ~ 5. Nevertheless, these values are not decisive.

When I incorporated heat redistribution, likely relevant for atmospheres above 1 bar, the evidence for thicker, water-rich atmospheres weakened considerably. None of the H_2O atmospheres with moderate to full heat redistribution provided good fits to the data. This

is worrying, since H_2O-vapour is relatively opaque to long-wavelength radiation, suggesting significant heat transport for these atmospheres [Koll, 2022].

Using transmission spectroscopy, Moran et al. [2023] found that it is most likely for GJ 486b to either have a water-rich atmosphere, or its spectrum to be dominated by stellar contamination. My results favour the first scenario.

On the other hand, my findings contrast with other studies. Ridden-Harper et al. [2023] found no evidence for pure H_2O atmospheres, although they did not rule out other secondary atmospheres containing water. Mansfield et al. [2024] concluded that GJ 486b likely lacks a thick atmosphere entirely and found poor fits for pure H_2O atmospheres above 1 bar. While their water-rich models significantly yielded considerably lower contrasts than the data, my models followed the data well, despite similar spectral shapes. This discrepancy could stem from differences in underlying assumptions and model parameters. I am more optimistic about thick, water-rich atmospheres than Mansfield et al. [2024], but the evidence remains inconclusive.

Nevertheless, a water-rich atmosphere is in line with the geologic simulations of GJ 486b obtained by Sahu et al. [2025]. From a theoretical perspective, atmospheres containing significant amounts of water vapour are generally considered likely for planets of this equilibrium temperature ($\sim$700 K) [Wordsworth and Kreidberg, 2022, Herbort et al., 2020]. Kite and Schaefer [2021] suggest that short-period super-Earths, at least those around Sun-like stars, might retain thick water-rich atmospheres. Johnstone [2020], on the other hand, model that water-vapour atmospheres on planets around active stars might be easily lost due to photodissociation. Still, steam atmospheres are theoretically viable for super-Earths in this equilibrium temperature range.

5.1.2 GJ 486b: surface results

For scenarios assuming minimal or absent atmospheres, surfaces with moderate albedo, such as hematite or tephrite, provided the best fits. The surface pyrite, with a notably lower Bond albedo, also performed well. While I could exclude high-albedo ultramafic surfaces based on the data, no conclusive evidence emerged favouring specific bare-rock surface compositions.

My best fitting model was hematite (Fe_2O_3), consistent with Mansfield et al. [2024], who found that one of their best fitting models was oxidised iron consisting of 50% basalt and 50% hematite. Hematite is common on Mars, where it originates from weathering of iron-bearing minerals [Rasmussen et al., 2014] and is considered evidence of past liquid water [Christensen and Ruff, 2004]. Since GJ 486b is too far outside the habitable zone to sustain liquid water, any hematite formation would more likely result from high-temperature oxidation processes involving water vapour or atmospheric oxygen, or from non-aqueous mechanisms such as volcanic activity [Hynek et al., 2002]. While hematite was not the only well-fitting surface type, its spectral match raises interesting questions about oxidation processes on this planet.

Despite these surface fits, no modelled surfaces reproduced all the spectral features observed in GJ 486b, particularly the features below 7 μm and around 10 μm, and subtler signatures such as the small dip below 8 μm, the small peak above 8.5 μm, and the increasing

slope at longer wavelengths. This suggests additional complexity; potentially a more feature-rich surface composition not considered in this study, stellar contamination, or instrumental artifacts. The features at 7 μm and 10 μm will be discussed further in the next section.

5.1.3 GJ 486b: Features at 7 μm and 10 μm

As mentioned, the emission spectrum of GJ 486b contains considerable contrast dips around 7 μm and 10 μm. These were not accounted for by my bare-rock, or my atmosphere models. The feature just below 7 μm is difficult to explain: H_2O absorbs in this range, but not enough to account for this specific feature.

On the other hand, I showed in Section 4.1.4 that atmospheres with significant amounts of H_2O and traces of O_3 account for the 10 μm feature, and fit the data of GJ 486b better than any other model tried. In fact, three of these atmospheres reaches Bayes factors above 20 with respect to the surface hematite. Ozone is strongly correlated with the presence of oxygen in an atmosphere: the photolysis of O_2 by high-energy UV photons can produce atomic oxygen in its ground triplet state, combining with O_2 to form ozone [Yates et al., 2020]. Yates et al. [2020] found that a thin but stable ozone layer could be formed in the atmosphere of Proxima Centauri b, a nearby exoplanet around an M-star. Moreover, Vidaurri et al. [2024] suggest that M-star flaring could produce both a significant amount of oxygen, and large amounts of ozone on planets with steam atmospheres.

While these findings should not be taken as evidence for ozone, or both oxygen and ozone in the atmosphere of GJ 486b, they are interesting hints which should be explored further in the future.

5.1.4 GJ 367b: atmosphere results

For GJ 367b, I excluded most high-pressure atmospheric scenarios except for relatively transparent, nitrogen-based atmospheres containing 1 ppm trace amounts of the volatiles examined. The best performing atmospheres were those at low pressures (0.01 - 1 bar), where all trace gases (H_2O, CH_4, SO_2, CO_2) performed well. At 1000 ppm abundance alongside nitrogen, both H_2O and CO_2 could not be rejected based on the data.

Interestingly, several high-pressure scenarios remained viable: pure H_2O at 10 and 100 bar, and 100 bar N_2 atmospheres with 1 ppm SO_2 and CO_2. However, surface models generally outperformed atmospheric models, with the best surface model achieving a Bayes factor of $\sim$4 compared to the best atmospheric model. For 100 bar atmospheres, all Bayes factors remained in the lowest acceptable range (0.05 - 0.10).

Including heat transport significantly weakened the evidence for thick atmospheres. Pure H_2O atmospheres were only consistent with no heat redistribution ($f = 2/3$), while nitrogen atmospheres with 1000 ppm CO_2 remained viable up to 1 bar pressure and 50% redistribution efficiency ($\varepsilon = 0.5, f = 11/24$).

These results align with previous work. Zhang et al. [2024] found that H_2O and Earth-like atmospheres up to 1 bar provided the best fits, but their phase curve observations limited heat redistribution efficiency to only 17%. Combined with Poppenhaeger et al. [2024]'s demonstration that high-energy environments would rapidly evaporate any substantial atmosphere, both

studies concluded that a hot and bare surface represents the most likely scenario. Our upper limit of 50% redistribution efficiency for the 1 bar N_2 + 1000 ppm CO_2 atmosphere becomes implausible given Zhang et al.'s 17% constraint, leaving only thin atmospheres as viable, but not the most probable scenarios.

5.1.5 GJ 367b: surface results

Given that GJ 367b is likely a bare planet, characterising its surface composition is of particular interest. However, the limited resolution of available data constrained our analysis, allowing us to reject only a narrow range of high-albedo surfaces, including albite dust and magnesium sulfate. Among the candidate surfaces, pyrite yielded the best fit, closely followed by a substantial group of surfaces with Bayes factors reaching approximately 0.6.

From a geological perspective, four surface compositions are especially relevant for this planet: gabbro, norite, lherzolite, and harzburgite [Spaargaren, personal communication]. My analysis did not reject any of these geologically significant surfaces. The ultramafic compositions – lherzolite and harzburgite – showed the poorest fits among this group, while norite and gabbro emerged as strong candidates for the planet's surface composition.

My findings align with Zhang et al. [2024], who concluded that GJ 367b most likely possesses a low-albedo surface. They encountered similar challenges in distinguishing between specific surface compositions, highlighting the need for higher-resolution spectral observations to achieve more definitive surface characterisation.

5.1.6 TRAPPIST-1b and 1c: atmosphere results

Recent observations of TRAPPIST-1b using both F1500W and F1280W broadband filters [Ducrot et al., 2025] constrain the possible atmospheric compositions to a narrow range. My analysis identified three atmosphere types consistent with these data: high-pressure N_2 atmospheres with 1000 ppm H_2O, low-pressure pure CH_4 atmospheres, and a 100 bar N_2 atmosphere with 1000 ppm CH_4.

Including heat transport effects significantly changed these results. Evidence for thick, pure CH_4 atmospheres weakened, while H_2O and N_2 + 1000 ppm CH_4 atmospheres (up to 10 bar) became more consistent with observations when moderate heat transport was considered. However, both atmosphere types deteriorated under full heat redistribution conditions. Of the viable options, N_2-dominated atmospheres with 1000 ppm CH_4 performed best. These nitrogen-methane atmospheres with heat redistribution efficiencies of 50-75% represent promising candidates for TRAPPIST-1b, despite performing slightly worse than the best surface model (Martian breccia).

My findings contrast with previous studies. Ducrot et al. [2025] identified only a thick, hazy CO_2 atmosphere with temperature inversion as consistent with their data (though with caveats), otherwise suggesting an ultramafic surface. Greene et al. [2023] observed TRAPPIST-1b in F1500W and concluded it likely has a bare rock surface. Neither study specifically examined CH_4 atmospheres, which are generally considered unlikely to accumulate abiotically on terrestrial planets [Wogan et al., 2020, Thompson et al., 2022]. If substantial CH_4 amounts are present on TRAPPIST-1b, this would have significant implications for our understanding of volcanic methane replenishment and methane as a potential biotracer.

TRAPPIST-1c presents a greater challenge for atmospheric characterisation, having been observed only in the F1500W filter, by Zieba et al. [2023]. This allows a broad range of atmospheric compositions to fit the measured contrast.

Two models provided exact matches to the data: a 1 bar N_2 atmosphere with 1 ppm CO_2, and a 100 bar N_2 atmosphere with 1000 ppm CH_4. Interestingly, the latter composition matches the methane atmosphere identified for TRAPPIST-1b. Additionally, between 0.01 and 10 bar surface pressure, N_2 atmospheres with 1000 ppm CH_4 performed well when heat redistribution efficiencies between 50-75% were included.

Furthermore, my results show that thick atmospheres with significant CO_2 concentrations perform poorly. This aligns with the results by Zieba et al. [2023], who concluded that TRAPPIST-1c very unlikely hosts a thick CO_2 atmosphere. Nevertheless, they showed that a 1 bar O_2 atmosphere with 1 ppm CO_2 fits the data well. Given the similar opacity characteristics of O_2 and N_2 at this wavelength, this result is comparable to my 1 bar N_2 with 1 ppm CO_2 model, which exactly matched the observed data point at 15 μm.

Similarly as for TRAPPIST-1b, neither Zieba et al. [2023], or the follow-up study by Lincowski et al. [2023] modelled methane atmospheres on TRAPPIST-1c. Methane atmospheres fitting both TRAPPIST-1 planets well in my analysis is interesting, and might be investigated further in the future.

The main conclusion to draw for TRAPPIST-1c, however, is that more data is needed to make any statements of its atmospheric status with some certainty. Observing the planet in MIRI's F1280W band would be a good initial step.

5.1.7 TRAPPIST-1b and 1c: surface results

Multiple surface compositions fit TRAPPIST-1b's data, making definitive characterisation difficult. Martian breccia, a composite of different Martian rock types, provided the best fit, while mafic (basalt, gabbro) and ultramafic (lherzolite) materials also performed well. However, none precisely reproduced both data points, suggesting either an untested surface composition or modelling limitations.

Atmospheric models did not improve upon the best surface fits. This supports Ducrot et al. [2025]'s conclusion that a moderate-albedo, ultramafic surface is a likely scenario for TRAPPIST-1b. Precise characterisation will require additional data or more extensive bare-rock models.

Surface characterisation proved equally challenging for TRAPPIST-1c. Surfaces with intermediate albedo fit the data well, including granite, harzburgite, gabbro, and basalt. Only albite dust could be excluded. These results align with Zieba et al. [2023], who found ultramafic and basaltic surfaces plausible. Notably, while Zieba et al. [2023] considered unweathered granitoid surfaces marginally worse performers, granite showed the best fit in my analysis, highlighting how specific spectral measurements of rock types can significantly impact results.

5.2 JWST MIRI imaging simulations

GJ 367b and GJ 486b have not yet been observed with MIRI broadband imaging. The F1500W and F1280W filters are recommended for detecting atmospheres on rocky exoplanets, as they

can trace CO_2 (and SO_2) signatures and heat transport [Redfield et al., 2024]. However, Hammond et al. [2025] demonstrated degeneracies between bare-rock scenarios and atmospheres in these bands. I simulated emissions in both filters to assess whether such observations could definitively rule out or confirm atmospheric presence.

My simulated JWST MIRI observations confirm Hammond et al. [2025]'s concerns. For GJ 486b, four eclipse observations yielded atmospheric scenarios all within the range of possible surface emissions. Only CH_4 atmospheres produced consistently elevated emissions distinguishable from surface effects. H_2O atmospheres cannot be distinguished from surface reflectivity in these filters. GJ 367b, on the other hand, showed a more optimistic picture, with several atmospheres producing emissions outside the modelled surface range. This enhanced detectability might stem from the planet's higher equilibrium temperature, which narrows plausible surface emissions. CO_2-bearing atmospheres showed clear signatures.

Heat redistribution effects improved the potential of atmosphere detection, particularly for higher pressures. Efficient heat transport can drive thermal emissions below surface-only scenarios for thick ($\geq$ 10 bar) atmospheres. This effect was most pronounced for GJ 367b, where CO_2 and SO_2 atmospheres with substantial heat redistribution produced emissions clearly outside the surface emission range. Reliance on heat redistribution, however, also introduces uncertainties. The redistribution efficiencies I assumed represent simple estimates rather than physically constrained values. N_2-dominated atmospheres transport heat differently compared to pure CO_2 or SO_2 atmospheres due to differences in optical depth and radiative forcing.

Overall, GJ 367b might be a more promising target than GJ 486b, with several atmospheres potentially detectable without invoking heat transport. MIRI imaging might reliably exclude a range of atmosphere scenarios on this planet. Nevertheless, since most rocky exoplanets will not have characteristics similar to GJ 367b, observations with additional MIRI filters, or alternative approaches like phase curve observations, may be needed.

A persistent challenge is the degeneracy between H_2O atmospheres and bare-rock surface emissions. Water vapour is among the most geophysically plausible atmospheric constituents for rocky planets, yet its spectral signature in the MIRI bands is nearly indistinguishable from blackbody emission. This suggests that alternative observational approaches, such as transmission spectroscopy, phase curve measurements, longer-wavelength thermal emission measurements, or a combination of approaches may be necessary for detecting water-dominated atmospheres.

5.3 Caveats

This analysis is subject to several important limitations, that must be considered when interpreting the results.

5.3.1 Stellar spectrum uncertainty and variability

One of the most important limitations in this study, is the fact that I did not consider uncertainties in the stellar spectra used to calculate secondary eclipse depths. While SPHINX stellar spectra are considered relatively reliable for M-stars [Iyer et al., 2023, Ih et al., 2023], they are synthetic spectra with discrete parameter grids: effective temperatures in 100 K steps,

metallicities in steps of 0.25, log g in steps of 0.25 , and C-to-O ratios in steps of 0.2. I interpolated for temperature differences (e.g., 3300 K SPHINX versus 3317 K measured for GJ 486) but did not account for differences in metallicity, log g, or C-to-O abundance. Additionally, these stellar parameters carry their own uncertainties; GJ 486's effective temperature uncertainty spans 73 K at 2σ, for example. This could significantly shift modelled emission spectra, leading to substantial differences in model fits. Fauchez et al. [2025] demonstrated high degeneracy between stellar parameters and surface albedo for TRAPPIST-1b data.

Stellar contamination is another concern. While it is mostly limiting for transmission spectroscopy, it can also significantly influence emission results [Fauchez et al., 2025]. TRAPPIST-1 is moderately active [Gillon et al., 2016], and GJ 486, though weakly active [Caballero et al., 2022], shows high flaring activity [Diamond-Lowe et al., 2024]. Stellar variability might therefore influence the data used in this thesis. To minimise both issues, Fauchez et al. [2025] suggest accompanying observations for rocky exoplanet atmosphere characterisation with simultaneous mid-IR stellar observations.

5.3.2 Surface samples and atmosphere compositions

The set of surfaces and atmospheres applied in this thesis is not exhaustive. The surfaces modelled represent only a fraction of possible planetary surfaces, and are based on solar system (mostly terrestrial) samples. Rock spectral properties were based on small-grain laboratory samples that may not represent planetary surface conditions. Furthermore, my surface models assumed simple, homogeneous compositions rather than complex mixtures of rocks and minerals or weathered materials.

Atmospheric models were similarly limited. While for GJ 486b I included the trace gases NH_3, HCN, H_2S and CO, the atmospheres modelled for the other three planets remained limited to CO_2, H_2O, CH_4, N_2 and SO_2. I considered only single-component atmospheres, or nitrogen-based atmospheres with merely two different trace gas abundances: 1 and 1000 ppm. A good next step would be to focus on atmospheric species performing well in this study, and to model more trace gas abundances, as well as mixing different gas types. Specific mixes might depend on theoretical atmosphere compositions based on a planet's redox state and temperature. Furthermore, I could not accurately model oxygen-bearing atmospheres. Oxygen could be significant for atmospheric evolution scenarios, and is intrinsically tied to the presence of ozone.

Another important limitation was the exclusion of aerosols such as clouds and hazes, which can significantly impact thermal emission signatures. Aerosols modify the effective emission altitude and temperature-pressure level from which thermal radiation is observed, potentially masking atmospheric gas signatures or even creating spurious spectral features. For example, aerosols might decrease the water feature amplitude with respect to a clear atmosphere by 50% to 70% [Gao et al., 2021]. Furthermore, high-altitude hazes can create temperature inversions, completely altering thermal emission profiles. For rocky planets, relevant aerosols include volcanic sulfur acids, photochemical hazes, and condensation clouds of water or CO_2 [Gao et al., 2021]. A hazy CO_2 atmosphere with a temperature inversion was what fitted the data of TRAPPIST-1b well in Ducrot et al. [2025]'s study, which I could not attempt to reproduce in this thesis. Additionally, Mansfield et al. [2019] show that layers of clouds in a planet's atmosphere can result in an extremely high albedo, decreasing the observed thermal emission. Future work should incorporate aerosol models to better capture these effects.

5.3.3 Heat redistribution and geometry

While heat redistribution was taken into account in this thesis, it was significantly simplified. AGNI is a 1D radiative-convective model that cannot capture the three-dimensional atmospheric circulation processes that transport heat on tidally locked planets. Instead, I applied a scaling factor approach based on Cowan and Agol [2011], simply adjusting the dayside energy budget based on heat redistributio efficiency. The redistribution parameters I used represent simplified estimates rather than physically constrained values derived from atmospheric dynamics. Real heat transport efficiency depends on atmospheric composition, pressure, and stellar irradiation [Koll, 2022], none of which are explicitly accounted for in my scaling approach.

The simplified geometry also introduces uncertainty. My approach uses a fixed zenith angle of 48.19° to represent an average incidence angle across the dayside hemisphere, but this cannot capture the full range of incident angles present in a real three-dimensional system. Additionally, the relationship between observable heat redistribution signatures and atmospheric thickness remains poorly constrained. While I assumed that atmospheres above 1 bar should exhibit significant heat transport, the actual threshold depends on atmosphere composition, as well as on planetary and stellar properties that vary across my sample.

Nevertheless, including heat redistribution effects proved crucial for several conclusions. The weakening of evidence for thick atmospheres when heat transport is considered, particularly for GJ 486b and GJ 367b, suggests that previous studies neglecting these effects may have been overly optimistic about atmospheric retention. On the other hand, TRAPPIST-1b and 1c show that including heat transport might allow for a larger set of viable atmospheres than otherwise. The quantitative reliability, however, of my heat transport regimes remains uncertain, and future work should prioritize more physically motivated treatments of heat transport processes. Three-dimensional general circulation models (GCMs), often used for gaseous exoplanets, would likely yield more accurate atmospheric predictions [Rauscher and Menou, 2012]. The development of computationally efficient parametrisations based on full GCM results could allow for more physical realism while remaining practically applicable.

5.4 Broader context and future developments

This thesis addressed a fundamental question in exoplanet science: to what extent can JWST thermal emission measurements differentiate between bare-rock and atmosphere scenarios on M-star rocky planets, and constrain specific surfaces and atmospheres? My results showed promise, but also limitations of thermal emission observations used for mapping the cosmic shoreline. JWST provides the best sensitivity so far for characterising rocky exoplanets; but degeneracies remain nevertheless. My work showed that while some atmospheric scenarios might be excluded in favourable cases, such as thick CO_2, CH_4 or SO_2 atmospheres, the detection of water-dominated atmospheres remains challenging due to their emission consistently approaching a blackbody. Surface characterisation with JWST's broadband imaging or low-resolution spectroscopy is similarly difficult. Broad compositional or mineralogical categories might be distinguished, but precise identification is not realistic with the limited resolution of the data. The cosmic shoreline thus remains partially concealed by observational degeneracies that no single measurement technique can fully resolve.

Several developments might make a difference in advancing rocky exoplanet characterisation. Combining multiple observational approaches, for instance thermal emission imaging

and spectroscopy with transmission spectroscopy and phase curve measurements, offers a realistic path forward. Phase curve mapping, specifically, directly constrains heat redistribution efficiency, a parameter that my work shows significantly affects atmospheric interpretations.

The Rocky Worlds Director's Discretionary Time (DDT) programme represents an important step in this direction, targeting rocky M-star planets with complementary observational approaches. It aims to observe rocky exoplanets in MIRI's F1500W filter, while simultaneously observing its host star's UV spectrum with Hubble [Evans, 2025]. In this way, it directly targets the cosmic shoreline. Based on my results, the DDT programme will be able to confidently detect thick CO_2 and perhaps even SO_2 atmospheres on certain planets with favourable observability, especially if heat transport plays a significant role. Nevertheless, the downsides of observing thermal emission in just the 15 μm band remain, and follow-up strategies might still be necessary.

In the more distant future, new space missions might allow us to enter a new era, as JWST did this decade. The proposed LIFE (Large Interferometer For Exoplanets) would use nulling interferometry to allow for detailed thermal emission observations of potential habitable worlds. LIFE might offer the resolution that lifts surface-atmosphere degeneracies limiting current observations. It would not only constrain the presence of an atmosphere with confidence, but also enable the detection of atmospheric elements [Alei et al., 2022].

Understanding the cosmic shoreline is relevant to theories of planetary evolution, atmospheric escape, and to the prevalence of potentially habitable worlds. My findings show that, based on current JWST data, reliably excluding thick atmospheres on rocky exoplanets is very difficult. This could be interpreted with optimism; previous studies might have been overly hasty in declaring exoplanets such as GJ 486b or TRAPPIST-1c bare. Instead, it could also be taken as a sign of our current limitations.

While JWST has opened the door to rocky exoplanet characterisation, it cannot fully map the cosmic shoreline. Future progress will depend on combining different JWST observations, as well as complementing this with other observational techniques, using better atmospheric models, and finally, on the development of next-generation instruments.

6 Conclusions

In the search for extraterrestrial life, rocky exoplanets around M-dwarf stars are promising targets. Nevertheless, as these planets are very close to their stars, it is unclear whether their hosts would not strip them of their astmospheres. The *cosmic shoreline* represents a proposed boundary between exoplanets with atmospheres and those without, mapping planets according to their surface gravity and incoming radiation.

This thesis investigated the cosmic shoreline by focusing on four M-star exoplanets: GJ 486b, GJ 367b, TRAPPIST-1b and TRAPPIST-1c. These planets were recently observed with JWST's mid-infrared instrument. I modelled surface and atmospheric compositions using the 1D AGNI radiative-convective model, and used Bayesian selection to compare simulated emission spectra with observational data. Additionally, I tested whether future broadband data of GJ 486b and GJ 367b could distinguish bare-rock from atmosphere scenarios.

For GJ 486b, most thick atmospheric models were excluded. Water-rich atmospheres, on the other hand, fit very well; contradicting Mansfield et al. [2024]. Interestingly, water atmospheres with ozone traces significantly outperformed surface models. The likelihood of abiotic ozone build-up on this planet, however, is uncertain. Furthermore, taking the first-order effects of heat transport into account, the evidence for steam atmospheres weakened substantually. If airless, a moderate albedo is most likely for the planet. Hematite, an iron-oxide, performed best, raising questions about weathering and oxidation processes on the planet.

For GJ 367b, thick atmospheres were unlikely, but not excluded; including heat transport limited plausible atmospheres to those below 1 bar. This is in line with the results of Zhang et al. [2024], who constrained the planet to having, at the most, a thin atmosphere. The best-fitting bare surface was pyrite; and two geologically likely scenarios, norite and gabbro, were also strong candidates. Overall, however, low data resolution limited precise surface constraints.

The TRAPPIST-1 planets, if bare, likely contain mafic to ultramafic surfaces. Nevertheless, surface characterisation was challenging for both planets with the limited data. Additionally, nitrogen atmospheres with trace methane emerged as viable scenarios when heat transport was taken into account, even up to 10 bar. This contrasts with earlier findings suggesting TRAPPIST-1b and 1c have, at most, thin atmospheres Ducrot et al. [2025], Zieba et al. [2023]. Given my models' sensitivity to heat transport, the link between redistribution and atmospheric properties needs further study. Furthermore, since methane is a potential biotracer, an abiotic origin on these planets should be investigated.

Simulated JWST broadband observations showed degeneracies between bare surfaces and atmospheres. Assuming heat redistribution strongly affects thick-atmosphere spectra, SO_2 and CO_2 might be distinguishable from surfaces on favourable targets like GJ 367b. Nevertheless, water atmospheres will likely not easily be discerned with imaging. Progress in mapping the cosmic shoreline requires combining multiple JWST observational techniques – imaging, phase curve mapping and both emission and transmission spectroscopy – as well as using different instruments, such as will be done in the Rocky Worlds DDT programme. While JWST has gotten rocky exoplanet characterisation within reach, confidently detecting atmosphere presence on rocky M-star exoplanets remains a challenge, requiring both combined observational strategies, and continued technological advancement.

Acknowledgements

In the first instance, this thesis came into existence not because of me, but because of the efforts and ideas of my supervisor and co-supervisor, Tim Lichtenberg and Mark Hammond. While I have made it my own, I want to thank both for their technical, theoretical and moral support. Tim, thank you for arranging this thesis. You included me in the group very early on, which gave me a great start. You had time to see me almost every week, were available for questions at almost any hour, and read through and commented on long weekly updates and an even longer first draft. Mark, thank you for meeting me online and keeping up with my results, as well as having the time to go through my unending list of technical questions, giving me tips and feedback, and even attending my presentation through Zoom despite the very early hour.

I'd also like to thank the full Forming Worlds group. Many of you were prepared to help from the start: helping me install my setup, giving me tips throughout the thesis, sending me bits of code and spending over an hour to give feedback on my presentation. In particular, I want to thank Harrison Nicholls, although we never met in person. Harrison seemed to be online almost every hour of the day to answer any question I had about his model.

In addition, I would like to thank Kristof de Bruyn, for reading my thesis and attending my presentation as a second examiner, despite working in a completely different field. I hope it was an interesting read in part.

Finally, I would like to thank my parents for always being proud, supportive and enthusiastic about what I am doing, even if it is about planets outside of the solar system. And, of course, I want to thank Paula, without whom I would probably still be writing the literature review. You gave me endless space and support to make this thesis, put up with me when I was busy or stressed, and read through it at the very last moment. Thank you.

Statement on the use of AI

In writing this thesis, generative AI was used as a tool to assist with language improvement, including sentence structure and word choice. The research methodology, analysis, interpretations, and all substantive content represent original work.

A Bayesian model selection: tables

Summaries of the Bayesian model comparison for all surface and atmosphere models, for the planets GJ 486b, GJ 367b, TRAPPIST-1b and TRAPPIST-1c have been shown in the upcoming tables.

A.1 GJ 486b

A.1.1 Surfaces

Table 6 shows the Bayesian model comparison summary for GJ 486b surface models.

Surface	Reduced χ^2	$\ln Z$	$\Delta \ln Z$	Bayes factor	Consistent?
Hematite	1.20	-12.70	0.00	1.00	Yes
Pyrite	1.26	-13.23	-0.53	0.59	Yes
Tephrite	1.21	-13.14	-0.44	0.64	Yes
Basalt glass	1.30	-14.05	-1.35	0.26	Yes
Trachy basalt	1.38	-14.08	-1.38	0.25	Yes
Phonolite	1.30	-14.08	-1.38	0.25	Yes
Gabbro	1.32	-14.24	-1.54	0.21	Yes
Basalt tuff	1.40	-14.32	-1.62	0.20	Yes
Mars basaltic shergottite	1.38	-14.50	-1.80	0.17	Yes
Norite	1.40	-14.75	-2.05	0.13	Yes
Lherzolite	1.43	-15.10	-2.40	0.09	Yes
Granite	1.48	-15.24	-2.54	0.08	Yes
Basalt large	1.55	-15.29	-2.59	0.07	Yes
Trachyte	1.85	-15.39	-2.69	0.07	Yes
Lunar mare basalt	1.52	-15.65	-2.95	0.05	Yes
Diorite	1.64	-15.71	-3.01	0.05	No
Basalt small	1.66	-16.36	-3.66	0.03	No
Rhyolite	1.98	-17.31	-4.61	0.01	No
Harzburgite	1.87	-17.94	-5.24	0.01	No
Andesite	1.78	-19.15	-6.45	0.00	No
Tholeiitic basalt	2.31	-24.75	-12.05	0.00	No
Lunar anorthosite	3.20	-25.00	-12.30	0.00	No
Martian breccia	2.75	-28.87	-16.17	0.00	No
Magnesium sulfate	8.02	-59.13	-46.43	0.00	No
Albite dust	8.45	-63.79	-51.09	0.00	No

Table 6: Bayesian model comparison of bare-rock surfaces for GJ 486b, with hematite as a reference model. A model is considered consistent with the data when Δ ln Z > -3. Data: `https://github.com/stuitje/VAYU/tree/main/out/gj486b/bayes_model_comparison_surface.csv`.

A.1.2 Atmospheres

Table 7 shows the Bayesian model comparison summary for GJ 486b pure atmosphere models. Tables 9 and 8 show the model comparison for N_2-based atmospheres with 1000 ppm and 1 ppm trace gases, respectively.

Atmosphere	Reduced χ^2	$\ln Z$	$\Delta \ln Z$	Bayes factor	Consistent?
0.01 bar, CO_2	5.01	-34.54	-21.87	3.16e-10	No
0.01 bar, H_2O	**1.39**	**-12.50**	**0.16**	**1.18**	**Yes**
0.01 bar, SO_2	10.37	-100.09	-87.42	1.08e-38	No
0.01 bar, CH_4	2.45	-25.80	-13.13	1.99e-06	No
0.1 bar, CO_2	8.40	-59.37	-46.70	5.23e-21	No
0.1 bar, H_2O	1.24	-12.27	0.40	1.49	Yes
0.1 bar, SO_2	13.08	-113.06	-100.39	2.52e-44	No
0.1 bar, CH_4	2.22	-23.67	-11.00	1.67e-05	No
1 bar, CO_2	10.13	-72.70	-60.03	8.50e-27	No
1 bar, H_2O	1.22	-12.21	0.46	1.59	Yes
1 bar, SO_2	15.26	-132.00	-119.33	1.50e-52	No
1 bar, CH_4	1.93	-20.75	-8.08	3.10e-04	No
10 bar, CO_2	5.95	-53.67	-41.00	1.56e-18	No
10 bar, H_2O	1.22	-12.20	0.47	1.60	Yes
10 bar, SO_2	16.22	-141.44	-128.77	1.19e-56	No
10 bar, CH_4	1.80	-19.30	-6.64	1.31e-03	No
100 bar, CO_2	3.61	-37.34	-24.67	1.93e-11	No
100 bar, H_2O	1.23	-12.14	0.52	1.69	Yes
100 bar, SO_2	16.50	-150.48	-137.81	1.41e-60	No
100 bar, CH_4	1.76	-18.82	-6.16	2.12e-03	No

Table 7: Bayesian model comparison for all pure atmospheric models of GJ 486b, showing the log-evidence (ln Z), difference in log evidence with respect to the surface hematite (Δ ln Z) and the Bayes factor with respect to hematite. Models with Δ ln Z > -3, corresponding to a Bayes factor of 0.05, are considered consistent with the data. The best performing model with respect to hematite has been made bold. The reduced chi-squared value is also shown. All atmosphere data: `https://github.com/stuitje/VAYU/tree/main/out/gj486b/bayes_model_comparison_atmo.csv`.

Table 8: GJ 486b: N_2 atmospheric models with 1 ppm trace gases.

Atmosphere	Reduced χ^2	$\ln Z$	$\Delta \ln Z$	Bayes factor	Consistent?
0.01 bar N_2, 1 ppm CO_2	2.62	-17.97	-5.30	4.98e-03	No
0.1 bar N_2, 1 ppm CO_2	2.13	-16.32	-3.65	2.60e-02	No
1 bar N_2, 1 ppm CO_2	2.96	-18.97	-6.30	1.84e-03	No
10 bar N_2, 1 ppm CO_2	3.44	-20.80	-8.13	2.95e-04	No
100 bar N_2, 1 ppm CO_2	4.28	-27.48	-14.81	3.70e-07	No
0.01 bar N_2, 1 ppm H_2O	5.24	-25.62	-12.95	2.37e-06	No
0.1 bar N_2, 1 ppm H_2O	14.32	-63.62	-50.95	7.46e-23	No
1 bar N_2, 1 ppm H_2O	12.32	-39.37	-26.70	2.54e-12	No
10 bar N_2, 1 ppm H_2O	9.76	-31.93	-19.26	4.33e-09	No
100 bar N_2, 1 ppm H_2O	3.60	-21.43	-8.77	1.56e-04	No
0.01 bar N_2, 1 ppm SO_2	2.04	-16.07	-3.40	3.32e-02	No
0.1 bar N_2, 1 ppm SO_2	1.92	-16.15	-3.48	3.08e-02	No
1 bar N_2, 1 ppm SO_2	2.59	-26.16	-13.50	1.37e-06	No
10 bar N_2, 1 ppm SO_2	6.94	-72.84	-60.17	7.37e-27	No
100 bar N_2, 1 ppm SO_2	11.06	-116.56	-103.89	7.61e-46	No
0.01 bar N_2, 1 ppm CH_4	3.19	-19.72	-7.05	8.67e-04	No
0.1 bar N_2, 1 ppm CH_4	3.98	-21.96	-9.30	9.17e-05	No
1 bar N_2, 1 ppm CH_4	1.92	-15.42	-2.75	6.37e-02	Yes
10 bar N_2, 1 ppm CH_4	3.16	-28.61	-15.94	1.19e-07	No
100 bar N_2, 1 ppm CH_4	4.70	-48.37	-35.70	3.13e-16	No
0.01 bar N_2, 1 ppm CO	2.28	-17.11	-4.45	1.17e-02	No
0.1 bar N_2, 1 ppm CO	2.14	-16.54	-3.87	2.08e-02	No
1 bar N_2, 1 ppm CO	**1.79**	**-14.99**	**-2.32**	**9.85e-02**	**Yes**
10 bar N_2, 1 ppm CO	3.29	-19.86	-7.20	7.49e-04	No
100 bar N_2, 1 ppm CO	2.69	-18.47	-5.80	3.02e-03	No
0.01 bar N_2, 1 ppm HCN	5.97	-26.94	-14.27	6.34e-07	No
0.1 bar N_2, 1 ppm HCN	5.05	-24.60	-11.94	6.55e-06	No
1 bar N_2, 1 ppm HCN	4.93	-24.00	-11.33	1.20e-05	No
10 bar N_2, 1 ppm HCN	6.96	-28.24	-15.58	1.72e-07	No
100 bar N_2, 1 ppm HCN	9.78	-35.09	-22.42	1.84e-10	No
0.01 bar N_2, 1 ppm H_2S	2.07	-16.14	-3.48	3.10e-02	No
0.1 bar N_2, 1 ppm H_2S	2.13	-16.32	-3.65	2.60e-02	No
1 bar N_2, 1 ppm H_2S	9.43	-34.50	-21.83	3.29e-10	No
10 bar N_2, 1 ppm H_2S	21.30	-54.06	-41.39	1.06e-18	No
100 bar N_2, 1 ppm H_2S	20.34	-65.05	-52.38	1.79e-23	No
0.01 bar N_2, 1 ppm NH_3	23.45	-56.64	-43.98	7.96e-20	No
0.1 bar N_2, 1 ppm NH_3	21.61	-54.59	-41.92	6.24e-19	No
1 bar N_2, 1 ppm NH_3	16.08	-47.14	-34.48	1.06e-15	No
10 bar N_2, 1 ppm NH_3	6.91	-31.63	-18.96	5.81e-09	No
100 bar N_2, 1 ppm NH_3	11.10	-36.29	-23.62	5.52e-11	No

Table 9: GJ 486b: N_2 atmospheric models with 1000 ppm trace gases.

Atmosphere	Reduced χ^2	$\ln Z$	$\Delta \ln Z$	Bayes factor	Consistent?
0.01 bar N_2, 1000 ppm CO	2.41	-17.55	-4.88	7.58e-03	No
0.01 bar N_2, 1000 ppm CO_2	2.42	-17.37	-4.70	9.07e-03	No
0.01 bar N_2, 1000 ppm H_2O	1.94	-15.11	-2.44	8.70e-02	Yes
0.01 bar N_2, 1000 ppm H_2S	2.07	-16.17	-3.51	3.00e-02	No
0.01 bar N_2, 1000 ppm HCN	1.94	-15.06	-2.39	9.13e-02	Yes
0.01 bar N_2, 1000 ppm SO_2	4.71	-49.73	-37.06	8.00e-17	No
0.01 bar N_2, 1000 ppm CH_4	1.92	-16.06	-3.39	3.37e-02	No
0.01 bar N_2, 1000 ppm NH_3	1.65	-15.48	-2.82	5.99e-02	Yes
0.1 bar N_2, 1000 ppm CO	2.61	-17.66	-4.99	6.80e-03	No
0.1 bar N_2, 1000 ppm CO_2	3.20	-20.35	-7.68	4.61e-04	No
0.1 bar N_2, 1000 ppm H_2O	**1.31**	**-11.60**	**1.07**	**2.91**	**Yes**
0.1 bar N_2, 1000 ppm H_2S	2.00	-15.52	-2.85	5.74e-02	Yes
0.1 bar N_2, 1000 ppm HCN	1.99	-17.11	-4.45	1.17e-02	No
0.1 bar N_2, 1000 ppm SO_2	9.37	-98.71	-86.04	4.29e-38	No
0.1 bar N_2, 1000 ppm CH_4	2.33	-22.93	-10.26	3.49e-05	No
0.1 bar N_2, 1000 ppm NH_3	1.99	-17.25	-4.58	1.03e-02	No
1 bar N_2, 1000 ppm CO	3.13	-19.61	-6.94	9.68e-04	No
1 bar N_2, 1000 ppm CO_2	5.47	-42.42	-29.75	1.20e-13	No
1 bar N_2, 1000 ppm H_2O	2.02	-21.41	-8.74	1.60e-04	No
1 bar N_2, 1000 ppm H_2S	1.44	-14.00	-1.33	2.65e-01	Yes
1 bar N_2, 1000 ppm HCN	4.54	-38.16	-25.49	8.52e-12	No
1 bar N_2, 1000 ppm SO_2	10.84	-111.60	-98.93	1.08e-43	No
1 bar N_2, 1000 ppm CH_4	2.61	-27.75	-15.08	2.81e-07	No
1 bar N_2, 1000 ppm NH_3	1.78	-15.69	-3.02	4.88e-02	Yes
10 bar N_2, 1000 ppm CO	4.66	-27.60	-14.93	3.27e-07	No
10 bar N_2, 1000 ppm CO_2	8.89	-69.86	-57.19	1.46e-25	No
10 bar N_2, 1000 ppm H_2O	2.52	-22.48	-9.81	5.48e-05	No
10 bar N_2, 1000 ppm H_2S	2.93	-30.31	-17.64	2.18e-08	No
10 bar N_2, 1000 ppm HCN	5.59	-51.52	-38.86	1.33e-17	No
10 bar N_2, 1000 ppm SO_2	12.38	-113.50	-100.83	1.62e-44	No
10 bar N_2, 1000 ppm CH_4	2.64	-28.13	-15.47	1.92e-07	No
10 bar N_2, 1000 ppm NH_3	2.08	-17.26	-4.60	1.01e-02	No
100 bar N_2, 1000 ppm CO	5.19	-32.61	-19.94	2.18e-09	No
100 bar N_2, 1000 ppm CO_2	10.66	-88.70	-76.04	9.50e-34	No
100 bar N_2, 1000 ppm H_2O	2.61	-22.99	-10.32	3.28e-05	No
100 bar N_2, 1000 ppm H_2S	3.47	-30.87	-18.20	1.25e-08	No
100 bar N_2, 1000 ppm HCN	4.16	-42.98	-30.31	6.86e-14	No
100 bar N_2, 1000 ppm SO_2	15.32	-133.97	-121.31	2.07e-53	No
100 bar N_2, 1000 ppm CH_4	2.46	-25.74	-13.07	2.10e-06	No
100 bar N_2, 1000 ppm NH_3	2.19	-17.67	-5.00	6.73e-03	No

A.2 GJ 367b

A.2.1 Surfaces

Table 10 shows the Bayesian model comparison summary for GJ 367b surface models.

Surface	Reduced χ^2	$\ln Z$	$\Delta \ln Z$	Bayes factor	Consistent?
Pyrite	1.74	-8.77	0.00	1.00	Yes
Phonolite	1.85	-9.48	-0.71	0.49	Yes
Norite	1.86	-9.50	-0.72	0.49	Yes
Gabbro	1.87	-9.50	-0.72	0.48	Yes
Tephrite	1.82	-9.33	-0.56	0.57	Yes
Basalt glass	1.86	-9.38	-0.61	0.55	Yes
Basalt small	1.86	-9.44	-0.67	0.51	Yes
Diorite	1.93	-9.53	-0.76	0.47	Yes
Hematite	1.91	-9.60	-0.83	0.44	Yes
Granite	1.94	-9.67	-0.89	0.41	Yes
Mars basaltic shergottite	1.90	-9.71	-0.94	0.39	Yes
Basalt large	1.90	-9.75	-0.98	0.38	Yes
Rhyolite	1.99	-9.87	-1.10	0.33	Yes
Trachy basalt	1.96	-10.01	-1.24	0.29	Yes
Lherzolite	1.99	-10.11	-1.33	0.26	Yes
Basalt tuff	2.02	-10.17	-1.40	0.25	Yes
Lunar mare basalt	1.99	-10.18	-1.41	0.24	Yes
Trachyte	2.02	-10.28	-1.50	0.22	Yes
Lunar anorthosite	2.20	-10.86	-2.09	0.12	Yes
Harzburgite	2.18	-10.92	-2.15	0.12	Yes
Andesite	2.23	-11.25	-2.48	0.08	Yes
Tholeiitic basalt	2.40	-12.13	-3.36	0.03	No
Mars breccia	2.49	-12.24	-3.46	0.03	No
Albite dust	3.66	-16.09	-7.32	0.00	No
Magnesium sulphate	5.36	-23.06	-14.28	0.00	No

Table 10: Bayesian model comparison of bare-rock surfaces for GJ 367b, with pyrite used as a reference model. A model is considered consistent with the data when Δ ln Z > -3. Data: `https://github.com/stuitje/VAYU/tree/main/out/gj367b/bayes_model_comparison_surface.csv`.

A.2.2 Atmospheres

Table 11 shows the Bayesian model comparison summary for GJ 367b pure atmosphere models. Tables 12 and 13 show the model comparison for N_2-based atmospheres with 1000 ppm and 1 ppm trace gases, respectively.

Atmosphere	Reduced χ^2	$\ln Z$	$\Delta \ln Z$	Bayes Factor	Consistent?
0.01 bar CO_2	2.520	-12.709	-3.870	2.086e-02	No
0.1 bar CO_2	3.436	-17.192	-8.353	2.357e-04	No
1 bar CO_2	3.333	-16.890	-8.051	3.188e-04	No
10 bar CO_2	2.953	-14.800	-5.960	2.579e-03	No
100 bar CO_2	2.921	-14.626	-5.787	3.067e-03	No
0.01 bar H_2O	**2.455**	**-11.796**	**-2.957**	**5.199e-02**	**Yes**
0.1 bar H_2O	2.465	-11.856	-3.017	4.895e-02	No
1 bar H_2O	2.801	-13.133	-4.294	1.365e-02	No
10 bar H_2O	2.441	-11.732	-2.893	5.544e-02	Yes
100 bar H_2O	2.424	-11.734	-2.895	5.533e-02	Yes
0.01 bar SO_2	9.299	-42.291	-33.451	2.967e-15	No
0.1 bar SO_2	10.965	-49.336	-40.497	2.584e-18	No
1 bar SO_2	11.700	-52.767	-43.928	8.363e-20	No
10 bar SO_2	11.917	-53.944	-45.105	2.577e-20	No
100 bar SO_2	11.989	-53.982	-45.143	2.482e-20	No
0.01 bar CH_4	3.886	-17.935	-9.096	1.122e-04	No
0.1 bar CH_4	3.838	-17.592	-8.752	1.581e-04	No
1 bar CH_4	3.749	-17.153	-8.314	2.451e-04	No
10 bar CH_4	3.640	-16.738	-7.899	3.711e-04	No
100 bar CH_4	3.515	-16.236	-7.397	6.133e-04	No

Table 11: Bayesian model comparison for all pure atmospheric models of GJ 367b, showing the log-evidence (ln Z), difference in log evidence with respect to the surface pyrite (Δ ln Z) and the Bayes factor with respect to pyrite. Models with Δ ln Z > -3, corresponding to a Bayes factor of 0.05, are considered consistent with the data. The best performing model has been made bold. The reduced chi-squared value is also shown. All atmosphere data: `https://github.com/stuitje/VAYU/tree/main/out/gj367b/bayes_model_comparison_atmo.csv`.

Table 12: GJ 367b: N_2 atmospheric models with 1000 ppm trace gases.

Atmosphere	Reduced χ^2	$\ln Z$	$\Delta \ln Z$	Bayes Factor	Consistent?
0.01 bar N_2, 1000 ppm CO_2	**2.145**	**-10.739**	**-1.899**	**0.150**	**Yes**
0.1 bar N_2, 1000 ppm CO_2	2.776	-12.562	-3.723	2.416e-02	No
1 bar N_2, 1000 ppm CO_2	2.278	-11.617	-2.778	6.215e-02	Yes
10 bar N_2, 1000 ppm CO_2	3.098	-15.713	-6.873	1.035e-03	No
100 bar N_2, 1000 ppm CO_2	3.691	-18.684	-9.845	5.300e-05	No
0.01 bar N_2, 1000 ppm H_2O	2.060	-10.543	-1.704	1.820e-01	Yes
0.1 bar N_2, 1000 ppm H_2O	2.713	-13.309	-4.469	1.146e-02	No
1 bar N_2, 1000 ppm H_2O	5.481	-24.033	-15.193	2.521e-07	No
10 bar N_2, 1000 ppm H_2O	6.292	-27.570	-18.731	7.333e-09	No
100 bar N_2, 1000 ppm H_2O	3.316	-14.944	-6.104	2.233e-03	No
0.01 bar N_2, 1000 ppm SO_2	5.061	-25.219	-16.380	7.698e-08	No
0.1 bar N_2, 1000 ppm SO_2	3.304	-13.996	-5.156	5.762e-03	No
1 bar N_2, 1000 ppm SO_2	8.014	-37.584	-28.745	3.283e-13	No
10 bar N_2, 1000 ppm SO_2	10.074	-45.393	-36.554	1.333e-16	No
100 bar N_2, 1000 ppm SO_2	11.387	-51.121	-42.282	4.336e-19	No
0.01 bar N_2, 1000 ppm CH_4	2.832	-14.318	-5.479	4.175e-03	No
0.1 bar N_2, 1000 ppm CH_4	3.775	-18.236	-9.396	8.303e-05	No
1 bar N_2, 1000 ppm CH_4	4.237	-19.620	-10.781	2.079e-05	No
10 bar N_2, 1000 ppm CH_4	4.433	-20.244	-11.404	1.115e-05	No
100 bar N_2, 1000 ppm CH_4	4.521	-20.484	-11.645	8.765e-06	No

Table 13: GJ 367b: N_2 atmospheric models with 1 ppm trace gases.

Atmosphere	Reduced χ^2	$\ln Z$	$\Delta \ln Z$	Bayes Factor	Consistent?
0.01 bar N_2, 1 ppm CO_2	2.096	-10.596	-1.756	1.727e-01	Yes
0.1 bar N_2, 1 ppm CO_2	2.103	-10.607	-1.768	1.707e-01	Yes
1 bar N_2, 1 ppm CO_2	2.113	-10.657	-1.818	1.624e-01	Yes
10 bar N_2, 1 ppm CO_2	3.087	-13.435	-4.596	1.010e-02	No
100 bar N_2, 1 ppm CO_2	2.302	-11.201	-2.362	9.422e-02	Yes
0.01 bar N_2, 1 ppm H_2O	2.130	-10.597	-1.758	1.724e-01	Yes
0.1 bar N_2, 1 ppm H_2O	2.073	-10.482	-1.642	1.935e-01	Yes
1 bar N_2, 1 ppm H_2O	2.045	-10.469	-1.629	1.961e-01	Yes
10 bar N_2, 1 ppm H_2O	3.415	-16.742	-7.902	3.699e-04	No
100 bar N_2, 1 ppm H_2O	4.740	-20.883	-12.043	5.883e-06	No
0.01 bar N_2, 1 ppm SO_2	2.105	-10.683	-1.844	1.582e-01	Yes
0.1 bar N_2, 1 ppm SO_2	2.248	-11.455	-2.616	7.309e-02	Yes
1 bar N_2, 1 ppm SO_2	3.188	-16.133	-7.293	6.800e-04	No
10 bar N_2, 1 ppm SO_2	3.286	-13.943	-5.104	6.075e-03	No
100 bar N_2, 1 ppm SO_2	2.591	-11.473	-2.633	7.183e-02	Yes
0.01 bar N_2, 1 ppm CH_4	2.021	-10.342	-1.502	2.226e-01	Yes
0.1 bar N_2, 1 ppm CH_4	2.065	-10.474	-1.634	1.951e-01	Yes
1 bar N_2, 1 ppm CH_4	2.156	-10.997	-2.158	1.155e-01	Yes
10 bar N_2, 1 ppm CH_4	3.270	-16.420	-7.581	5.102e-04	No
100 bar N_2, 1 ppm CH_4	4.723	-21.858	-13.018	2.219e-06	No

A.3 TRAPPIST-1b

A.3.1 Surfaces

Table 14 shows the Bayesian model comparison summary for TRAPPIST-1b surface models.

Surface	Reduced χ^2	$\ln Z$	$\Delta \ln Z$	Bayes factor	Consistent?
Martian breccia	**1.19**	**-0.66**	**0.0**	**1.0**	**Yes**
Basalt tuff	1.38	-0.76	-0.10	0.909	Yes
Basalt glass	1.49	-0.82	-0.16	0.856	Yes
Lherzolite	1.50	-0.81	-0.15	0.860	Yes
Gabbro	1.46	-0.81	-0.14	0.867	Yes
Hematite	1.56	-0.85	-0.19	0.829	Yes
Phonolite	1.70	-0.92	-0.25	0.777	Yes
Tephrite	1.77	-0.96	-0.29	0.747	Yes
Tholeiitic basalt	1.85	-0.98	-0.31	0.732	Yes
Martian basaltics hergottite	1.83	-0.97	-0.31	0.733	Yes
Pyrite	2.37	-1.14	-0.48	0.619	Yes
Granite	2.30	-1.16	-0.50	0.609	Yes
Andesite	2.35	-1.21	-0.55	0.580	Yes
Basalt (large grain)	2.46	-1.25	-0.59	0.556	Yes
Norite	2.56	-1.27	-0.61	0.543	Yes
Harzburgite	2.73	-1.31	-0.64	0.526	Yes
Diorite	3.10	-1.53	-0.87	0.421	Yes
Trachybasalt	3.25	-1.59	-0.92	0.397	Yes
Lunar mare basalt	3.41	-1.60	-0.94	0.390	Yes
Rhyolite	4.69	-2.21	-1.55	0.213	Yes
Basalt (small grain)	5.51	-2.60	-1.94	0.144	Yes
Trachyte	7.54	-3.31	-2.65	0.071	Yes
Lunar anorthosite	13.69	-6.46	-5.80	0.003	No
Magnesium sulfate	19.65	-9.42	-8.76	0.00016	No
Albite dust	34.39	-16.78	-16.11	1.00e-07	No

Table 14: Bayesian model comparison of bare-rock surfaces for TRAPPIST-1b. The best performing surface, Martian breccia, is used as a reference model. A model is considered consistent with the data when Δ ln Z $>$ -3. Data: `https://github.com/stuitje/VAYU/tree/main/out/trappist-1b/bayes_model_comparison_surface.csv`.

A.3.2 Atmospheres

Table 15 shows the Bayesian model comparison summary for TRAPPIST-1b pure atmosphere models. Tables 16 and 17 show the model comparison for N_2-based atmospheres with 1000 ppm and 1 ppm trace gases, respectively.

Atmosphere	Reduced χ^2	$\ln Z$	$\Delta \ln Z$	Bayes factor	Consistent?
0.01 bar CH_4	3.58	-1.75	-1.08	0.341	Yes
0.1 bar CH_4	2.88	-1.38	-0.71	4.92e-01	Yes
1 bar CH_4	6.94	-3.20	-2.53	8.00e-02	Yes
10 bar CH_4	11.45	-5.43	-4.75	8.61e-03	No
100 bar CH_4	21.10	-10.08	-9.41	8.22e-05	No
0.01 bar H_2O	14.69	-6.18	-5.51	4.06e-03	No
0.1 bar H_2O	11.53	-5.03	-4.36	1.28e-02	No
1 bar H_2O	11.23	-5.03	-4.35	1.28e-02	No
10 bar H_2O	11.20	-4.95	-4.28	1.38e-02	No
100 bar H_2O	11.23	-5.07	-4.40	1.23e-02	No
0.01 bar CO_2	16.59	-8.18	-7.51	5.49e-04	No
0.1 bar CO_2	22.65	-10.92	-10.25	3.53e-05	No
1 bar CO_2	95.33	-47.65	-46.98	3.94e-21	No
10 bar CO_2	23.48	-11.37	-10.70	2.25e-05	No
100 bar CO_2	23.46	-11.38	-10.71	2.23e-05	No
0.01 bar SO_2	38.11	-16.77	-16.10	1.02e-07	No
0.1 bar SO_2	56.36	-24.92	-24.25	2.95e-11	No
1 bar SO_2	34.02	-16.59	-15.92	1.22e-07	No
10 bar SO_2	26.77	-13.43	-12.76	2.87e-06	No
100 bar SO_2	25.48	-12.79	-12.12	5.43e-06	No

Table 15: Bayesian model comparison for all pure atmospheric models of TRAPPIST-1b, showing the log-evidence (ln Z), difference in log evidence with respect to the surface Martian breccia (Δ ln Z) and the Bayes factor with respect to Martian breccia. Models with Δ ln Z > -3, corresponding to a Bayes factor of 0.05, are considered consistent with the data. The best performing model has been made bold. The reduced chi-squared value is also shown. All atmosphere data: `https://github.com/stuitje/VAYU/tree/main/out/trappist-1b/bayes_model_comparison_atmo.csv`.

Table 16: TRAPPIST-1b: N_2 atmospheric models with 1000 ppm trace gases.

Atmosphere	Reduced χ^2	$\ln Z$	$\Delta \ln Z$	Bayes factor	Consistent?
100 bar N_2, 1000 ppm CH_4	**1.42**	**-0.79**	**-0.12**	**0.891**	**Yes**
100 bar N_2, 1000 ppm H_2O	6.05	-3.04	-2.37	9.33e-02	Yes
10 bar N_2, 1000 ppm H_2O	6.44	-3.20	-2.53	8.00e-02	Yes
0.01 bar N_2, 1000 ppm CO_2	7.95	-3.73	-3.06	4.70e-02	No
0.01 bar N_2, 1000 ppm H_2O	9.31	-3.94	-3.27	3.80e-02	No
0.01 bar N_2, 1000 ppm CH_4	9.29	-3.99	-3.32	3.62e-02	No
0.01 bar N_2, 1000 ppm SO_2	14.68	-6.00	-5.33	4.83e-03	No
1 bar N_2, 1000 ppm CH_4	14.19	-5.92	-5.25	5.23e-03	No
0.1 bar N_2, 1000 ppm H_2O	12.09	-5.16	-4.49	1.12e-02	No
0.01 bar N_2, 1000 ppm CH_4	11.20	-4.68	-4.01	1.81e-02	No
0.1 bar N_2, 1000 ppm CH_4	11.20	-4.68	-4.01	1.81e-02	No
0.1 bar N_2, 1000 ppm CO_2	28.30	-14.20	-13.53	1.33e-06	No
1 bar N_2, 1000 ppm CO_2	31.44	-15.49	-14.82	3.66e-07	No
1 bar N_2, 1000 ppm SO_2	34.10	-15.46	-14.79	3.77e-07	No
10 bar N_2, 1000 ppm CO_2	37.72	-18.44	-17.77	1.92e-08	No
100 bar N_2, 1000 ppm CO_2	39.08	-19.16	-18.49	9.34e-09	No
10 bar N_2, 1000 ppm SO_2	74.62	-32.40	-31.73	1.65e-14	No
100 bar N_2, 1000 ppm SO_2	48.73	-23.44	-22.77	1.30e-10	No

Table 17: TRAPPIST-1b: N_2 atmospheric models with 1 ppm trace gases.

Atmosphere	Reduced χ^2	$\ln Z$	$\Delta \ln Z$	Bayes factor	Consistent?
1 bar N_2, 1 ppm CO_2	**14.78**	**-7.43**	**-6.75**	**1.17e-03**	**No**
1 bar N_2, 1 ppm SO_2	22.01	-8.60	-7.93	3.59e-04	No
0.1 bar N_2, 1 ppm SO_2	39.27	-14.28	-13.61	1.22e-06	No
10 bar N_2, 1 ppm CO_2	57.20	-20.83	-20.16	1.75e-09	No
0.1 bar N_2, 1 ppm CO_2	61.94	-21.10	-20.43	1.34e-09	No
0.01 bar N_2, 1 ppm CO_2	617.97	-134.21	-133.54	1.01e-58	No
100 bar N_2, 1 ppm CO_2	314.33	-97.29	-96.62	1.10e-42	No
0.01 bar N_2, 1 ppm H_2O	1444.56	-266.18	-265.51	4.90e-116	No
0.1 bar N_2, 1 ppm H_2O	1076.59	-340.36	-339.69	2.98e-148	No
1 bar N_2, 1 ppm H_2O	1059.32	-269.39	-268.72	1.99e-117	No
10 bar N_2, 1 ppm H_2O	1019.59	-184.67	-184.00	1.22e-80	No
100 bar N_2, 1 ppm H_2O	1176.77	-316.68	-316.01	5.72e-138	No
0.01 bar N_2, 1 ppm SO_2	1459.57	-315.03	-314.36	2.99e-137	No
10 bar N_2, 1 ppm SO_2	304.44	-83.68	-83.01	8.87e-37	No
100 bar N_2, 1 ppm SO_2	1752.06	-167.91	-167.24	2.34e-73	No
0.01 bar N_2, 1 ppm CH_4	1617.77	-368.32	-367.65	2.15e-160	No
0.1 bar N_2, 1 ppm CH_4	276.89	-78.12	-77.45	2.32e-34	No
1 bar N_2, 1 ppm CH_4	408.69	-84.31	-83.64	4.72e-37	No
10 bar N_2, 1 ppm CH_4	344.86	-76.06	-75.39	1.82e-33	No
100 bar N_2, 1 ppm CH_4	1101.95	-199.92	-199.24	2.95e-87	No

A.4 TRAPPIST-1c

A.4.1 Surfaces

Table 18 shows the Bayesian model comparison summary for TRAPPIST-1c surface models.

Surface	$\ln Z$	$\Delta \ln Z$	Bayes factor	Consistent?
Granite	**-0.032**	**0.00**	**1.0**	**Yes**
Gabbro	-0.041	-0.009	0.991	Yes
Basalt glass	-0.050	-0.018	0.982	Yes
Harzburgite	-0.048	-0.017	0.984	Yes
Basalt tuff	-0.065	-0.033	0.968	Yes
Diorite	-0.073	-0.041	0.959	Yes
Lherzolite	-0.054	-0.022	0.978	Yes
Hematite	-0.145	-0.113	0.893	Yes
Phonolite	-0.165	-0.134	0.875	Yes
Tephrite	-0.164	-0.133	0.876	Yes
Rhyolite	-0.197	-0.165	0.848	Yes
Martian basaltic shergottite	-0.186	-0.154	0.857	Yes
Martian breccia	-0.240	-0.208	0.812	Yes
Basalt small grain	-0.296	-0.264	0.768	Yes
Basalt large grain	-0.378	-0.346	0.707	Yes
Norite	-0.476	-0.444	0.641	Yes
Andesite	-0.477	-0.445	0.641	Yes
Trachy basalt	-0.517	-0.485	0.615	Yes
Tholeiitic basalt	-0.559	-0.527	0.591	Yes
Lunar mare basalt	-0.672	-0.640	0.527	Yes
Pyrite	-0.752	-0.720	0.487	Yes
Lunar anorthosite	-1.076	-1.044	0.352	Yes
Magnesium sulfate	-1.638	-1.606	0.201	Yes
Trachyte	-1.323	-1.291	0.275	Yes
Albite dust	-3.234	-3.202	0.041	No

Table 18: Bayesian model comparison of bare-rock surfaces for TRAPPIST-1c. The best performing surface, granite, is used as a reference model. A model is considered consistent with the data when $\Delta \ln Z > -3$. Data: `https://github.com/stuitje/VAYU/tree/main/out/trappist-1c/bayes_model_comparison_surface.csv`.

A.4.2 Atmospheres

Table 19 shows the Bayesian model comparison summary for TRAPPIST-1c pure atmosphere models. Tables 20 and 21 show the model comparison for N_2-based atmospheres with 1000 ppm and 1 ppm trace gases, respectively.

Atmosphere	$\ln Z$	$\Delta \ln Z$	Bayes factor	Consistent?
0.01 bar CO_2	-1.96	-1.93	0.145	Yes
0.1 bar CO_2	-2.87	-2.84	5.85e-02	Yes
1 bar CO_2	-2.92	-2.88	5.59e-02	Yes
10 bar CO_2	-2.99	-2.96	5.18e-02	Yes
100 bar CO_2	-2.98	-2.95	5.26e-02	Yes
0.01 bar H_2O	-1.76	-1.73	0.177	Yes
0.1 bar H_2O	-0.75	-0.72	0.488	Yes
1 bar H_2O	-0.72	-0.69	0.504	Yes
10 bar H_2O	-0.74	-0.70	0.495	Yes
100 bar H_2O	-0.72	-0.69	0.502	Yes
0.01 bar SO_2	-0.66	-0.63	0.532	Yes
0.1 bar SO_2	**-0.06**	**-0.02**	**0.976**	**Yes**
1 bar SO_2	-0.60	-0.57	0.565	Yes
10 bar SO_2	-1.52	-1.48	0.227	Yes
100 bar SO_2	-1.83	-1.80	0.166	Yes
0.01 bar CH_4	-0.26	-0.22	0.800	Yes
0.1 bar CH_4	-0.40	-0.37	0.692	Yes
1 bar CH_4	-1.59	-1.55	0.211	Yes
10 bar CH_4	-2.39	-2.36	9.46e-02	Yes
100 bar CH_4	-3.58	-3.55	2.88e-02	No

Table 19: Bayesian model comparison for all pure atmospheric models of TRAPPIST-1c, showing the log-evidence (ln Z), difference in log evidence with respect to the surface granite (Δ ln Z) and the Bayes factor with respect to granite. Models with Δ ln Z > -3, corresponding to a Bayes factor of 0.05, are considered consistent with the data. The best performing model has been made bold. The reduced chi-squared value is also shown. All atmosphere data: `https://github.com/stuitje/VAYU/tree/main/out/trappist-1c/bayes_model_comparison_atmo.csv`.

Table 20: Bayesian model comparison for N_2 + 1000 ppm trace gas atmospheric models of TRAPPIST-1c. Models with $\Delta \ln Z > -3$, corresponding to a Bayes factor > 0.05, are considered consistent with the data.

Atmosphere	$\ln Z$	$\Delta \ln Z$	Bayes factor	Consistent?
0.01 bar N_2 + 1000 ppm CO_2	-0.22	-0.18	0.832	Yes
0.1 bar N_2 + 1000 ppm CO_2	-2.32	-2.29	0.101	Yes
1 bar N_2 + 1000 ppm CO_2	-4.22	-4.18	1.52e-02	No
10 bar N_2 + 1000 ppm CO_2	-4.64	-4.60	1.00e-02	No
100 bar N_2 + 1000 ppm CO_2	-4.71	-4.67	9.35e-03	No
0.01 bar N_2 + 1000 ppm H_2O	-1.61	-1.57	0.207	Yes
0.1 bar N_2 + 1000 ppm H_2O	-1.99	-1.95	0.142	Yes
1 bar N_2 + 1000 ppm H_2O	-1.59	-1.56	0.210	Yes
10 bar N_2 + 1000 ppm H_2O	-0.27	-0.24	0.788	Yes
100 bar N_2 + 1000 ppm H_2O	-0.22	-0.18	0.833	Yes
0.01 bar N_2 + 1000 ppm SO_2	-2.43	-2.39	9.14e-02	Yes
0.1 bar N_2 + 1000 ppm SO_2	-3.75	-3.72	2.43e-02	No
1 bar N_2 + 1000 ppm SO_2	-0.31	-0.28	0.756	Yes
10 bar N_2 + 1000 ppm SO_2	-0.27	-0.24	0.788	Yes
100 bar N_2 + 1000 ppm SO_2	-1.44	-1.40	0.246	Yes
0.01 bar N_2 + 1000 ppm CH_4	-1.56	-1.53	0.217	Yes
0.1 bar N_2 + 1000 ppm CH_4	-1.73	-1.69	0.184	Yes
1 bar N_2 + 1000 ppm CH_4	-1.65	-1.62	0.198	Yes
10 bar N_2 + 1000 ppm CH_4	-1.62	-1.59	0.204	Yes
100 bar N_2 + 1000 ppm CH_4	-0.02	0.01	1.01	Yes

Table 21: Bayesian model comparison for N_2 + 1 ppm trace gas atmospheric models of TRAPPIST-1c. Models with $\Delta \ln Z > -3$, corresponding to a Bayes factor > 0.05, are considered consistent with the data.

Atmosphere	$\ln Z$	$\Delta \ln Z$	Bayes factor	Consistent?
0.01 bar N_2 + 1 ppm CO_2	-43.79	-43.76	9.92e-20	No
0.1 bar N_2 + 1 ppm CO_2	-26.09	-26.05	4.84e-12	No
1 bar N_2 + 1 ppm CO_2	-0.02	0.01	1.01	Yes
10 bar N_2 + 1 ppm CO_2	-24.01	-23.98	3.86e-11	No
100 bar N_2 + 1 ppm CO_2	-17.03	-17.00	4.14e-08	No
0.01 bar N_2 + 1 ppm H_2O	-112.82	-112.79	1.04e-49	No
0.1 bar N_2 + 1 ppm H_2O	-128.07	-128.04	2.48e-56	No
1 bar N_2 + 1 ppm H_2O	-13.20	-13.16	1.92e-06	No
10 bar N_2 + 1 ppm H_2O	-135.61	-135.58	1.31e-59	No
100 bar N_2 + 1 ppm H_2O	-116.19	-116.16	3.57e-51	No
0.01 bar N_2 + 1 ppm SO_2	-47.30	-47.26	2.98e-21	No
0.1 bar N_2 + 1 ppm SO_2	-12.56	-12.52	3.64e-06	No
1 bar N_2 + 1 ppm SO_2	-6.48	-6.45	1.58e-03	No
10 bar N_2 + 1 ppm SO_2	-2.92	-2.89	5.56e-02	Yes
100 bar N_2 + 1 ppm SO_2	-3.61	-3.58	2.80e-02	No
0.01 bar N_2 + 1 ppm CH_4	-73.48	-73.44	1.27e-32	No
0.1 bar N_2 + 1 ppm CH_4	-167.50	-167.47	1.86e-73	No
1 bar N_2 + 1 ppm CH_4	-94.69	-94.66	7.77e-42	No
10 bar N_2 + 1 ppm CH_4	-122.88	-122.85	4.45e-54	No
100 bar N_2 + 1 ppm CH_4	-48.75	-48.72	6.97e-22	No

B JWST imaging emission: TRAPPIST-1b and 1c

As TRAPPIST-1b and TRAPPIST-1c have already been observed with MIRI imaging, simulations of emissions in the MIRI filters F1500W and F1280W would be only useful for surface or atmosphere characterisation of these planets. The surface emission results have been shown in Figure 52. For TRAPPIST-1b, we see that indeed, the surfaces Martian breccia, lherzolite, and gabbro fit best. Nevertheless, the difference between two filters is much larger in the data than in simulations, as was also found in Section 4.3.1. For TRAPPIST-1c, granite's emission in around 15 μm is slightly too low to match observations. Instead, gabbro and lherzolite perform better. This slightly differs from what was found in 4.4.1.

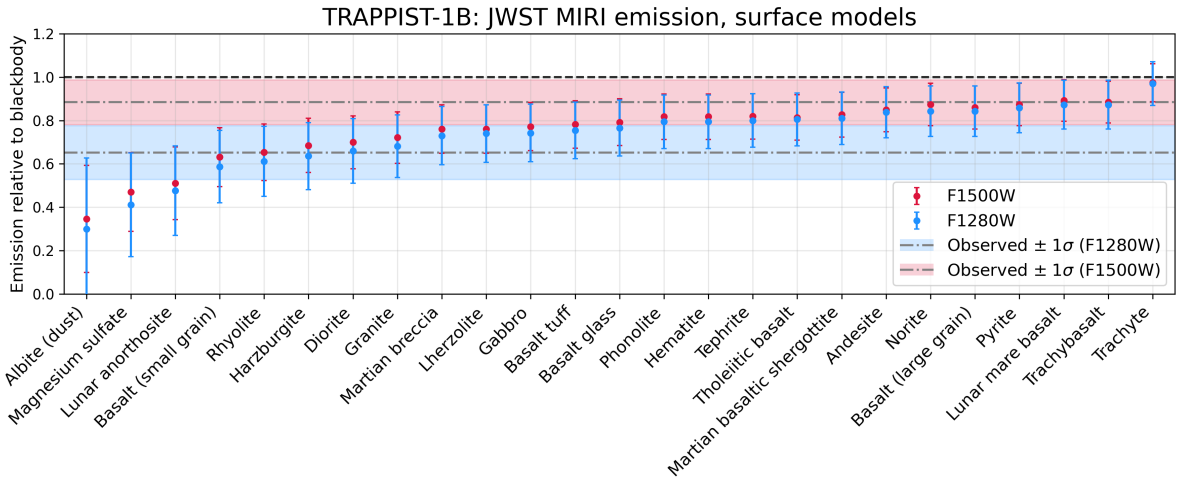

(a) TRAPPIST-1b surface emissions. Data by Ducrot et al. [2025].

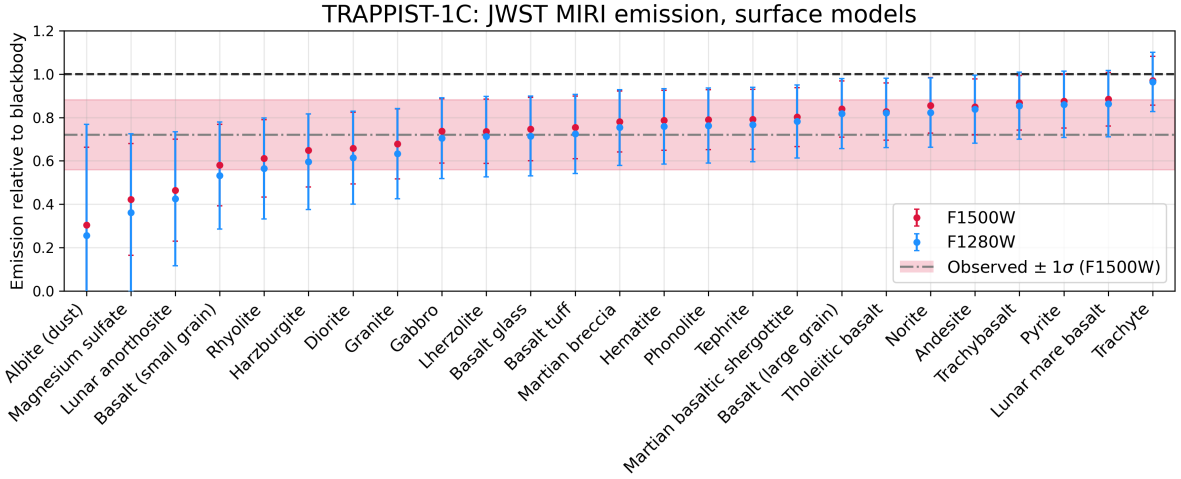

(b) TRAPPIST-1c surface emissions. Data by Zieba et al. [2023].

Figure 52: Simulated emissions in the JWST MIRI F1500W and F1280W filters for planets TRAPPIST-1b and 1c, together with the data gathered in F1500W by Zieba et al. [2023] and the data gathered in F1500W and F1280W by Ducrot et al. [2025].

References

Eric Agol, Caroline Dorn, Simon L Grimm, Martin Turbet, Elsa Ducrot, Laetitia Delrez, Michaël Gillon, Brice-Olivier Demory, Artem Burdanov, Khalid Barkaoui, et al. Refining the transit-timing and photometric analysis of TRAPPIST-1: masses, radii, densities, dynamics, and ephemerides. *The planetary science journal*, 2(1):1, 2021.

Eleonora Alei, Björn S Konrad, Daniel Angerhausen, John Lee Grenfell, Paul Mollière, Sascha P Quanz, Sarah Rugheimer, and Fabian Wunderlich. Large interferometer for exoplanets (life)-v. diagnostic potential of a mid-infrared space interferometer for studying earth analogs. *Astronomy & Astrophysics*, 665:A106, 2022.

LY Aranovich, ES Persikov, PG Bukhtiyarov, AN Koshlyakova, and NM Lebedeva. Origin of the earth's first felsic crust: A hydrogen perspective? *Petrology*, 33(1):62–71, 2025.

Thomas Barclay, Kyle B Sheppard, Natasha Latouf, Avi M Mandell, Elisa V Quintana, Emily A Gilbert, Giuliano Liuzzi, Geronimo L Villanueva, Giada Arney, Jonathan Brande, et al. The transmission spectrum of the potentially rocky planet l 98-59 c. *The Astronomical Journal*, 169(5):241, 2025.

Justine Bernadet, Anastassia Y Borisova, Martin Guitreau, Oleg G Safonov, Paul Asimow, Anne Nédélec, Wendy A Bohrson, Svetlana A Kosova, and Philippe de Parseval. Making continental crust on water-bearing terrestrial planets. *Science Advances*, 11(13):eads6746, 2025.

Karalee Brugman, MG Phillips, and CB Till. Experimental determination of mantle solidi and melt compositions for two likely rocky exoplanet compositions. *Journal of Geophysical Research: Planets*, 126(7):e2020JE006731, 2021.

Remo Burn, Christoph Mordasini, Lokesh Mishra, Jonas Haldemann, Julia Venturini, Alexandre Emsenhuber, and Thomas Henning. A radius valley between migrated steam worlds and evaporated rocky cores. *Nature astronomy*, 8(4):463–471, 2024.

JA Caballero, E González-Álvarez, M Brady, T Trifonov, TG Ellis, C Dorn, C Cifuentes, K Molaverdikhani, JL Bean, T Boyajian, et al. A detailed analysis of the Gl 486 planetary system. *Astronomy & Astrophysics*, 665:A120, 2022.

Philip R Christensen and Steven W Ruff. Formation of the hematite-bearing unit in meridiani planum: Evidence for deposition in standing water. *Journal of Geophysical Research: Planets*, 109(E8), 2004.

Nicolas B. Cowan and Eric Agol. The Statistics of Albedo and Heat Recirculation on Hot Exoplanets. *The Astrophysical Journal*, 729:54, 2011.

Ian J. M. Crossfield, Matej Malik, Michelle L. Hill, Stephen R. Kane, Bradford Foley, Alex S. Polanski, David Coria, Jonathan Brande, Yanzhe Zhang, Katherine Wienke, Laura Kreidberg, Nicolas B. Cowan, Diana Dragomir, Varoujan Gorjian, Thomas Mikal-Evans, Björn Benneke, Jessie L. Christiansen, Drake Deming, and Farisa Y. Morales. Gj 1252b: A hot terrestrial super-earth with no atmosphere. *The Astrophysical Journal Letters*, 937(1):L17, September 2022. doi: 10.3847/2041-8213/ac886b.

H Diamond-Lowe, GW King, A Youngblood, A Brown, WS Howard, JG Winters, DJ Wilson, K France, JM Mendonça, LA Buchhave, et al. High-energy spectra of LTT 1445A and GJ 486 reveal flares and activity. *Astronomy & Astrophysics*, 689:A48, 2024.

Hannah Diamond-Lowe, David Charbonneau, Matej Malik, Eliza M-R Kempton, and Yuri Beletsky. Optical transmission spectroscopy of the terrestrial exoplanet lhs 3844b from 13 ground-based transit observations. *The Astronomical Journal*, 160(4):188, 2020.

Dan Dicken, Macarena García Marín, Irene Shivaei, Pierre Guillard, Mattia Libralato, Alistair Glasse, Karl D Gordon, Christophe Cossou, Patrick Kavanagh, Tea Temim, et al. JWST MIRI flight performance: Imaging. *Astronomy & Astrophysics*, 689:A5, 2024.

Laura N.R. do Amaral, Rory Barnes, Antígona Segura, and Rodrigo Luger. The contribution of M-dwarf flares to the thermal escape of potentially habitable planet atmospheres. *The Astrophysical Journal*, 928(1):12, 2022.

Elsa Ducrot, Michaël Gillon, Laetitia Delrez, E Agol, P Rimmer, M Turbet, MN Günther, B-O Demory, AHMJ Triaud, E Bolmont, et al. TRAPPIST-1: global results of the spitzer exploration science program red worlds. *Astronomy & Astrophysics*, 640:A112, 2020.

Elsa Ducrot, Pierre-Olivier Lagage, Michiel Min, Michaël Gillon, Taylor J Bell, Pascal Tremblin, Thomas Greene, Achrène Dyrek, Jeroen Bouwman, Rens Waters, et al. Combined analysis of the 12.8 and 15 μm JWST/MIRI eclipse observations of TRAPPIST-1 b. *Nature Astronomy*, 9(3):358–369, 2025.

Steven Earle. *Physical geology*. BCcampus, 2015.

J. M. Edwards and A. Slingo. Studies with a flexible new radiation code. i: Choosing a configuration for a large-scale model. *Quarterly Journal of the Royal Meteorological Society*, 122(531):689–719, 1996. doi: https://doi.org/10.1002/qj.49712253107.

European Space Agency. Webb, 2023. URL `https://www.esa.int/Science_Exploration/Space_Science/Webb`. Accessed: July 7, 2025.

Chris Evans. The rocky worlds director's discretionary time programme, Jun 2025. URL `https://esahubble.org/forscientists/announcements/sci25003/?lang`.

Thomas J Fauchez, Benjamin V Rackham, Elsa Ducrot, Kevin B Stevenson, and Julien de Wit. Stellar models also limit exoplanet atmosphere studies in emission. *arXiv preprint arXiv:2502.19585*, 2025.

Bradford J Foley. Exoplanet geology: What can we learn from current and future observations? *Reviews in Mineralogy and Geochemistry*, 90(1):559–594, 2024.

Kevin France, Girish Duvvuri, Hilary Egan, Tommi Koskinen, David J Wilson, Allison Youngblood, Cynthia S Froning, Alexander Brown, Julián D Alvarado-Gómez, Zachory K Berta-Thompson, et al. The high-energy radiation environment around a 10 Gyr M dwarf: habitable at last? *The Astronomical Journal*, 160(5):237, 2020.

Peter Gao, Hannah R Wakeford, Sarah E Moran, and Vivien Parmentier. Aerosols in exoplanet atmospheres, 2021.

LJ Garcia, SE Moran, BV Rackham, HR Wakeford, Michaël Gillon, Julien de Wit, and NK Lewis. Hst/wfc3 transmission spectroscopy of the cold rocky planet TRAPPIST-1h. *Astronomy & Astrophysics*, 665:A19, 2022.

Megan T Gialluca, Rory Barnes, Victoria S Meadows, Rodolfo Garcia, Jessica Birky, and Eric Agol. The implications of thermal hydrodynamic atmospheric escape on the TRAPPIST-1 planets. *The Planetary Science Journal*, 5(6):137, 2024.

Michaël Gillon, Emmanuël Jehin, Susan M Lederer, Laetitia Delrez, Julien de Wit, Artem Burdanov, Valérie Van Grootel, Adam J Burgasser, Amaury HMJ Triaud, Cyrielle Opitom, et al. Temperate Earth-sized planets transiting a nearby ultracool dwarf star. *Nature*, 533 (7602):221–224, 2016.

Elisa Goffo, Davide Gandolfi, Jo Ann Egger, Alexander J Mustill, Simon H Albrecht, Teruyuki Hirano, Oleg Kochukhov, Nicola Astudillo-Defru, Oscar Barragan, Luisa M Serrano, et al. Company for the ultra-high density, ultra-short period sub-earth GJ 367 b: Discovery of two additional low-mass planets at 11.5 and 34 days. *The Astrophysical Journal Letters*, 955 (1):L3, 2023.

Thomas P Greene, Taylor J Bell, Elsa Ducrot, Achrène Dyrek, Pierre-Olivier Lagage, and Jonathan J Fortney. Thermal emission from the earth-sized exoplanet TRAPPIST-1 b using JWST. *Nature*, 618(7963):39–42, 2023.

Simon L. Grimm, Brice-Olivier Demory, Michaël Gillon, Caroline Dorn, Eric Agol, Artem Burdanov, Laetitia Delrez, Marko Sestovic, Amaury H. M. J. Triaud, Martin Turbet, Émeline Bolmont, Anthony Caldas, et al. The nature of the TRAPPIST-1 exoplanets. *Astronomy Astrophysics*, 613:A68, May 2018. ISSN 1432-0746. doi: 10.1051/0004-6361/201732233.

Simon L Grimm, Matej Malik, Daniel Kitzmann, Andrea Guzmán-Mesa, H Jens Hoeijmakers, Chloe Fisher, João M Mendonça, Sergey N Yurchenko, Jonathan Tennyson, Fabien Alesina, et al. HELIOS-K 2.0 opacity calculator and open-source opacity database for exoplanetary atmospheres. *The Astrophysical Journal Supplement Series*, 253(1):30, 2021.

Mark Hammond, Claire Marie Guimond, Tim Lichtenberg, Harrison Nicholls, Chloe Fisher, Rafael Luque, Tobias G Meier, Jake Taylor, Quentin Changeat, Lisa Dang, et al. Reliable detections of atmospheres on rocky exoplanets with photometric JWST phase curves. *The Astrophysical Journal Letters*, 978(2):L40, 2025.

Oliver Herbort and Leon Sereinig. The atmospheres of rocky exoplanets-III. using atmospheric spectra to constrain surface rock composition. *Astronomy & Astrophysics*, 699:A67, 2025.

Oliver Herbort, Peter Woitke, Ch Helling, and Aubrey Zerkle. The atmospheres of rocky exoplanets-i. outgassing of common rock and the stability of liquid water. *Astronomy & Astrophysics*, 636:A71, 2020.

Renyu Hu, Bethany L. Ehlmann, and Sara Seager. Theoretical spectra of terrestrial exoplanet surfaces. *The Astrophysical Journal*, 752(1):7, May 2012. ISSN 1538-4357. doi: 10.1088/0004-637x/752/1/7.

Renyu Hu, Sara Seager, and William Bains. Photochemistry in terrestrial exoplanet atmospheres. II. h2s and so2photochemistry in anoxic atmospheres. *The Astrophysical Journal*, 769(1):6, April 2013. ISSN 1538-4357. doi: 10.1088/0004-637x/769/1/6.

Jingcheng Huang, Sara Seager, Janusz J Petkowski, Sukrit Ranjan, and Zhuchang Zhan. Assessment of ammonia as a biosignature gas in exoplanet atmospheres. *Astrobiology*, 22 (2):171–191, 2022.

Emmy B Hughes, James Wray, Suniti Karunatillake, Grace Fanson, Elise Harrington, and Don R Hood. Water-limited hydrothermalism and volcanic resurfacing of eridania basin, mars. *Journal of Geophysical Research: Planets*, 129(7):e2024JE008461, 2024.

Husser, T.O., Wende-von Berg, S., Dreizler, S., Homeier, D., Reiners, A., Barman, T., and Hauschildt, P. H. A new extensive library of phoenix stellar atmospheres and synthetic spectra. *AA*, 553:A6, 2013. doi: 10.1051/0004-6361/201219058. URL https://doi.org/10.1051/0004-6361/201219058.

Brian M Hynek, Raymond E Arvidson, and Roger J Phillips. Geologic setting and origin of terra meridiani hematite deposit on mars. *Journal of Geophysical Research: Planets*, 107 (E10):18–1, 2002.

Jegug Ih, Eliza M-R Kempton, Emily A Whittaker, and Madeline Lessard. Constraining the thickness of TRAPPIST-1 b's atmosphere from its JWST secondary eclipse observation at 15 μm. *The Astrophysical Journal Letters*, 952(1):L4, 2023.

Aishwarya R Iyer, Michael R Line, Philip S Muirhead, Jonathan J Fortney, and Ehsan Gharib-Nezhad. The SPHINX M-dwarf spectral grid. I. Benchmarking new model atmospheres to derive fundamental M-dwarf properties. *The Astrophysical Journal*, 944(1):41, 2023.

LJ Janssen, Peter Woitke, Oliver Herbort, Michiel Min, Katy L Chubb, Ch Helling, and Ludmila Carone. The sulfur species in hot rocky exoplanet atmospheres. *Astronomische Nachrichten*, 344(10):e20230075, 2023.

Colin P Johnstone. Hydrodynamic escape of water vapor atmospheres near very active stars. *The Astrophysical Journal*, 890(1):79, 2020.

Sean Jordan, Paul B Rimmer, Oliver Shorttle, and Tereza Constantinou. Photochemistry of venus-like planets orbiting k-and M-dwarf stars. *The Astrophysical Journal*, 922(1):44, 2021.

Eliza M-R Kempton, Michael Zhang, Jacob L Bean, Maria E Steinrueck, Anjali AA Piette, Vivien Parmentier, Isaac Malsky, Michael T Roman, Emily Rauscher, Peter Gao, et al. A reflective, metal-rich atmosphere for gj 1214b from its JWST phase curve. *Nature*, 620 (7972):67–71, 2023.

Edwin S Kite and Megan N Barnett. Exoplanet secondary atmosphere loss and revival. *Proceedings of the National Academy of Sciences*, 117(31):18264–18271, 2020.

Edwin S Kite and Laura Schaefer. Water on hot rocky exoplanets. *The Astrophysical Journal Letters*, 909(2):L22, 2021.

Daniel DB Koll. A scaling for atmospheric heat redistribution on tidally locked rocky planets. *The Astrophysical Journal*, 924(2):134, 2022.

Quentin Kral, Jeanne Davoult, and Benjamin Charnay. Formation of secondary atmospheres on terrestrial planets by late disk accretion. *Nature Astronomy*, 4(8):769–775, 2020.

Quentin Kral, Paul Huet, Camille Bergez-Casalou, Philippe Thébault, Sébastien Charnoz, and Sonia Fornasier. An impact-free mechanism to deliver water to terrestrial planets and exoplanets. *Astronomy & Astrophysics*, 692:A70, 2024.

Laura Kreidberg. Exoplanet atmosphere measurements from transmission spectroscopy and other planet star combined light observations. In *Handbook of exoplanets*, pages 2083–2105. Springer, 2018.

Laura Kreidberg, Daniel D. B. Koll, Caroline Morley, Renyu Hu, Laura Schaefer, Drake Deming, Kevin B. Stevenson, Jason Dittmann, Andrew Vanderburg, David Berardo, Xueying Guo, Keivan Stassun, Ian Crossfield, David Charbonneau, David W. Latham, Abraham Loeb, George Ricker, Sara Seager, and Roland Vanderspek. Absence of a thick atmosphere on the terrestrial exoplanet LHS 3844b. *Nature*, 573(7772):87–90, August 2019. doi: 10.1038/s41586-019-1497-4.

Joshua Krissansen-Totton and Jonathan J Fortney. Predictions for observable atmospheres of TRAPPIST-1 planets from a fully coupled atmosphere–interior evolution model. *The Astrophysical Journal*, 933(1):115, 2022.

Joshua Krissansen-Totton, Nicholas Wogan, Maggie Thompson, and Jonathan J Fortney. The erosion of large primary atmospheres typically leaves behind substantial secondary atmospheres on temperate rocky planets. *Nature communications*, 15(1):8374, 2024.

Kristine WF Lam, Szilárd Csizmadia, Nicola Astudillo-Defru, Xavier Bonfils, Davide Gandolfi, Sebastiano Padovan, Massimiliano Esposito, Coel Hellier, Teruyuki Hirano, John Livingston, et al. GJ 367b: A dense, ultrashort-period sub-earth planet transiting a nearby red dwarf star. *Science*, 374(6572):1271–1275, 2021.

Tim Lichtenberg and Yamila Miguel. Super-earths and earth-like exoplanets. *arXiv preprint arXiv:2405.04057*, 2024.

Tim Lichtenberg, Laura K Schaefer, Miki Nakajima, and Rebecca A Fischer. Geophysical evolution during rocky planet formation. *arXiv preprint arXiv:2203.10023*, 2022.

Andrew P Lincowski, Victoria S Meadows, Sebastian Zieba, Laura Kreidberg, Caroline Morley, Michaël Gillon, Franck Selsis, Eric Agol, Emeline Bolmont, Elsa Ducrot, et al. Potential atmospheric compositions of TRAPPIST-1 c constrained by JWST/MIRI observations at 15 μm. *The Astrophysical Journal Letters*, 955(1):L7, 2023.

Manasvi Lingam. Implications of abiotic oxygen buildup for earth-like complex life. *The Astronomical Journal*, 159(4):144, 2020.

J Lustig-Yaeger, G Fu, EM May, KN Ortiz Ceballos, SE Moran, S Peacock, KB Stevenson, M López-Morales, RJ MacDonald, LC Mayorga, et al. A JWST transmission spectrum of a nearby earth-sized exoplanet. arxiv e-prints, article. *arXiv preprint arXiv:2301.04191*, 2023.

Jack Madden and Lisa Kaltenegger. How surfaces shape the climate of habitable exoplanets. *Monthly Notices of the Royal Astronomical Society*, 495(1):1–11, 2020.

R. Maitre, A. Streckeisen, B. Zanettin, M. Le Bas, Bernard Bonin, and P. Bateman. *Igneous Rocks: A Classification and Glossary of Terms*, volume -1. Cambridge University Press, 12 2004.

Megan Mansfield, Edwin S. Kite, Renyu Hu, Daniel D. B. Koll, Matej Malik, Jacob L. Bean, and Eliza M.-R. Kempton. Identifying atmospheres on rocky exoplanets through inferred high albedo. *The Astrophysical Journal*, 886(2):141, dec 2019. doi: 10.3847/1538-4357/ab4c90.

Megan Weiner Mansfield, Qiao Xue, Michael Zhang, Alexandra S Mahajan, Jegug Ih, Daniel Koll, Jacob L Bean, Brandon Park Coy, Jason D Eastman, Eliza M-R Kempton, et al. No thick atmosphere on the terrestrial exoplanet Gl 486b. *The Astrophysical Journal Letters*, 975(1):L22, 2024.

Michel Mayor and Didier Queloz. A jupiter-mass companion to a solar-type star. *nature*, 378 (6555):355–359, 1995.

Tobias G Meier, Dan J Bower, Tim Lichtenberg, Mark Hammond, Paul J Tackley, Raymond T Pierrehumbert, José A Caballero, Shang-Min Tsai, Megan Weiner Mansfield, Nicola Tosi, et al. Geodynamics of super-Earth GJ 486b. *Journal of Geophysical Research: Planets*, 129 (10):e2024JE008491, 2024.

P.-Y. Meslin, O. Gasnault, O. Forni, S. Schröder, A. Cousin, G. Berger, et al. Soil diversity and hydration as observed by chemcam at gale crater, mars. *Science*, 341(6153):1238670, 2013. doi: 10.1126/science.1238670.

RE Milliken, T Hiroi, D Scholes, S Slavney, and R Arvidson. The nasa reflectance experiment laboratory (relab) facility: An online spectral database for planetary exploration. In *Astromaterials Data Management in the Era of Sample-Return Missions Community Workshop*, volume 2654, 2021.

EJ Mlawer, KE Cady-Pereira, J Mascio, and IE Gordon. The inclusion of the MT_CKD water vapor continuum model in the HITRAN molecular spectroscopic database. *Journal of Quantitative Spectroscopy and Radiative Transfer*, 306:108645, 2023.

Sarah E Moran, Kevin B Stevenson, David K Sing, Ryan J MacDonald, James Kirk, Jacob Lustig-Yaeger, Sarah Peacock, LC Mayorga, Katherine A Bennett, Mercedes López-Morales, et al. High tide or riptide on the cosmic shoreline? a water-rich atmosphere or stellar contamination for the warm super-earth GJ 486b from JWST observations. *The Astrophysical Journal Letters*, 948(1):L11, 2023.

Joshua Murray. *Ultramafic Alteration and the Cooling of Earth and Mars*. PhD thesis, Massachusetts Institute of Technology, 2024.

Harrison Nicholls, Raymond T Pierrehumbert, Tim Lichtenberg, Laurent Soucasse, and Stef Smeets. Convective shutdown in the atmospheres of lava worlds. *Monthly Notices of the Royal Astronomical Society*, 536(3):2957–2971, 2025a.

Harrison Nicholls et al. AGNI: A radiative-convective model for lava planet atmospheres. *Journal of Open Source Software*, 10(109):7726, 2025b. doi: 10.21105/joss.07726. URL https://doi.org/10.21105/joss.07726.

G Ortenzi, L Noack, F Sohl, CM Guimond, JL Grenfell, C Dorn, JM Schmidt, S Vulpius, N Katyal, D Kitzmann, et al. Mantle redox state drives outgassing chemistry and atmospheric composition of rocky planets. *Scientific reports*, 10(1):10907, 2020.

Meng-rui Pan, Jiang-hui Ji, and Su Wang. The statistical investigation of exoplanets around M dwarfs. *Chinese Astronomy and Astrophysics*, 45(4):507–530, 2021.

Emily K Pass, David Charbonneau, and Andrew Vanderburg. The receding cosmic shoreline of mid-to-late m dwarfs: Measurements of active lifetimes worsen challenges for atmosphere retention by rocky exoplanets. *The Astrophysical Journal Letters*, 986(1):L3, 2025.

Timothy E. Pickering, Klaus M. Pontoppidan, Victoria G. Laidler, Christopher D. Sontag, Massimo Robberto, Diane M. Karakla, Christopher Hanley, Karoline Gilbert, Christine Slocum, Nicholas M. Earl, Laurent Pueyo, Swara Ravindranath, Alberto Noriega-Crespo, Elizabeth Barker, and Mark J. Sienkiewicz. Pandeia: a multi-mission exposure time calculator for JWST and wfirst. In Alison B. Peck, Chris R. Benn, and Robert L. Seaman, editors, *Observatory Operations: Strategies, Processes, and Systems VI*, page 44. SPIE, July 2016. doi: 10.1117/12.2231768.

K Poppenhaeger, L Ketzer, N Ilic, E Magaudda, J Robrade, B Stelzer, JHMM Schmitt, and PC Schneider. The high-energy environment of the heavy sub-earth GJ 367 b indicates likely complete evaporation of its atmosphere. *Astronomy & Astrophysics*, 689:A188, 2024.

Keith D Putirka. Exoplanet mineralogy. *Reviews in Mineralogy and Geochemistry*, 90(1): 199–257, 2024.

Benjamin V Rackham, Néstor Espinoza, Svetlana V Berdyugina, Heidi Korhonen, Ryan J MacDonald, Benjamin T Montet, Brett M Morris, Mahmoudreza Oshagh, Alexander I Shapiro, Yvonne C Unruh, et al. The effect of stellar contamination on low-resolution transmission spectroscopy: needs identified by nasa's exoplanet exploration program study analysis group 21. *RAS Techniques and Instruments*, 2(1):148–206, 2023.

Birger Rasmussen, Bryan Krapež, and Daniela B Meier. Replacement origin for hematite in 2.5 Ga banded iron formation: Evidence for postdepositional oxidation of iron-bearing minerals. *Bulletin*, 126(3-4):438–446, 2014.

Emily Rauscher and Kristen Menou. A general circulation model for gaseous exoplanets with double-gray radiative transfer. *The Astrophysical Journal*, 750(2):96, 2012.

Seth Redfield, Natasha Batalha, Björn Benneke, Beth Biller, Nestor Espinoza, Kevin France, Quinn Konopacky, Laura Kreidberg, Emily Rauscher, and David Sing. Report of the

working group on strategic exoplanet initiatives with HST and JWST. *arXiv preprint arXiv:2404.02932*, 2024.

Andrew Ridden-Harper, Stevanus K Nugroho, Laura Flagg, Ray Jayawardhana, Jake D Turner, Ernst de Mooij, Ryan MacDonald, Emily Deibert, Motohide Tamura, Takayuki Kotani, et al. High-resolution transmission spectroscopy of the terrestrial exoplanet GJ 486b. *The Astronomical Journal*, 165(4):170, 2023.

Laurence S Rothman, Iouli E Gordon, Yury Babikov, Alain Barbe, D Chris Benner, Peter F Bernath, Manfred Birk, Luca Bizzocchi, Vincent Boudon, Linda R Brown, et al. The HITRAN2012 molecular spectroscopic database. *Journal of Quantitative Spectroscopy and Radiative Transfer*, 130:4–50, 2013.

Chandan K Sahu, Liton Majumdar, Sudipta Mridha, and Harshit Krishna. Unveiling the interior structure and thermal evolution of super-earth GJ 486b. *arXiv preprint arXiv:2501.09963*, 2025.

Fabian L Seidler, Paolo A Sossi, and Simon L Grimm. Impact of oxygen fugacity on the atmospheric structure and emission spectra of ultra-hot rocky exoplanets. *Astronomy & Astrophysics*, 691:A159, 2024.

Joshua S Speagle. dynesty: a dynamic nested sampling package for estimating bayesian posteriors and evidences. *Monthly Notices of the Royal Astronomical Society*, 493(3):3132–3158, 2020.

Maggie A Thompson, Joshua Krissansen-Totton, Nicholas Wogan, Myriam Telus, and Jonathan J Fortney. The case and context for atmospheric methane as an exoplanet biosignature. *Proceedings of the National Academy of Sciences*, 119(14):e2117933119, 2022.

first name TRAPPIST-1 JWST Community Initiative. A roadmap for the atmospheric characterization of terrestrial exoplanets with JWST. *Nature Astronomy*, 8(7):810–818, 2024.

T Trifonov, JA Caballero, Juan Carlos Morales, A Seifahrt, I Ribas, A Reiners, JL Bean, R Luque, H Parviainen, E Pallé, et al. A nearby transiting rocky exoplanet that is suitable for atmospheric investigation. *Science*, 371(6533):1038–1041, 2021.

Gwenaël Van Looveren, Sudeshna Boro Saikia, Oliver Herbort, Simon Schleich, Manuel Güdel, Colin Johnstone, and Kristina Kislyakova. Habitable zone and atmosphere retention distance (HaZARD)-stellar-evolution-dependent loss models of secondary atmospheres. *Astronomy & Astrophysics*, 694:A310, 2025.

Monica Vidaurri, Laura Schaefer, Ward Howard, and Meredith MacGregor. Who run the world? (flares): Ozone production in steam atmospheres during M-star superflares. *AAS/Division for Extreme Solar Systems Abstracts*, 56(4):625–04, 2024.

Joshua N Winn. Transits and occultations. *arXiv preprint arXiv:1001.2010*, 2010.

Nicholas Wogan, Joshua Krissansen-Totton, and David C Catling. Abundant atmospheric methane from volcanism on terrestrial planets is unlikely and strengthens the case for methane as a biosignature. *The Planetary Science Journal*, 1(3):58, 2020.

Robin Wordsworth and Laura Kreidberg. Atmospheres of rocky exoplanets. *Annual Review of Astronomy and Astrophysics*, 60(1):159–201, 2022.

Qiao Xue, Jacob L Bean, Michael Zhang, Luis Welbanks, Jonathan Lunine, and Prune August. JWST transmission spectroscopy of HD 209458b: A supersolar metallicity, a very low C/O, and no evidence of CH4, HCN, or C2H2. *The Astrophysical Journal Letters*, 963(1):L5, 2024.

Jack S Yates, Paul I Palmer, James Manners, Ian Boutle, Krisztian Kohary, Nathan Mayne, and Luke Abraham. Ozone chemistry on tidally locked M dwarf planets. *Monthly Notices of the Royal Astronomical Society*, 492(2):1691–1705, 2020.

Kevin J. Zahnle and David C. Catling. The cosmic shoreline: The evidence that escape determines which planets have atmospheres, and what this may mean for proxima centauri b. *The Astrophysical Journal*, 843(2):122, July 2017. doi: 10.3847/1538-4357/aa7846.

Michael Zhang, Renyu Hu, Julie Inglis, Fei Dai, Jacob L Bean, Heather A Knutson, Kristine Lam, Elisa Goffo, and Davide Gandolfi. GJ 367b is a dark, hot, airless sub-earth. *The Astrophysical Journal Letters*, 961(2):L44, 2024.

Sebastian Zieba, Laura Kreidberg, Elsa Ducrot, Michaël Gillon, Caroline Morley, Laura Schaefer, Patrick Tamburo, Daniel DB Koll, Xintong Lyu, Lorena Acuña, et al. No thick carbon dioxide atmosphere on the rocky exoplanet TRAPPIST-1 c. *Nature*, 620(7975):746–749, 2023.